Modeling of the mineral dust cycle under present and glacial climate conditions

Tim Hannemann

Master thesis

University of Bremen

Alfred Wegener Institut Bremerhaven

10.04.2015

Abstract

Atmospheric dust influences directly and indirectly the radiative properties of the atmosphere and biogeochemical cycles like the carbon cycle. Thus, it plays a crucial role to the climate system Earth and its seasonal and long-term variability. During glacial periods like the last glacial maximum, the dust cycle has been significantly stronger. Beside the influence of different climate conditions, like the weakened glacial water cycle and increased glacial wind speeds, the vegetation coverage during glacial times is assumed to be an essential factor of the changed dust cycle.

The aim of this master thesis is to improve our understanding of the dust cycle by analysing the influence of two different climate periods (the present-day (PD) and the last glacial maximum (LGM)) as well as two related vegetation distributions on the dust cycle.

For this purpose, a set of dust cycle simulations using the general circulation model ECHAM, extended by the aerosol model HAM are carried out. The performed simulations are varied in the prescribed climate boundary conditions, vegetation distribution, as well as model resolution. The prescribed vegetation distributions are either based on an empirical analysis of present-day satellite observations or on results of a fully coupled run of the COSMOS Earth-System-Model. For both present-day and LGM simulations, two different horizontal and vertical model resolutions (T31L19, T63L31) are applied.

The results of this thesis show that the climate conditions and the vegetation distributions significantly affect the magnitude and seasonality of dust emissions, transport and deposition. Applying the modeled vegetation distribution leads to a less pronounced seasonality of the dust cycle and regional variations as compared to the simulation with the observational vegetation distribution. Nevertheless, both simulation types yield for present-day a very similar annual, global dust burden. For the last glacial maximum climate conditions, the simulation using the observational, present-day vegetation distribution leads to a twofold increase of the dust burden. Prescribing the modeled, glacial vegetation distribution produces a threefold increase and highlights the importance of glacial vegetation changes for the increased strength of the dust cycle during the LGM.

To evaluate the simulation results, it is compared to a compilation of observational data of marine and ice core records (DIRTMAP3). As only few coring sites are located in the mid-latitudes of the southern hemisphere, additional coring sites from the recent Polarstern cruise ANT-XXVI / 2 are added to the analysis. The evaluation reveals for example, that increased glacial depositions are reproduced quite well by the simulations with the modeled, glacial vegetation distribution, though some regions remain underestimated.

Declaration of Authorship

I declare that the work presented here is, to the best of my knowledge and belief, original and the result of my own investigations, except as acknowledged, and has not been submitted, either in part or whole, for a degree at this or any other University.

Formulations and ideas taken from other sources are cited as such. This work has not been published.

Bremen, 10th April 2015 Tim Hannemann

Contents

1 Introduction and motivation

The emission of dust into the atmosphere is a major source for airborne aerosols and its estimates range from 60 to 3000 $Mt \cdot yr^{-1}$ [Duce, 1995]. Atmospheric dust impacts onto local and global climate by different processes. E.g. dust alters the radiative transfer of solar and terrestrial radiation due to scattering and absorption [Dentener et al., 1996] and works as cloud condensation nuclei, affecting the climate indirectly [Albrecht, 1989, Twomey, 1974]. Thus, the study of the dust cycle, its sources, transport routes and sinks are of high relevance in climate research, as the dust cycle is not yet fully understood [Dentener et al., 1996, Tegen, 2002]. Of special interest are glacial periods because the dust cycle has been more intense compared to present-day or other interglacial periods [Petit et al., 1999]. This change is due to the different boundary conditions during the colder periods, such as the weakened water cycle and changed vegetation distribution [Mahowald et al., 1999]. Especially the latter is not yet sufficiently investigated and often, models prescribe the same vegetation distribution for present-day simulations as for glacial simulations.

In this master thesis, the deviations evoked by prescribing modeled vegetation distributions, that incorporate the conditions for different climate conditions, are analysed. Beside the present-day (PD) climate conditions, these are the climate conditions of the last glacial maximum (LGM) because this most recent cold period and its characteristics are well known. This way, the investigation of the dust cycle for different climate boundary conditions, can help to improve the understanding of the dust cycle in general.

1.1 Definition of dust

Dust originating from soil can be defined as mineral aerosols [Mahowald et al., 2006a]. An aerosol in turn is a dispersion of solid and/or material liquid in air. The composition of atmospheric dust depends on its source region [Sudarchikowa, 2012] and consists of a mixture of minerals such as quartz, feldspars, gypsum, calcite and clay minerals [Harrison et al., 2001, Kohfeld and Tegen, 2007]. These in turn are rich in components such as aluminium, iron, oxides and hydroxides [Harrison et al., 2001]. As dust is contributing largely to the global aerosol load [Kohfeld and Tegen, 2007, Textor, 2006], mineral dust has an impact onto the energy balance of both the solar and the planetary radiation [Mahowald et al., 2006a, Tegen, 2002]. Thus, a change in the amount of the atmospheric dust burden will change the radiation balance and consequently the surface temperature of the Earth [Tegen, 2002].

1.2 Dust during present-day and last glacial maximum

Geological and historical records indicate that mineral aerosols are sensitive to changes in climate [Mahowald et al., 2006a]. A decrease of the vegetation distribution due to climate change will enforce the dust cycle, the remaining bare soil is a prerequisite for its emission. A weakened water cycle affects the wet deposition of mineral aerosols, causing a prolonged lifetime of dust in the atmosphere. Vice versa, mineral aerosols are suspected to trigger biogeochemical reactions which are partly responsible for some of the 80 ppm change in carbon dioxide between glacial and interglacial time periods [Mahowald et al., 2006a, Watson et al., 2000]. By contrast, dust might compensate some of the warming, influencing the radiative balance and thus climate conditions. As a result, changes in climate caused by dust, may feed back onto the dust cycle itself [Tegen, 2002]. On this account the importance of regarding different climate conditions becomes evident, as these are an important factor for the intensity of the dust cycle.

1.2.1 Last Glacial Maximum (LGM)

The last glacial maximum (LGM) has been a major research focus for dust modeling studies for several reasons [Joussaume et al., 1999, Mahowald et al., 1999]. Firstly, changes in boundary conditions, such as the extent of ice sheets or the atmospheric composition are well known for this latest cold period [Barnola et al., 1987]. Secondly, the deposition of mineral dust was two to five times higher in the tropics and mid latitudes and even up to 20 times higher in the polar regions [Harrison et al., 2001]. These deposition fluxes have been reconstructed from ice cores and terrestrial and marine sediments which were considerably richer during past cold periods such as the LGM [Kohfeld and Harrison, 2001, and references therein].

The effects of dust onto the climate might have been stronger for glacial times than for interglacial periods and the changes in dust burden might have contributed to the changes in glacial-interglacial temperature [Tegen, 2002] as mineral aerosols could have had a larger influence onto the warming of polar regions during the transition from the last glacial maximum to the Holocene [Knippertz, 2013].

Following model-based studies of Harrison et al. [2001], Mahowald et al. [1999] and Werner et al. [2002] the enforcement of the dust cycle during the last glacial maximum has been up to one third in response to changes in dust source areas. This is a direct result from the glacial change in vegetation cover. Other reasons for the enforced dust cycle were the erosion of coastal shelves [Sudarchikowa, 2012], a weaker water cycle and the associated lower soil moisture [Mahowald et al., 2006b, Werner et al., 2002] as well as the change in wind velocities and pattern. The latter is estimated by Werner et al.

[2002] to be responsible for the other two thirds in the increased dust burden during LGM.

The comparatively higher LGM wind velocities under different model resolutions were the research topic for the bachelor thesis of Tim Carlsen at the Alfred Wegener Institute, Bremerhaven [Carlsen, 2014]. Carlsen examined the present-day to glacial change in wind velocities and pattern and found it to be a major factor for the increased dust emissions. Even though a refinement of the model resolution should lead to increased, local wind speeds, no general change of the dust cycle for a finer resolution was found.

1.3 Structure of the master thesis

This master thesis is based on the bachelor thesis of Carlsen [2014], who investigated the influence of the present-day and last glacial maximum climate conditions on the wind strength and wind pattern for different model resolutions and climate conditions.

In contrast, the aim of this master thesis is to discuss the influence of two prescribed vegetation distributions (Chapter 3.2.1) onto the dust cycle of the last glacial maximum for two different model resolutions (Chapter 4.1). Starting generally and leading towards the details of dust and its properties, Chapter 2 describes the theoretical background of this master thesis research. Initially, the dust cycle, some special properties of dust and the impact of dust onto the radiation budget are explained. Finally, some basic differences between the recent present-day (PD) and the last glacial maximum (LGM) are explained.

Chapter 3 describes the general circulation model ECHAM5 applied in this study and the additionally implemented aerosol module HAM2. Basic characteristics of the combined ECHAM5-HAM2 model like the discretisation of the aerosol spectrum, vegetation cover and dust source areas and the horizontal and vertical flux of dust are presented.

The results are described and discussed in Chapter 4 and evaluated against observational data in Chapter 5. Chapter 6 gives a conclusion and an outlook towards possible, further investigations.

2 Physical background

2.1 Dust cycle

Global cycles, such as the dust cycle describe the exchange of particles between various reservoirs within the climate system Earth [Seinfeld and Pandis, 1998]. The dust cycle in particular characterises the atmospheric processes that lead to the emission, transport, transformation and deposition of mineral aerosols [Zhang et al., 2012]. In the following description, only the atmospheric part of the dust cycle is going to be described as it represents the only part important for this study.

Climate parameters like precipitation, humidity, wind and vegetation cover are important factors for the processes involved in the emission, transport and deposition of dust [Kohfeld and Harrison, 2001]. These processes are described in the following chapters. As they can change on geological time scales in response to climate variation, feedback mechanisms can be inferred. Consequently, changes in the climate and changes in the dust cycle can depend on each other [Tegen, 2002].

2.1.1 Emission

The emission of dust is defined as the vertical mass flux of dust from the surface into the atmosphere [Shao, 2008]. This built up of mineral aerosols is evoked by the impact of surface winds [Marticorena and Bergametti, 1995]. Regarding the present-day, the estimated global emission of dust ranges from 60 Mt yr^{-1} to 3000 Mt yr^{-1} [Tegen, 2002, and references therein] with a rough average of 2000 Mt yr^{-1} [Shao et al., 2011]. Single dust outbreaks, which may last up to a few days, can strongly increase the regional, annual dust emission rate [Gläser et al., 2012].

Three forces counteract the emission of dust and have to be overcome by the wind induced drag exerted on the dust particle. For any particle at rest, these are the gravity, the interparticle cohesion and the wind shear stress on the surface [Marticorena and Bergametti, 1995]. The latter depends on the transfer of the wind energy to the surface, while the gravity and interparticle cohesion depend on the size or respectively the mass. A conventional size distribution of particles is presented in Table 1 in Chapter 2.2.1.

The balance of all forces exerted onto the dust particle defines the minimum threshold friction velocity U_t^*, defined as the velocity, necessary to induce the emission of a dust particle. Thus, emission can only take place if the friction velocity U^* overcomes the threshold friction velocity U_t^* [Marticorena and Bergametti, 1995]. The velocity U^* can be inferred as the square root of the ratio of surface stress τ_{surf} to air density ρ_{air}:

$$U^* = \sqrt{\frac{\tau_{surf}}{\rho_{air}}} \tag{1}$$

Three processes can be distinguished for the emission of dust into the atmosphere. These are depicted in Figure 1, following the explanations are based on the descriptions by Shao [2008].

- **Aerodynamic lift:** Dust particles can be lifted by the aerodynamic forces exerted through the wind stress onto the surface. This effect is negligible for small particles as inter-particle cohesion forces dominate.
- **Saltation bombardment:** Larger particles like sand grains may be put into motion by the aerodynamic lift. As these are too heavy to be lifted into the air, they bounce over the surface and may cause impactions that are strong enough to pass on sufficient kinetic energy to lift smaller particles into the air. This effect is also known as *wind blasting*.
- **Disaggregation:** Dust particles may stick together as aggregates. Such behave like one big particle during a weak wind event but may disintegrate during a stronger wind event. This disaggregation can result in the emission of dust into the atmosphere.

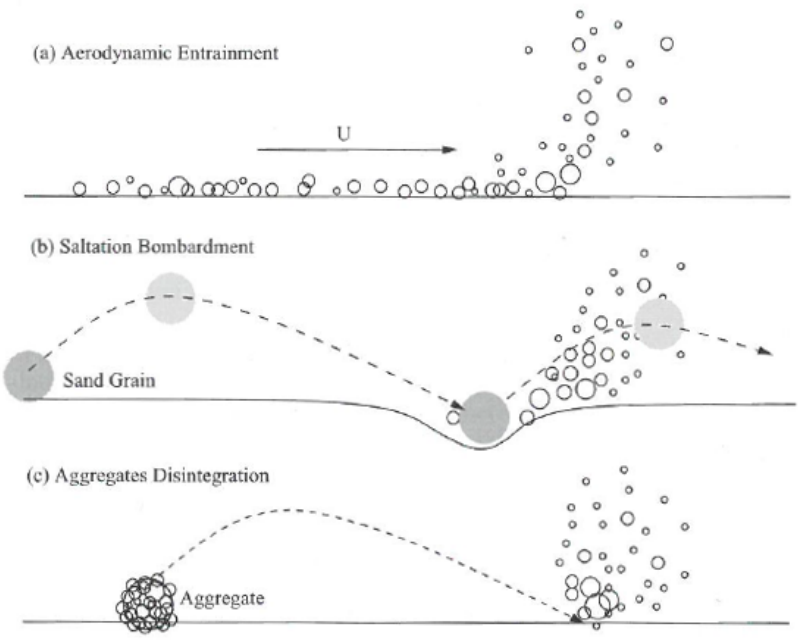

Figure 1: Mechanisms for dust emission. (a) Dust emission by aerodynamic lift, (b) by saltation bombardment and (c) through disaggregation. Figure adapted from [Shao, 2008]

Surface wetness and precipitation play a crucial role, as they inhibit the emission of dust into the atmosphere, when a certain soil wetness is exceeded [Marticorena and Bergametti,

1995]. This wetness is called threshold wetness and is usually set by the clay content of the soil as this component has the highest resistance against draining. Thus, the drying rate can be seen as a function of the clay content of the soil, the recent precipitation and the surface temperature [Marticorena and Bergametti, 1995]. Likewise, wind can dry the uppermost layer of the Earth's surface.

Figure 2 from Kohfeld and Tegen [2007] shows the aerosol index values observed by the Total Ozone Mapping Spectrometer (TOMS). These indicate the location of major source regions for mineral aerosols and their main transport direction. According to Figure 2 the largest contributing areas are the Sahara, the Arabian peninsula and central Asia. But also Australia and some regions in North and South America are important dust source regions.

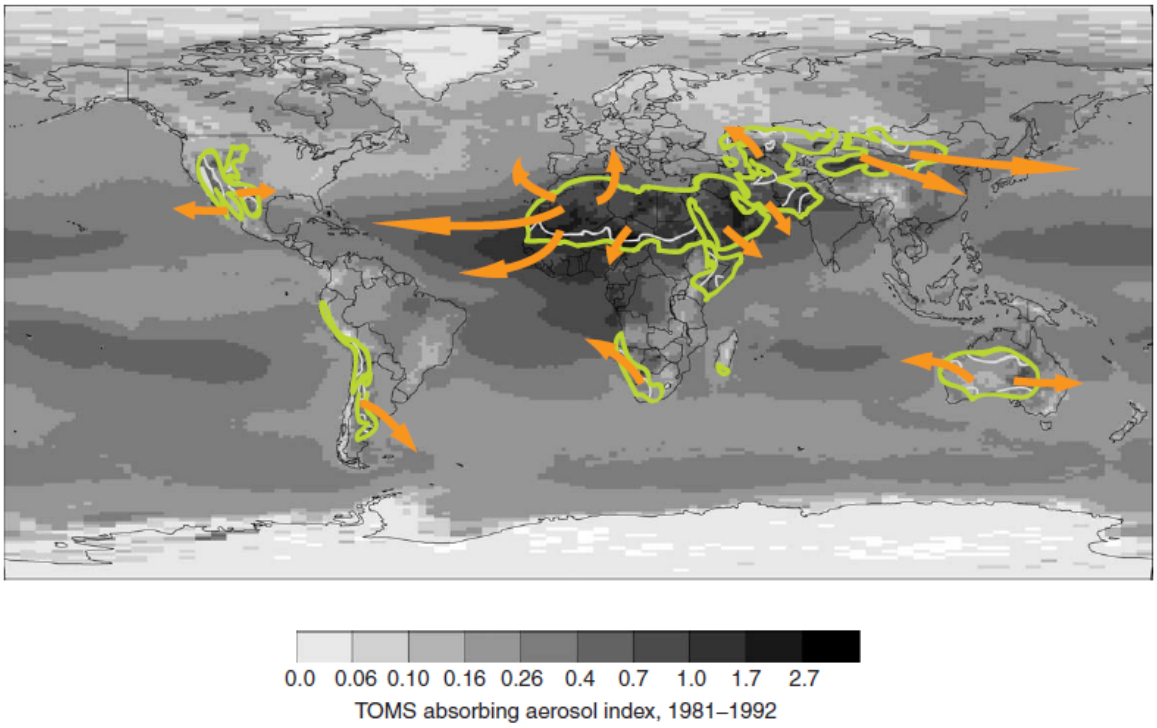

Figure 2: TOMS aerosol index values averaged from 1981 to 1992. Largest source areas are located in arid tropical-subtropical regions of Africa and the Middle East. Green lines outline regions that are considered dust sources. Orange arrows indicate the general direction of dust transport from these regions. Figure adapted from Kohfeld and Tegen [2007]

2.1.2 Transport and transformation

The path of a dust particle in the atmosphere depends on the balance between gravity and aerodynamic drag [Shao, 2008]. While gravity acts downward, diffusion due to turbulence may take the particle upwards into the upper levels of the atmosphere. Here, the particle can be carried over large distances by synoptic processes and global wind systems until it gets finally deposited back to the surface. The orange arrows in Figure 2 indicate some of the main transport directions close to the source areas of dust emissions.

During their residence in the atmosphere, dust can influence the radiative balance and atmospheric processes such as cloud formation and precipitation (see Chapter 2.2.2) [Shao et al., 2011]. Reactions with other dust particles can change the chemical properties of dust [Dentener et al., 1996]. While freshly emitted dust particles are assumed to be insoluble, their surfaces can become coated with sulphate and nitrate species, hereby turning the particle hydrophilic and thus soluble [Stier et al., 2005]. The efficiency of aerosols to form condensation or ice nuclei is set by their hygroscopicity.

Compared to other aerosols, dust particles have a large surface area, which evokes a high reactivity. Thus, dust particles may have a distinct influence on other cycles, such as the ozone and nitrogen cycle [Dentener et al., 1996, Tegen, 2002].

2.1.3 Deposition

The deposition of airborne mineral aerosols can be defined as the removal of dust particles from the atmosphere by different sink processes. These sink processes are basically sedimentation, dry and wet deposition [Seinfeld and Pandis, 1998, Stier et al., 2005]. The distance that particles travel before they are deposited, depends on the particle size and on the flow conditions during the atmospheric transport.

- **Sedimentation:**

  The lifetime of dust particles depends on their size. The larger the particle, the faster it gets deposited. The largest particles with radii of $r > 10\,\mu m$ are deposited after seconds to hours while small particles with $r < 1\,\mu m$ may reside 10 to 15 days in the atmosphere [Shao et al., 2011]. The quick deposition of large particles can be attributed to the large mass of the particles, as they get deposited due to the gravitational settling. This settling is also called sedimentation and especially takes place close to the emission areas [Seinfeld and Pandis, 1998].

  Because of the fast sedimentation of large dust particles, the size-distribution of

the mineral aerosols is shifted towards smaller radii with increasing life-time [Harrison et al., 2001]. As a consequence, other deposition processes, such as dry and wet deposition, become more important over time.

Some studies, such as Shao [2008] regard the sedimentation as a part of the dry deposition which is reasonable, as no water is involved in both processes. But as the sedimentation solely makes up the largest part of the sink processes, it is regarded individually here. Moreover, it could be understood as the direct counterpart of the emission due to wind drag and occurs due to the lack of it.

- **Dry deposition:**

  Dry deposition is defined as the deposition through diffusion, impaction and interception [Seinfeld and Pandis, 1998]:

  - **Diffusion:** This effect describes the inelastic collision of very small aerosol particles due to the Brownian movement. As their mass is little, they do not posses enough inertia to rebound from each other and stick together. This process is also called coagulation.
  - **Impaction:** As the particles posses masses, they have some inertia which is causing the so called impaction. Here, particles literary impact and keep attached as they clamp to the deformed surface.
  - **Interception:** The last process is the interception, which occurs as a result of the interaction of the particle with the surface. The latter may trap dust aerosols due to static electricity, surface wetness or specific surface characteristics, such as fine hairs on vegetation.

- **Wet deposition:**

  The major sink for far travelling dust particles is the wet deposition [Tegen, 2002]. It refers to the mass flux of mineral aerosols to the Earth's surface that are scavenged by hydrometeors [Shao, 2008]. These hydrometeors could be cloud and fog droplets, as well as precipitation and ice crystals [Seinfeld and Pandis, 1998]. In general, scavenging describes the process of the collection of dust particles and can be divided into in-cloud scavenging (rainout) and below-cloud scavenging (washout) [Seinfeld and Pandis, 1998, Shao, 2008]. In-cloud scavenging describes the process of forming cloud droplets by dust particles working as cloud condensation nuclei (CCN). By contrast, below-cloud scavenging refers to the collision or coagulation of dust particles with raindrops and ice crystals as these precipitate.

2.2 Properties of dust

2.2.1 Size distribution of dust

Aerosols in general are understood as particles with a mean radius $\bar{r}$ that ranges between $0.5\,nm$ and $50\,\mu m$ [Stier et al., 2005]. All aerosol particles with a radius below $0.5\,\mu m$ are so called fine aerosols. These in turn can be divided into four different modes, named Nucleation, Aitken, Accumulation and Coarse mode which are listed with their associated mean radius range in Table 1.

Aerosol type	**Modes**	**Mean radius $\bar{r}$ $[\mu m]$**
Fine aerosols	Nucleation	$\bar{r} \leq 0.005$
	Aitken	$0.005 \leq \bar{r} \leq 0.05$
	Accumulation	$0.05 \leq \bar{r} \leq 0.5$
Coarse aerosols	Coarse	$0.5 \leq \bar{r}$

Table 1: Size distribution of mineral particles in used in ECHAM5-HAM2. Adapted from Stier et al. [2005]

As dust particles are irregularly shaped, r cannot be regarded as the radius of a perfect spherical particle. Instead, the mean or geometric radius is used, which can be determined as a the radius of a perfect sphere with the same volume as the dust particle [Mahowald et al., 2013].

2.2.2 Impact of dust onto the radiation budget

As stated in Chapter 1.1, dust is contributing largely to the global aerosol burden [Kohfeld and Tegen, 2007, Tegen, 2002, Textor, 2006] and can influence the climate conditions [Harrison et al., 2001]. The perturbation of the radiation balance implied by the mineral aerosols is called dust forcing [Tegen, 2002]. Whether this dust forcing contributes positively or negatively to the radiative budget, depends on the optical properties of the mineral aerosols [Tegen et al., 1996] as well as the position of the dust within the atmospheric column, the presence of clouds and the albedo of the surface beneath [Seinfeld and Pandis, 1998, Tegen et al., 1996].

Dust interacts with radiation by either absorbing, emitting or scattering processes. These processes in turn, depend on the particle size and the refractive index of the aerosol particle [Tegen, 2002]. While solar short wave radiation is only scattered or absorbed, terrestrial long wave radiation is also emitted. By its impact on the radiative balance, dust can change the total planetary albedo, depending on the albedo of the underlying surface and the single scattering albedo of the dust particles themselves [Harrison et al., 2001, Tegen et al., 1996]. Thus, dust forcing may lead on the one hand to a net cooling

of the surface by enhancing the back radiation into space (by increasing the planetary albedo). On the other hand dust forcing may contribute to the greenhouse effect (by lowering the planetary albedo) [Tegen, 2002]. In any case, dust can change the radiation balance and consequently the surface temperature of the Earth. As an example, dust forcing could lead to a cooling over forests which have a comparatively lower albedo but it could lead to a warming over ice which has a higher albedo [Sudarchikowa, 2012]. Figure 3 from Mahowald et al. [2013] sketches and summarises the impact of mineral aerosols on climate. Moreover, it depicts the dust cycle and its components.

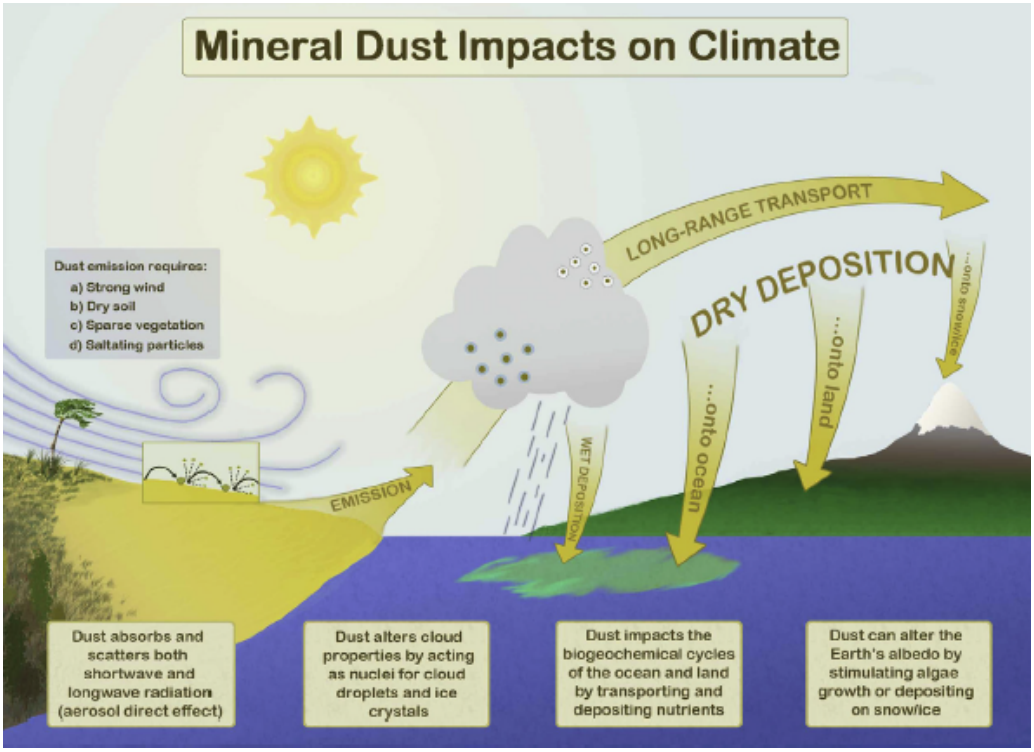

Figure 3: Scheme of the dust cycle and its impacts onto the climate. Interactions of dust with the radiation balance, clouds, biogeochemical cycles and the Earth's albedo are mentioned. Adapted from Mahowald et al. [2013].

Results from Perlwitz [2001] indicate that direct dust forcing leads to a net cooling of the surface. Additionally, Tegen [2002] states that the response of the climate to dust forcing will not necessarily follow the patterns of dust distributions, as the atmospheric circulation might change in course of the dust influence. Both the direct and the indirect impact of dust, which are explained below, are potentially large but remain basically unknown. They describe the impact of dust on the radiative transfer, the cloud formation and the longevity of water in the atmosphere. The interdependency of climate and dust forcing as well as the dimension of dust fluxes are not yet totally understood [Albrecht, 1989, Twomey, 1974].

- **Direct aerosol effect:**

  The direct dust aerosol effect describes the changes of the radiative transfer by mineral aerosols. As a consequence, the radiative energy balance is modified by the already mentioned ability of dust to absorb, scatter and reflect both solar and terrestrial radiation [Miller and Tegen, 1998].

  Depending on the concentrations of dust in the different altitudes, different atmospheric layers undergo a warming. This has a direct influence onto the stability of the atmospheric layering and the predominant wind patterns. Moreover, local warming can cause evaporation of clouds, which again changes the planetary albedo.

- **Indirect aerosol effects**

  Two indirect dust aerosol effects exist, describing the impact of mineral aerosols on the formation of clouds and their longevity. They are called first and second indirect aerosol effect or Twomey and Albrecht effect.

  The first indirect aerosol effect (Twomey effect) describes the modification of cloud characteristics by mineral aerosols [Twomey, 1974]. These work as cloud condensation nuclei (CCN) or even ice nuclei [Sassen et al., 2003]. Hereby, the aerosols cause the cloud droplets or ice crystals to be more numerous but smaller at the same time. As a direct consequence, the cloud albedo increases [Twomey, 1974]. As already stated in Chapter 2.1.2, the crucial characteristic of aerosols to form nuclei is their hygroscopicity as it sets the efficiency with which aerosols form droplets [Tegen, 2002]. The change in number and size of droplets within the cloud also changes its brightness and the amount of precipitation that might occur [Tegen, 2002]. Hence, it changes the hydrological cycle and the optical properties of the droplets/crystals which affects the radiative balance [Arimoto, 2001].

  The second indirect aerosol effect (Albrecht effect) does not influence the precipitation as efficiently as the first indirect one. It describes the increased lifetime of droplets in the atmosphere, which results from the decrease of the average droplet size [Albrecht, 1989]. For that reason, the lifetime of water in the atmosphere is increased, lowering the cloud albedo and leading to a net cooling of the Earth's surface (unless over ice/ snow).

2.2.3 Dust impact on biogeochemical cycles

When dust aerosols are deposited in vegetated regions or over the ocean, the mineral compounds can serve as a fertiliser to the ecosystem as they contain and transport micro nutrients, which influences the productivity of both the terrestrial and the marine ecosystem. Martin et al. [1994] stated, that an increased input of iron into the ocean would stimulate the growth of marine algae. This increase in marine biomass leads to a higher consumption of the greenhouse gas CO_2, which would affect the radiative balance of the Earth.

An altered dust cycle thus would affect the fertilization of the ecosystem, which in turn could lead to a change in climate conditions. Mahowald et al. [2006b] for example indicate that the fertilization may reduce in future in response to a possible weakening of the dust cycle. Succeeding weaker fertilization of marine algae then could lead to consequences, such as a lower uptake of CO_2. This way, the dust cycle has an indirect impact on climate conditions and their change.

2.2.4 Anthropogenic impact and prognosis

The presence of human beings and their interaction with the environment change the surface of the Earth and consequently the dust burden released into the atmosphere. Processes in agriculture and forestry, the deforestation of rainforests, the building of cities and rural areas have lead to increased erosion and thus anthropogenic dust emissions. This increase has been observed especially during the last centuries and may increase further as a result of the drying of the subtropics and land-use change [Knippertz, 2013, Mulitza et al., 2011]. A strengthening of the hydrological cycle of the mid-latitudes may lead to the offset of this increased dust emission by enhanced wet deposition.

But even though it is believed that the anthropogenic impact plays an important role to the dust cycle and thus to the current state and the future of the climate, its contribution is not yet completely understood [Sokolik and Toon, 1996, Tegen and Fung, 1995]. As a direct result, a large variety of expectations and predictions exist. Woodward et al. [2005] for example forecast a tripling of the dust burden until year 2100 by the increase of source areas. By contrast, Tegen [2002] and Mahowald et al. [2006b] expect the dust burden to decrease by up to 60 %.

2.3 Climate during present-day and last glacial maximum

The Holocene is the youngest climate period in Earth's history. Its began with the end of the last glacial maximum at roughly 11,700 years before present and is still continuing today. Thus, the present-day can be attributed to the last years or decades of this

current interglacial period. The basic differences between the present-day and the last glacial maximum climate period are differences in climate forcing and conditions. These result from changes in the concentrations of green house gases, such as carbon dioxide (CO_2), methane (CH_4) and laughing gas (N_2O), the differences in orbital parameters, which will affect the spatial distribution and seasonality of incoming solar radiation (see Chapter 2.3.1) and the differences in topography, which are themselves a consequence of the changed and colder climate conditions.

The last glacial maximum (LGM) was 21,000 years before present-day (PD) and is in contrast to the present-day characterised by a more active dust cycle [Kohfeld and Harrison, 2001, and references therein] as well as a colder and thus drier climate. The basic reasons for the colder climate were the built up of ice, prior to the last glacial maximum and the decrease of the CO_2-concentration, resulting from a change of orbital parameters. Details for both the present-day and last glacial maximum orbital parameters can be seen in Table 4 in Chapter 4.2. Due to the colder climate, more water has been stored at the poles in terms of ice caps. As a result, the sea level was lower by $\sim$116 m and the hydrological cycle was weaker [Braconnot et al., 2012, Joussaume et al., 1999]. Another consequence was a change in atmospheric transport patterns and an increase in wind velocities.

2.3.1 Orbital parameters

The orbit of the Earth around the Sun varies in response to different astronomical periodicities. While the annually integrated solar flux is constant, the instantaneous solar flux density changes according to the periodic variations of the Earth's orbit. These periodicities are called Milankovitch cycles, named after the astronomer Milutin Milankovitch, and are thus variations in radiative forcing onto the Earth, changing the incoming solar radiation both seasonally and spatially [Barry and Chorley, 2010]. Three different cycles are distinguished, including the eccentricity, obliquity and precession of the Earth's orbit.

- **Eccentricity:**

  The deviation of the Earth's orbit from a circular path is called eccentricity. It is due to the gravitational influence of other planets with a period of about 100,000 years and 410,000 years. It can affect the differences between the seasons on the two hemispheres as the incoming solar radiation changes with the distance Earth-Sun [Barry and Chorley, 2010, Rödel and Wagner, 2011].

- **Obliquity:**

The rotation axis of the Earth is tilted compared to the areal normal of the orbit around the Sun (skewness of the ecliptic). This tilt is changing on a period of approximately 41,000 years and causes the seasons due to a seasonal change of incoming solar radiation [Barry and Chorley, 2010].

- **Precession:**

  Due to the fact that the rotation axis is tilted and that the density of the Earth is not spread rotationally symmetric, the gravity of Sun and Moon imply a torque onto the Earth. As any gyroscope, the Earth does not follow this torque but evades into a precession movement. It has a period of 19,000 years and 21,000 years and influences the seasons. Together with the eccentricity, the precession changes the incoming solar radiation at perihelion and aphelion of the elliptic orbit [Barry and Chorley, 2010, Rödel and Wagner, 2011].

3 Model description

In this chapter, a description of the used climate model ECHAM5 and the implemented aerosol module HAM2 for simulating the atmospheric aerosols will be described. Dust related processes relevant for this study are regarded in detail.

3.1 The ECHAM5-HAM2 General Circulation Model

A general circulation model (GCM) can literary be described as a virtual Earth upon which experiments can be performed [Donner et al., 2011]. In general, a GCM simulates circulations within the climate system Earth on a global scale in response to climate forcing such as the meridionally and seasonally imbalanced incoming solar radiation (see Chapter 2.3.1). Global circulations include for example the atmospheric circulation of air masses and the circulation of water masses in the oceans. Tracers like dust or CO_2 are transported by these circulations and their cycle can be simulated within a GCM.

The ECHAM5 atmospheric general circulation model is the fifth generation GCM of the ECHAM model developed by the Max Planck Institute for Meteorology (MPIM) in Hamburg, Germany [Roeckner et al., 2003]. It is based on the operational forecast model cycle 36 (1989) invented by the European Centre for Medium Range Weather Forecast (ECMWF).

The implemented Hamburg Aerosol Module (HAM2) is a complex aerosol model [Zhang et al., 2012]. Its main purpose is the quantification of aerosol loading and radiative effects and how these change the global climate system under present-day and other climate conditions.

3.1.1 ECHAM5

The following descriptions and explanations of the GCM ECHAM5 are based on the manual written by Roeckner et al. [2003].

ECHAM5 describes the general circulation of the atmosphere by numerically solving a system of non-linear differential equations. These are primarily the conservation laws for mass, momentum and energy. Concerning the equations of motion, the primitive set of equations is used, replacing the vertical z-component by a hydrostatic approximation. The regarded prognostic model variables include physical properties, such as vorticity, divergence, surface air pressure and temperature. The flux of trace components, such as mineral aerosols, is estimated by a semi-Lagrangian transport scheme, which is realised on a Gaussian grid. Such a grid divides the Earth in equidistant, zonal rings of latitude

and longitudes of equal length going from pole to pole.

3.1.2 HAM2

The HAM2 model is based on a flexible microphysical approach, meaning that it "predicts the evolution of an ensemble of microphysically interacting internally- and externally-mixed aerosol populations as well as their size-distribution and composition" [Stier et al., 2005].

The optical properties of aerosols are calculated by HAM2 in dependence of their size and composition. This in turn allows the determination of the radiative effects caused by aerosols, directly from the prognostic variables provided by ECHAM5 [Stier et al., 2005]. The combined ECHAM5-HAM2 model then simulates the amount and composition of tracers such as aerosols by considering the most important physical processes, ranging from the micro- to the global scale. On that account, ECHAM5-HAM2 estimates the radiative effects of the aerosols on the dynamics of the atmosphere [Zhang et al., 2012]. In order to make ECHAM5-HAM2 in particular as complete as possible, the attempt was made to minimise the number of external parameters, so that it can run as independently from exterior conditions as possible.

The major aerosol components in HAM distinguished by Stier et al. [2005] are mineral dust (DU), sulphate (SU), black carbon (BC), particulate organic matter (POM) and sea salt (SS). The terrestrial surface types, that are considered, are snow/ ice, bare soil, vegetation, wet skin, open water and sea ice [Zhang et al., 2012].

HAM2 is driven by meteorological data derived from the ECHAM5 simulation. This data includes variables such as the temperature, air pressure, air moisture, two horizontal components of the wind velocity and one vertical wind component. In return, HAM2 influences ECHAM5 by returning the radiative and climate conditions changed by the scheme for the cloud microphysics [Lohmann and Roeckner, 1996]. These include among others prognostic equations for cloud liquid water and ice [Lohmann and Roeckner, 1996, Stier et al., 2005]. As aerosols are treated just like other tracers within ECHAM5, they are transported along with the convective and turbulent movement of the air. As stated before in Chapter 2.2.2 and 2.1.3, the sink processes, as well as the aerosol optical properties depend on the composition of the dust particles.

3.1.3 Discretisation of the aerosol spectrum

The spectrum of aerosols and their sizes is represented in HAM2 by the superposition of seven log-normal size distributions. These log-normal modes are divided into the four

different geometrical size classes described in Chapter 2.2.1 (Nucleation, Aitken, Accumulation and Coarse mode). Three out of the seven modes comprise only insoluble compounds, while the other four contain one or more soluble compounds. This takes into account that the emitted dust particles are assumed to be insoluble [Stier et al., 2005]. Details of the aerosol scheme are listed in Table 2 which is showing an overview over the different characteristics of the log-normal distributions.

Modes $\bar{r}$ $[\mu m]$	**Soluble/ Mixed**	**Insoluble**
Nucleation $\bar{r} \leq 0.005$	N_1,M_1^{SU}	
Aitken $0.005 \leq \bar{r} \leq 0.05$	N_2,M_2^{SU},M_2^{BC},M_2^{POM}	N_5,M_5^{BC},M_5^{POM}
Accumulation $0.05 \leq \bar{r} \leq 0.5$	N_3,M_3^{SU},M_3^{BC},M_3^{POM},M_3^{SS},M_3^{DU}	N_6,M_6^{BC}
Coarse $0.5 \leq \bar{r}$	N_4,M_4^{SU},M_4^{BC},M_4^{POM},M_4^{SS},M_4^{DU}	N_7,M_7^{BC}

Table 2: The modal structure of HAM2. N_i denotes the aerosol number of the mode i and M_i^j denotes the mass compound $j \in \{SU, BC, POM, SS, DU\}$ in mode i. The range for $\bar{r}$ give the respective mode boundaries. The abbreviations SU, BC, POM, SS and DU describe the five implemented aerosol components sulphate, black carbon, particulate organic matter, sea salt and dust. The Table was adapted from Stier et al. [2005].

Each of the four size modes has a varying median radius $\bar{r}$ but fixed mode boundaries used for the repartitioning between the modes. The standard deviations σ_i are set constant. For the Nucleation, Aitken and Accumulation mode, it is set to $\sigma_i = 1.59$. For the Coarse mode, which is the largest of the four, the value is set to $\sigma_i = 2.00$ [Wilson et al., 2001]. The characteristics of each mode can be modified by either aerosol dynamics, such as coagulation, or by thermodynamical processes. An example for the latter would be the condensation of sulphate on particles which might turn them from insoluble particles to soluble particles.

3.2 Dust model characteristics

In this study, the dust emission scheme of Tegen [2002] is used. The associated size classes of the mineral aerosol particles range between $0.2\,\mu m$ and $1300\,\mu m$ [Tegen, 2002]. The following chapter provides an insight into the characteristics and parameters of the dust emission scheme.

3.2.1 Vegetation cover and dust source areas

Vegetation cover has a crucial influence onto the wind velocities in the lowermost centimetres of the atmosphere, closest to the surface and thus to the emission of dust by this surface. Especially grass is very successful in inhibiting the emission of dust by reducing the wind speed. By implication, this means that an essential condition for dust source areas is the lack of vegetation cover. As in typical dust source areas the main vegetation is either shrub or grass, these are the only considered plant types for simulating dust emission processes. They are determined using the approach presented in Tegen [2002], by obtaining the relative contributions f_{shrub} and f_{grass} of shrub and grass within a grid cell. Zero refers to no contribution while one refers to maximum contribution.

$$0 \leq f_{shrub} \leq 1 \tag{2}$$

$$0 \leq f_{grass} \leq 1 \tag{3}$$

To determine dust sources, the seasonal cycle of vegetation cover (phenology), snow cover and soil hydrology must be considered [Werner et al., 2002]. The dust source scheme therefore needs to describe the linkage between vegetation cover and the resulting dust source area.

In this master thesis, two different distributions for inferring the dust source area from the vegetation coverage are prescribed and compared. The first one has been developed by [Tegen, 2002] and is based on observational data from satellite records. In the following chapters, it is referred to as "observational vegetation distribution". By contrast, the term "modeled vegetation distribution" refers to a distribution derived from a fully coupled control simulation of the COSMOS Earth System Model (MPIM Hamburg) for either the pre-industrial or last glacial maximum climate boundary conditions.

Observational vegetation distribution

The observational vegetation distribution described by Tegen [2002] is extracted from monthly retrievals of the normalised difference vegetation index (NDVI) from the advanced very high resolution radiometer (AVHRR) satellite instrument [Braswell et al., 1997]. The NDVI is used to infer the monthly mean fraction of the photosynthetically active radiation $FPAR$ which is in turn used to determine the effective surface area for dust emissions A_{eff}.

$FPAR$ is obtained from $NDVI$ using an empirical relationship. This relationship determines the seasonal cycle of vegetation in semi-arid regions (potential source regions) on the account of averaging the normalised difference vegetation index NDVI [Tegen,

2002] and has been stated by Knorr and Heimann [1995] as:

$$FPAR = 1.222 \cdot \left(\frac{NDVI}{0.559} - 0.1566 \right) \tag{4}$$

To obtain the effective surface area A_{eff} for dust emission, Tegen [2002] differentiate between shrub and grass dominated potential source areas:

Grass dominated potential source areas:

$$A_{eff} = \begin{cases} 1 - FPAR & \text{, if } FPAR \leq 0.25 \\ 0 & \text{, otherwise} \end{cases} \tag{5}$$

Shrub dominated potential source areas:

$$A_{eff} = \begin{cases} 1 - FPAR(max_{ann}) & \text{, if } FPAR(max_{ann}) \leq 0.25 \\ 0 & \text{, otherwise} \end{cases} \tag{6}$$

In both cases, it is assumed that dust emission can only occur when the vegetation ratio f and thus the surrogated mean fraction of the photosynthetically active radiation $FPAR$ is below a certain threshold value. Or in other words, dust emission is inhibited if the grass or shrub cover is too dense. This threshold value is set in both cases to 0.25. If $FPAR$ exceeds this value, A_{eff} is set to zero. But a difference between grass and shrub covered areas has to be taken into account as the stems and branches of shrubs are still present and affecting the dust emissions if no leaves are present and thus the $FPAR$ is equal to zero. It is therefore assumed that the effective vegetation cover ratio is constant throughout the year. It equals the yearly maximum of $FPAR$.

Modeled vegetation distribution

For the modeled vegetation distribution, another approach is done. Here, $FPAR$ cannot be obtained from satellite based measurements and thus from $NDVI$. Instead, it is inferred from the simulated leaf are index LAI. The modeled vegetation distribution is produced by the land surface scheme *JSBACH* (Jena Scheme for Biosphere-Atmosphere Interaction in Hamburg) [Raddatz et al., 2007] which has been developed by the Max Planck Institute for Meteorology (MPIM) in Hamburg, Germany. It models the vegetation phenology by simulating the fractional coverage by eight different plant functional types, their growing and mortality [Haese et al., 2013,Raddatz et al., 2007].

The JSBACH module and consequently the vegetation distributions are not based on the empirical analysis of satellite data but are fully modeled and directly extracted from

fully coupled control simulations of the COSMOS. Thus, these COSMOS based vegetation distributions are completely independent from present-day observational data but depend on climate variables, which are given by the ECHAM general circulation model included in the COSMOS. By regarding properties like precipitation, soil wetness and temperature, the locally predominant plant type, its growing and mortality rate and thus its population can be inferred. The whole biosphere is developed by the model itself and biological processes also interact and feed back into the atmosphere model ECHAM. Details for some greenhouse gases, orbital parameters and sea surface temperature are described in chapter 4.2.

From the JSBACH model output, the modeled fraction of the photosynthetically active radiation $FPAR$ is determined by a relationship stated by Monsi and Saeki [1953]:

$$FPAR = 1 - \exp\left(\frac{-0.5}{LAI}\right) \tag{7}$$

3.2.2 Horizontal and vertical dust emission fluxes

Both the horizontal and the vertical flux of dust particles are parametrised according to an emission scheme with 192 different size classes [Marticorena and Bergametti, 1995, Tegen, 2002]. The horizontal flux scheme also includes the explicit simulation of saltation processes [Marticorena and Bergametti, 1995].

Horizontal dust emission flux

The horizontal particle flux G is dependent on the soil particle size and the wind friction velocity [Marticorena and Bergametti, 1995]. Tegen [2002] describes the horizontal particle flux by the total of 192 size classes s_i:

$$G = \frac{\rho_{air}}{g} \cdot U^{*3} \cdot \sum_i \left[\left(1 + \frac{U_t^*(i)}{U^*}\right) \cdot \left(1 - \frac{U_t^{*2}(i)}{U^{*2}}\right) \cdot s_i\right] \qquad | \text{ for } U^* \geq U_t^* \tag{8}$$

Here, ρ_{air} is the air density, g is the gravitational constant, U_t^* is the threshold friction velocity in units of $m\,s^{-1}$ and U^* is the surface wind stress in units of $m\,s^{-1}$. The latter is equal to the wind velocity measured $10\,m$ above the surface [Tegen, 2002].

Vertical dust emission flux

The vertical particle flux F, which can also be described as the vertical dust emission flux, is described by the mass of fine particles passing through a horizontal unit area per unit time [Marticorena and Bergametti, 1995]. As the process of saltation bombardment

plays an important role in the emission of dust, the horizontal particle flux G is included in the estimation of F. Moreover, the effective surface fraction A_{eff} presented in Chapter 3.2.1 is included as well as the effective snow cover fraction A_{snow}. I_Θ represents the soil moisture of the uppermost soil layer and α prescribes the mean over the ratios of the vertical to the horizontal particle flux, which is different for each regarded soil textures (silt, loam, sand, etc.). According to [Tegen, 2002], F can be calculated as:

$$F = \alpha \cdot I_\Theta \cdot A_{eff} \cdot (1 - A_{snow}) \cdot G \tag{9}$$

The soil moisture I_Θ is a value between zero and one and gets equal to zero if the soil moisture is larger than 99 % of the soil capacity. Vice versa, I_Θ is equal to one if the soil moisture is smaller than 99 %. Hereby, the vertical particle flux F gets equal to zero if the soil is saturated with water, meaning that maximum soil moisture inhibits the emission of dust into the atmosphere.

4 Results and discussion

4.1 Simulation characteristics

In this study, the data of six simulations is analysed. The simulations deviate in terms of model resolution, climate boundary conditions and prescribed vegetation distribution. For each of these three characteristics, two possible options exist: Either modeled or observational vegetation distribution, either present-day or last glacial maximum boundary conditions and either T31L19 or T63L31 model resolution. For the T31L19 resolution all four possible simulations are carried out. To distinguish these, the simulations are assigned to abbreviations representing the climate conditions. PD refers to present-day, while LGM refers to the last glacial maximum climate conditions. The post posed number yields whether the observational vegetation distribution (1) or the modeled distribution (2) is prescribed.

While the observational vegetation distribution is always modern, the modeled vegetation distribution differs for the different climate conditions. For the present-day, the vegetation distribution is produced by a fully coupled pre-industrial control simulation of the COSMOS. For the Last glacial maximum, the distribution is produced by LGM control simulation. All distributions are produced for the T31L19 model resolution. For the simulations with the T63L31 model resolution, the vegetation distributions are upscaled.

Abbrev.	**Period**	**Vegetation distribution**	**Resolution**	**Simulation time (+Spin up time)**
PD1	Present-day	observed (modern distribution)	T31L19	10 (+2) *years*
PD2	Present-day	modeled (modern distribution)	T31L19	10 (+2) *years*
LGM1	Last glacial maximum	observed (modern distribution)	T31L19	10 (+2) *years*
LGM2	Last glacial maximum	modeled (LGM distribution)	T31L19	10 (+2) *years*
PD2-T63	Present-day	modeled (modern distribution)	T63L31	10 (+2) *years*
LGM2-T63	Last glacial maximum	modeled (LGM distribution)	T63L31	10 (+2) *years*

Table 3: Overview over the different simulations and their characteristics

For the T63L31 resolution, only the two simulations comprising the modeled vegetation distribution are carried out. To distinguish the runs with same characteristics but different resolutions, the T63L31 runs are named PD2-T63 and LGM2-T63.

T31 and T63 describe the horizontal size of a single grid cell in the used Gaussian grid. L19 and L31 represent the number of vertical layers in the model. For T31, each grid cell has a fixed length of ∼3.75° both longitude and latitude. L19 refers to 19 atmospheric layers from the surface the 0.1 hPa level. For T63L31, each grid cell is 1.875° longitude × ∼1.875° latitude and the model features 31 atmospheric layers, also from the surface the 0.1 hPa level. Consequently, the T31L19 resolution is comparatively coarse in horizontal and vertical resolution, compared to the T63L31 one.

Each simulation comprises ten simulated years and two years of model spin up. This spin up period is necessary as the model needs time to balance out the processes in the atmosphere. This is necessary as the initial atmospheric conditions for the model are prescribed arbitrarily (but each time in an identical manner) and the simulation takes time to level off before it moves towards stable and thus reliable results. The model specific characteristics are listed in Table 3.

4.2 Climate scenario conditions

Characteristic	**Values**	
	Present-day (PD1,PD2)	**Last glacial maximum** (LGM1, LGM2)
Period	1979-1996	∼ 21,000 yr bp
SST	AMIP II	GLAMAP
$c(CO_2)$	348 ppm	185 ppm
$c(CH_4)$	1650 ppb	350 ppb
$c(N_2O)$	306 ppb	200 ppb
Eccentricity	0.016715	0.018994
Obliquity	23.441°	22.949°
Precession	102.70°	114.42°

Table 4: Overview of the basic climate conditions of the applied present-day and last glacial maximum simulations. This Table is partly adapted from Carlsen [2014]

The boundary conditions for the two simulated climates (PD, LGM) have been partly adapted from Carlsen [2014] and are depicted in Table 4. For the present-day simulations, both the mean seasonal cycle of the sea surface temperatures (SST) and the sea ice coverage (SIC) (from the period of 1979 to 1996) are adapted from the Atmosphere Model Intercomparison Project II (AMIPII). Table 4 also depicts the mixing ratios of the three major greenhouse gases carbon dioxide (CO_2), methane (CH_4) and laughing gas (N_2O). The mixing ratio of CO_2 is set to 348 ppm, which represents the mean state of the period from 1979 to 1996.

The settings for the last glacial maximum simulations are chosen accordingly to the Paleoclimate Modeling Intercomparison Project 3 (PMIP3) [Braconnot et al., 2012]. A crucial difference to the present-day simulations is the change in orbital parameters, which lead to a changed solar radiation flux distribution onto the Earth. Hereby, the energy balance and the resulting back radiation of the Earth are altered, leading to a change in climate. Also the changed concentrations of greenhouse gases lead to a change of the radiative balance. As these have been generally lower during the last glacial maximum, also the surface temperature of the Earth has been lower than for the present-day. The mean seasonal cycle of the SST and the SIC are adapted from the Glacial Atlantic Ocean Mapping (GLAMAP) [Schäfer-Neth and Paul, 2003]. The large glacial ice sheets have been prescribed in these simulations, too, and the related reduction of the sea level by 116 m required an adjustment of the land sea mask for the LGM simulations.

The boundary conditions of the COSMOS control simulation that produced the modeled present-day vegetation distribution, differ partially from the boundary conditions of the present-day simulation carried out in this master thesis and described in Table 4. The COSMOS simulation uses pre-industrial boundary conditions instead of present-day conditions like PD1 and PD2. While the concluding change of the orbital parameters is negligible, the differences of the greenhouse gases are large enough to affect the modeled vegetation coverage. Table 5 depicts the greenhouse gas concentrations for the PD1 and PD2 simulations and for the pre-industrial COSMOS simulation [personal communication with M. Werner]:

Characteristic	**Values**	
	Present-day (PD1,PD2)	**COSMOS** (pre-industrial)
Period	1979-1996	pre-industrial
$c(CO_2)$	348 ppm	280 ppm
$c(CH_4)$	1650 ppb	760 ppb
$c(N_2O)$	306 ppb	270 ppb

Table 5: Difference of the greenhouse gas concentrations for the PD1, PD2 simulation and for the pre-industrial COSMOS simulation that produced the modeled vegetation distribution

Thus, differences between the modeled and the observational present-day vegetation distribution result very likely from these different boundary conditions. By contrast, the boundary conditions for the LGM COSMOS simulation are identical to the boundary conditions of the last-glacial maximum simulations carried out in this master thesis (LGM1, LGM2).

4.3 Specific source regions

The world map in Figure 4 highlights regions, that are assumed to be areas of strong dust emissions. Among them are the Sahara, central Asia, the Arabian peninsula, Australia, North America and South America. These source regions cover large parts of the land mass and especially comprise desert areas like the Taklamakan and Gobi for central Asia or the Sahara and the Sahel for northern Africa.

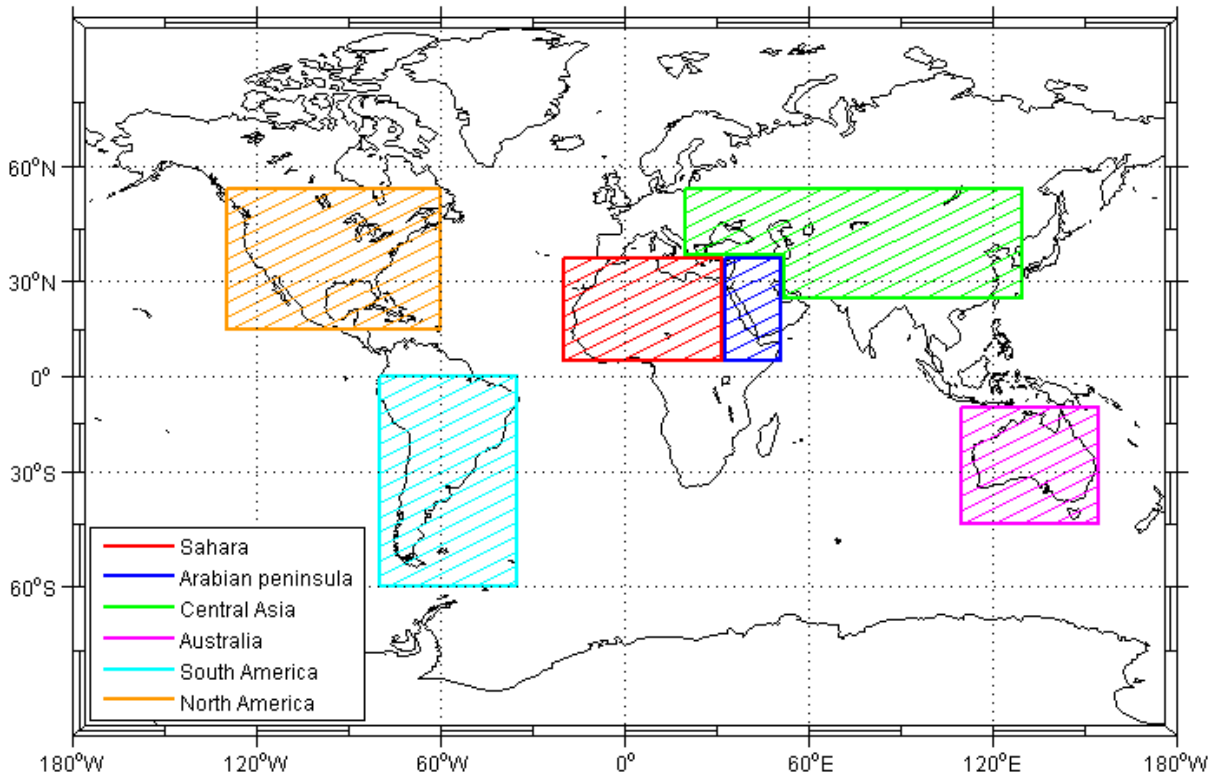

Figure 4: Largest source regions for mineral aerosols. These are the Sahara, the Arabian peninsula, central Asia, Australia North America and South America.

Source region	Meridional extension	Zonal extension
Sahara	5°N - 37°N	20°W - 32°E
Arabian peninsula	5°N - 37°N	33°E - 51°E
Central Asia	25°N - (38°N)- 55°N	25°E - (52°E) - 130°E
Australia	45°S - 10°S	110°E - 155°E
South America	60°S - 0°	80°W - 35°W
North America	15°N - 55°N	130°W - 60°W

Table 6: Overview of the meridional (south to north) and zonal (east to west) extensions of the dust emission regions highlighted in Figure 4. The values are partly adopted from Carlsen [2014].

Table 6 yields an overview of the zonal and meridional extensions of the specified source

areas. The information is adapted from Carlsen [2014]. An additional source region for North America is defined and the central Asian source region is extended to the west, covering parts of eastern Europe. These adaptions have been done to improve the estimation of source areas and their dust emission and to reduce the residual dust emissions of the remaining land mass in the following analysis.

4.4 Annual mean global emissions and depositions

4.4.1 T31L19

The annual mean global emissions and depositions are determined. Table 7 of the four different T31L19 simulations are listed in Table 7. It represents values of the annual mean over the ten simulated years in units of $Mt \cdot yr^{-1}$. Concerning the emission, the Table includes the results for the source regions specified in Chapter 4.3. For the deposition values, the three different types of dust deposition, described in Chapter 2.1.3, are listed. The comparison of the annually and globally summed emission to the corresponding deposition serves as a test for the dust mass conservation during transport. Regarding the results for all simulations, displayed by Table 7, the deviations from total emission to deposition are below 1% and thus the values are in good agreement and each simulation produces conclusive results.

Source region	**Mean emission values** $[Mt \cdot yr^{-1}]$			
	PD1 (observational)	**PD2** (modeled)	**LGM1** (observational)	**LGM2** (modeled)
Total	851±57	817±79	1619±220	2519±259
Sahara	386±43	353±90	850±153	779±136
Central Asia	234±34	339±36	524±99	1396±182
Arabian peninsula	23±5	18±3	53±8	53±12
Australia	121±17	94±9	150±26	53±2
South America	7±1	9±1	8±1	181±18
North America	4±1	0±0	2±1	22±4
Rest	79±23	4±14	31±15	36±9
Deposition type	**Mean deposition values** $[Mt \cdot yr^{-1}]$			
Total	848±67	821±83	1619±225	2519±276
Dry deposition	94±84	99±99	213±31	268±44
Sedimentation	373±30	349±42	699±101	926±104
Wet deposition	382±29	372±33	706±94	1225±128

Table 7: Results and standard deviations for the simulated PD and LGM multi-year mean annual dust emissions and depositions for both the observational and the modeled vegetation distribution. Specific emission regions are regarded individually, as well as the different deposition types.

The two present-day simulations only differ by the prescribed vegetation distribution. Thus, all deviations are the direct result of the influence of the vegetation distribution onto the emission of dust. Taking the observational vegetation distribution as the best match for the present-day vegetation, the comparison of the PD1 to PD2 data can serve as a quality check for the simulation including the modeled vegetation distribution. The deviation for the total emission is smaller than 5% and consequently the two values can be considered to be in good agreement. The strongest source area for the two present-day simulations is the Sahara followed closely by central Asia for the PD2 simulation. From Table 7, it becomes already clear that even though the global emission is in good agreement, regional emissions may vary significantly between the PD1 and the PD2 simulation.

The annual, total values for the LGM1 simulation increase by a twofold in relation to the PD1 simulation, which can be directly associated to the change of not-vegetation-related boundary conditions, as the observational vegetation distribution is the same for PD1 and LGM1. LGM2 by contrast features a threefold increase of the total emission compared to the PD2 simulation. As the climate conditions are the same as in LGM1 but the vegetation distribution is different, the additional increase can be directly understood as a consequence of this vegetation distribution change.

Source region	**Emission ratio**			
	$\frac{\textbf{PD2}}{\textbf{PD1}}$	$\frac{\textbf{LGM1}}{\textbf{PD1}}$	$\frac{\textbf{LGM2}}{\textbf{PD2}}$	$\frac{\textbf{LGM2}}{\textbf{LGM1}}$
Total	0.960	1.903	3.083	1.556
Sahara	0.915	2.202	2.207	0.917
Central Asia	1.449	2.239	4.118	2.664
Arabian peninsula	0.783	2.304	2.944	1.000
Australia	0.777	1.240	0.564	0.353
South America	1.286	1.143	20.111	22.625
North America	0.000	0.500	∞	11.000
Rest	0.051	0.392	9.000	1.161
Deposition type	**Deposition ratio**			
Total	0.969	1.909	3.068	1.556
Dry deposition	1.053	2.266	2.707	1.258
Sedimentation	0.936	1.874	2.653	1.325
Wet deposition	0.974	1.848	3.293	1.735

Table 8: Results for the ratios of the different, simulated mean annual dust emissions and depositions. These are used to estimate the relative changes between different model runs. Particularly high values are highlighted in red, low values in blue.

Table 8 includes ratios of the data presented in Table 7. It can be used to better infer

the change between the different simulations, source regions and deposition types and to infer if these changes are significant.

The first column represents the ratio of PD2 to PD1. If both vegetation distributions would lead to the identical results, all values in this column would be equal to one. Values above one imply an overestimation of the PD2 data, meaning that it leads to larger results than the PD1 simulation, which serves as a reference here. Lower values refer to an underestimation, meaning, that PD1 produces higher values. As most values are below one, prescribing the modeled vegetation distribution leads to a general underestimation of dust emission, except for central Asia and South America (see red marked values), where the outcome exceeds the PD1 data. The deviations for the global emission and deposition, as well as the sedimentation, wet and dry deposition are below 10%. As this deviation is small, the PD1 and PD2 simulations can be assumed to agree globally. For central Asia and South America, an overestimation can be observed and an underestimation is seen for North America, Australia and the Arabian peninsula.

Column two shows the LGM1 to PD1 ratio for the observational vegetation distribution. Since PD1 and LGM1 include the same (observational) vegetation distribution, the LGM1 to PD1 deviations only occur as a result of the changed boundary conditions for the last glacial maximum simulation, e.g. changed winds, humidity, sea level height and orbital parameters. The global emission (1.903) and deposition values (1.909) imply a twofold increase due to these changed conditions. It can be seen that this increase is not constant for all source regions. For the LGM1 to PD1 ratio, the highest value can be found for the Arabian peninsula (2.304), with similar high values for central Asia (2.239) and the Sahara (2.202). For South America (1.143) and Australia (1.240), the local increase is lower than the global and for North America (0.500), the glacial emissions even decrease.

The variability of the LGM2 to PD2 ratio is much higher. The increase of the total dust emission flux is by a factor three (3.083). Here, the Sahara shows only an increase of 2.207 while the emissions for Australia (0.564) even decrease for the LGM2 simulation. For central Asia, the glacial dust emission increase by a fourfold (4.118) and for South America an increase by a factor 20.111 can be observed.

The fourth column reveals the deviations between the two last glacial maximum simulations. The increase due to the prescription of the modeled vegetation distribution is not constant either but reveals just like the corresponding PD2 to PD1 ratio a higher increase for central Asia (2.664) and especially for North America (11.000) and South America (22.625). In contrast, the emission even drops for the Sahara (0.917) and Australia (0.353).

4.4.2 T63L31

For the analysis of the data produced by the T63L31 simulations, the corresponding simulations with the T31L19 model resolution are used as a comparison. Apart from the different resolutions, these runs are identical. Differences that occur can be directly attributed to the changed model resolution. First, the annual mean global emissions and depositions are compared. Table 9 represents the annual mean over the ten simulated years in units of $Mt \cdot yr^{-1}$.

Source region	**Mean emission values** $[Mt \cdot yr^{-1}]$		**Emission ratio**		
	PD2-T63	**LGM2-T63**	**LGM2-T63 / PD2-T63**	**PD2-T63 / PD2**	**LGM2-T63 / LGM2**
Total	361±142	1528±154	4.232	0.442	0.607
Sahara	176±69	520±75	2.955	0.499	0.668
Central Asia	133±60	813±154	6.113	0.392	0.582
Arabian peninsula	29±14	109±27	3.759	1.61	2.057
Australia	13±6	10±2	0.769	0.138	0.189
South America	2±1	37±5	18.500	0.222	0.204
North America	0±0	3±1	-	-	0.136
Rest	8±4	37±9	4.625	2.000	1.028
	Mean deposition values $[Mt \cdot yr^{-1}]$		**Deposition ratio**		
Total	361±144	1536±165	4.255	0.440	0.609
Dry deposition	28±12	147±14	5.250	0.283	0.549
Sedimentation	141±53	544±46	3.858	0.404	0.588
Wet deposition	193±79	845±105	4.378	0.519	0.690

Table 9: Results and standard deviations for the simulated PD2-T63 and LGM2-T63 multi-year mean annual dust emissions and depositions as well as results for the ratios of the different, simulated mean annual dust emissions and depositions. Specific emission regions are regarded individually as well as the different deposition types. Particularly low values are highlighted in red, high values in green.

The first two columns of Table 9 display the yearly mean emission and deposition values for the PD2-T63 and the LGM-T63 simulations, analogue to Table 7. Again, the deviation between the emission values and the corresponding deposition values is below 1%. While for PD2-T63 the Sahara is the strongest dust emission region, it is central Asia for LGM2-T63. Column three displays the ratio of the LGM2-T63 to PD2-T63 and thus shows the glacial increase of the dust emissions and depositions. Regarding the ratio for the global emission reveals a fourfold increase, which is higher as compared to the threefold increase of the identical simulation with the T31L19 model resolution. Again, the glacial increase is not uniform for the different source areas, as the Sahara shows an increase by a factor 2.955, while central Asia increases by a factor 6.113 and the emissions

from South America even multiply by 18.500. In contrast, the emissions for Australia (0.769) even decrease from PD2-T63 to LGM2-T63. Even though the relative changes deviate, the pattern of this present-day to glacial dust emission change is similar to the PD2 to LGM2 change.

To infer relative changes, that occur only due to the change of the resolution, column four and five show the ratio of the T63L31 to the corresponding T31L19 results. Values above (below) one refer to higher (lower) results for the T63L31 simulation. Comparing the two present-day simulations, the simulation featuring the T63 resolution only produces ∼44% of the corresponding T31L19 global emission value. This is also true for the two biggest source regions, the Sahara (0.499) and central Asia (0.392). For Australia and South America, the emissions even decrease more, reaching only ∼14% and ∼22%, respectively. The Arabian peninsula is the only exception with an increase by a factor 1.61 for the finer T63L31 resolution. The same qualitative observations can be stated for the LGM2-T63 to LGM2 ratio.

Even though the different simulations of this study feature different prescribed vegetation distributions and model resolutions, a general increase of the dust burden and consequently the dust cycle from present-day to last glacial maximum times can be observed. This matches the expectations from marine, terrestrial and ice-core records which indicate a glacial increase of dust depositions [Kohfeld and Harrison, 2001]. The general, glacial increase of dust emissions varies for the different simulations. While it increases by a twofold (1.903) for the simulation featuring the observational vegetation distribution and T31L19 resolution (PD1 to LGM1), it increases by a threefold (3.083) and fourfold (4.232) for the simulations with the modeled vegetation distribution (PD2 to LGM2 and PD2-T63 to LGM2-T63). These different values indicate a model-dependent uncertainty of the results, as these vary only due to a change of resolution but not from a change of boundary conditions. In general, the absolute values for the present-day, global dust emissions are with 851 $Mt \cdot yr^{-1}$ (PD1) and 817 $Mt \cdot yr^{-1}$ (PD2) at the lower limit of the values from other studies (1930 $Mt \cdot yr^{-1}$ [Mahowald et al., 2006a], 1060 $Mt \cdot yr^{-1}$ [Werner et al., 2002]).

The twofold increase from the PD1 to LGM1 simulation can be associated to the change of the climate conditions, because the prescribed vegetation distributions for both simulations are identical and represent observational data from satellite measurements. In contrast, the PD2 and the LGM2 simulations (for both resolutions) each include a modeled vegetation distribution, that was produced by a fully coupled control simulation of the COSMOS Earth System Model and thus take the different vegetation distributions of the present-day and the last glacial maximum into consideration. This study indicates

that the change of the vegetation distribution has an impact of the same order of magnitude onto the dust cycle as the change of the other glacial climate conditions. This matches the results by Tegen [2002], that those climate models simulating the dust cycle during the last glacial maximum, which consider only the increased wind velocities and the weakened hydrological cycle, are underestimating the strong present-day to glacial increase in the dust cycle. According to Werner et al. [2002] and Mahowald et al. [1999], this increased strengthening of the glacial dust cycle is partly related to the changes in vegetation cover, too. While Werner et al. [2002] attribute 10% of the glacial increase to the vegetation cover changes, this master thesis yields a value of ∼62%.

The PD1 and PD2 simulations produce similar outputs for the total emission and deposition with their deviation being lower than 10%. This deviation occurs only due to the differences in the vegetation distributions. With 361 $Mt \cdot yr^{-1}$, the output of the LGM2-T63 simulation falls below the two T31L19 values by more than 50%. This decrease can be attributed directly to the change of the model resolution as it comprises the same characteristics as the T31L19 simulation featuring the modeled vegetation distribution. The same tendency, even though less drastic, can be seen in the study of Carlsen [2014]. Here, the present-day emission value dropped by a factor $\sim \frac{1}{3}$. This decrease due to a finer model resolution contradicts the results from other studies like Gläser et al. [2012]. Gläser stated such a decrease only for one singular simulation and attributed it to an interaction of the coarser resolution with the orography. Usually, emissions are expected to be higher for a finer model resolution as local processes can be better resolved and the maximum wind velocities are locally higher. But where regions of high dust emissivity (e.g. deserts) border regions of high wind speeds (e.g. mountains), a coarser resolution may lead to a mixture of high emissivity and high wind speeds in the grid cell, producing high, simulated emission fluxes.

4.5 Comparison of the vegetation distributions (T31L19)

Because the global distribution of dust emissions is not uniform but changes for the different emission regions, it is of interest to further examine the spatial variations of emissions. Because the presence of bare soil is a prerequisite for the emission of dust, the dust cycle is moreover subject to variations throughout the year. These temporal changes are following the phenology of vegetation and are investigated below.

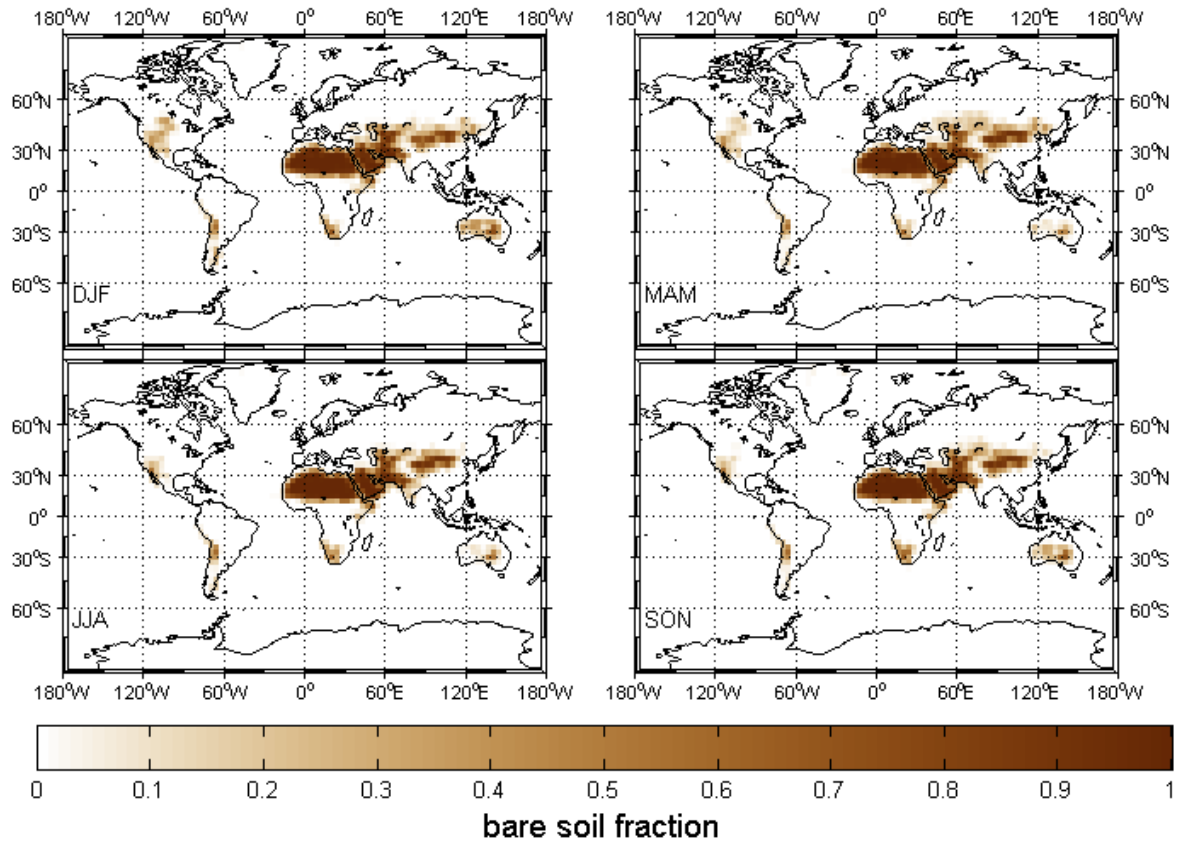

Figure 5: Seasonal mean of the bare soil fraction used for the PD1 and the LGM1 simulation. Seasons are conventionally defined as December-January-February (DJF), March-April-May (MAM), June-July-August, (JJA) and September-October-November (SON).

Dust can potentially be emitted wherever bare soil can be found. Figure 5 shows the seasonal variability of the dust source regions derived from the observational vegetation distribution (see Chapter 3.2.1). The depicted variable is inferred from the (seasonally averaged) monthly effective leaf area index LAI_{eff}, which represents the relative distribution of vegetation. It is in turn inferred from the fraction of photosynthetic active radiation $FPAR$, recorded by satellite. Opposed to this, Figure 6 illustrates the seasonal variability of the dust emission areas inferred from the modeled vegetation distribution. Both figures provide the relative strength of different potential dust source areas. The range of values stretches from zero (no emission) to one (maximum emission). The mod-

eled bare soil fraction for the LGM2 simulation can be found in the Appendix. The same vegetation distributions but up scaled, are used for the T63L31 model resolution.

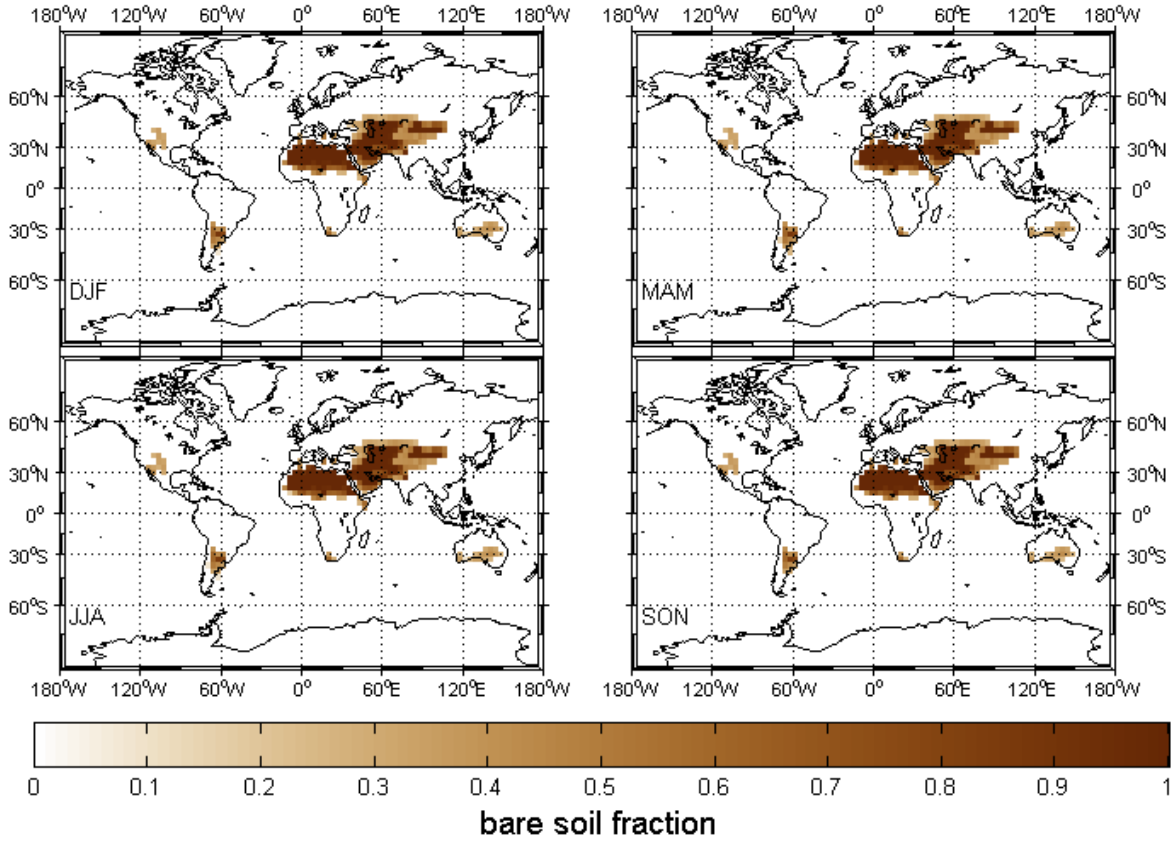

Figure 6: Seasonal mean of the bare soil fraction in the PD2 simulation. Seasons are conventionally defined as in figure 5.

As both the observational and the modeled bare soil fraction should ideally show the same distribution and strength of source regions, the comparison of these model inputs can serve as an indicator for the quality of the PD2 simulation results. If both distributions reveal large deviations from each other, with respect to strength, spatial and seasonal character of the bare soil areas, this could lead to potential variations dust emissions.

Comparing the two bare soil fraction distributions, it becomes distinct that the overall pattern of bare soil fraction is alike. To better display the deviations of the distributions, Figure 7 shows the anomaly of the mean seasonal bare soil fractions from Figure 5 and 6. Taking the observational bare soil fraction as a reference, the Sahara and central Asia show a peripheral region of underestimation. This can be associated with comparatively sharper source region edges of the modeled bare soil fraction.

Regarding central Asia, the bare soil fraction is in general higher for the modeled bare soil

fraction. Vice versa, Africa provides a smaller source area but of equally high bare soil fraction in the centre. In addition, the less pronounced seasonal character of the modeled distribution can be seen. This is especially true for the source regions of Australia and North America, where no significant change of the bare soil fraction throughout the year can be observed. In case of North America, this leads to an underestimation of the bare soil fraction during DJF (December-January-February) and MAM (May-April-March). For Australia, an underestimation takes place during SON (September-October-November) and DJF and an overestimation during MAM and JJA (June-July-August). South America displays a large source area in Patagonia, that is not subject to seasonal variations.

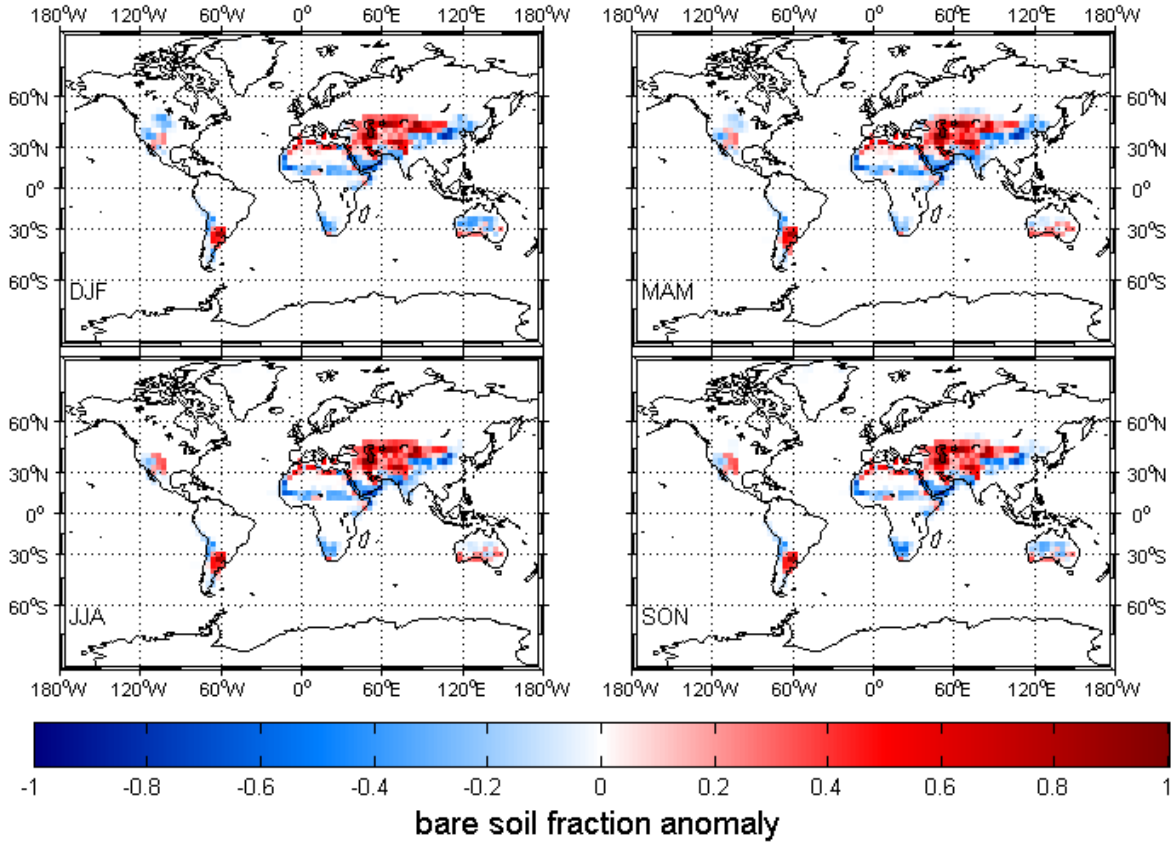

Figure 7: Anomaly of the seasonal mean of the bare soil fraction (modeled minus observational bare soil fraction). Blue shading indicates an underestimation of the modeled fraction in respect to the observational fraction. Red shading indicates an overestimation. Seasons are conventionally defined as in Figure 5.

4.6 Seasonal variability of dust emissions (T31L19)

In the following chapter, the seasonal character of the dust emissions for both the two present-day and the two last glacial maximum simulations are described. Hereby, the focus is put on the data representing the modeled vegetation distribution (PD2, LGM2). The data associated with the observational vegetation distribution (PD1, LGM1) is taken as a reference in anomaly plots, only. All corresponding figures showing the absolute emission and deposition fluxes of PD1 and LGM1 can be found in the Appendix.

4.6.1 Present-day simulation

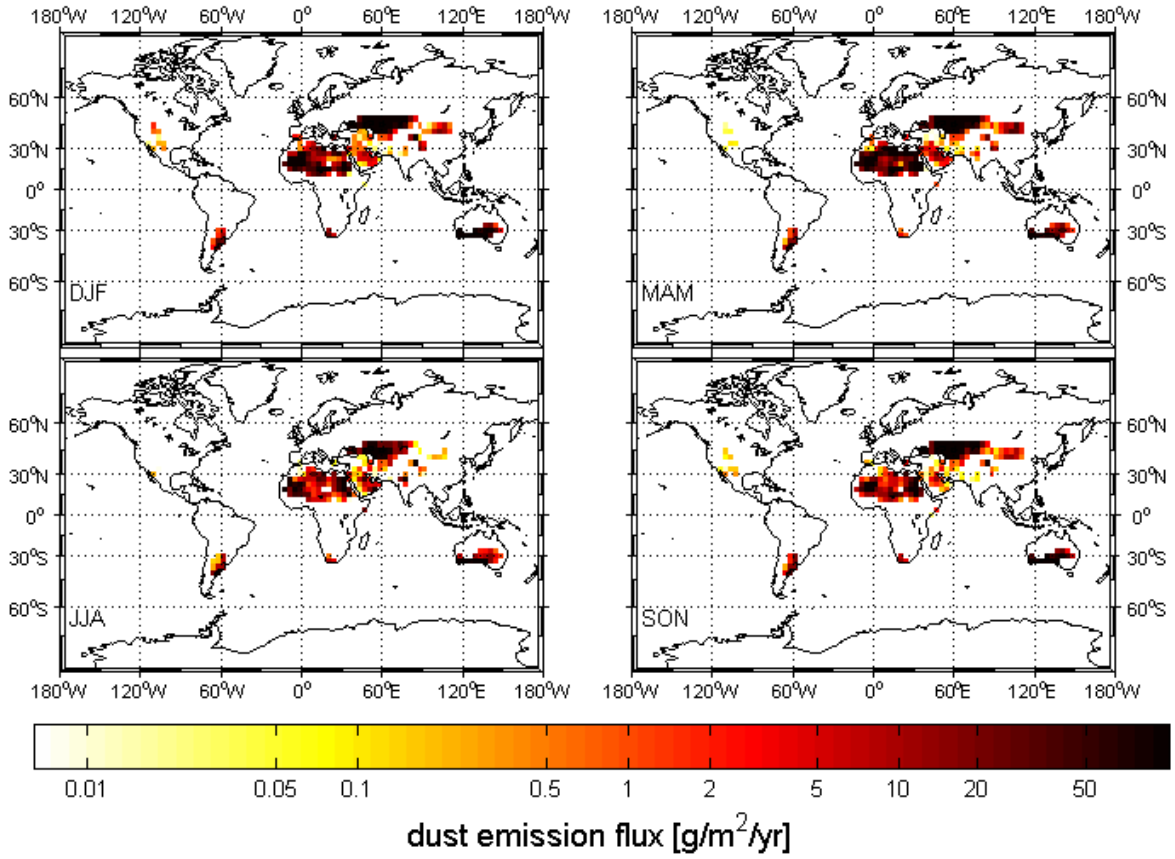

Figure 8: Seasonal mean dust emission fluxes for the PD2 simulation, using the modeled vegetation distribution. Seasons are conventionally defined as in Figure 5.

Figure 8 shows the averaged, seasonal dust emission flux for the PD2 simulation, i.e. the present-day simulation based on the modeled vegetation distribution. The emission flux is here defined as the flow of dust into atmosphere in units of mass per square metre per year.

The major dust emission sources can be recognised in Figure 8. These are located in northern Africa, central Asia, the Arabian peninsula, Australia, North America and South America. The source region in North Africa includes the Sahara but also the Sahel, while

the region in central Asia comprises the deserts Taklamakan and Gobi. A seasonal character of the dust emission can be observed for the Sahara and central Asia, which both reveal an emission maximum in DJF and MAM. For the other regions, seasonal variability is less pronounced.

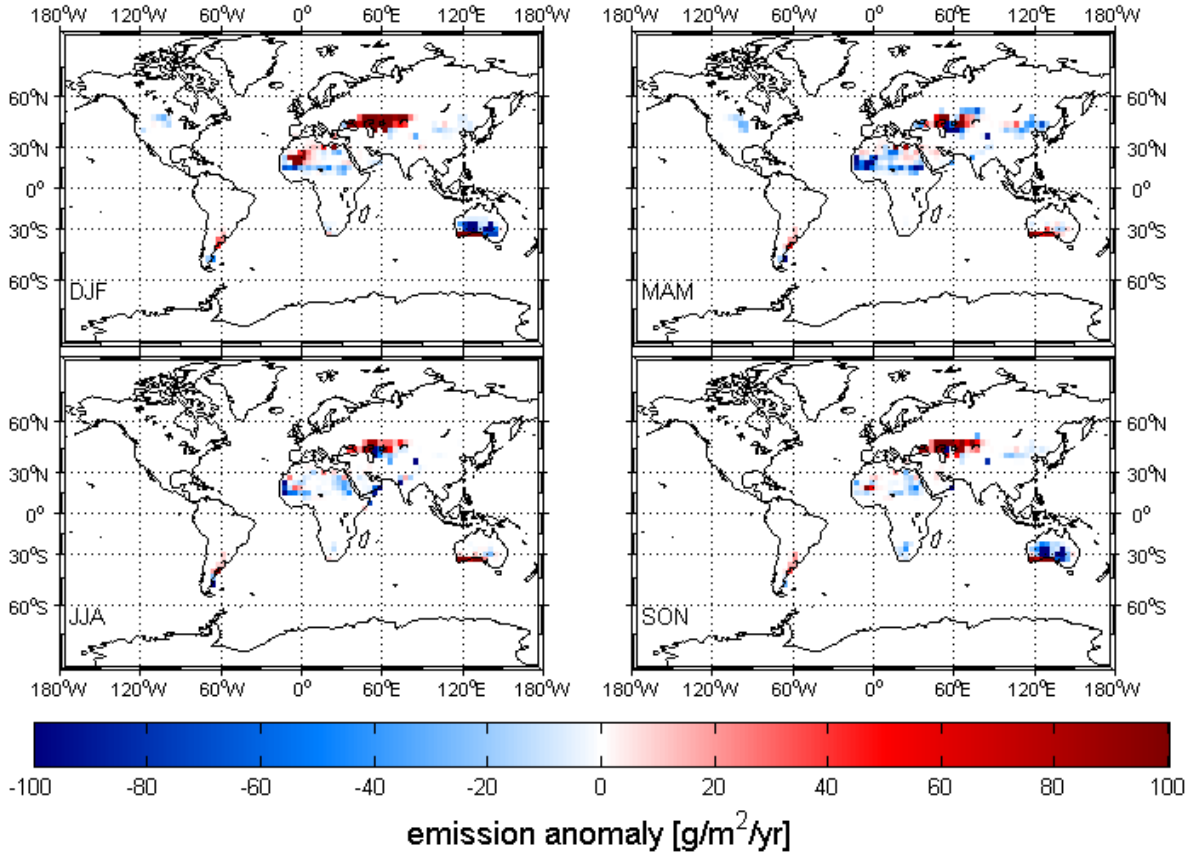

Figure 9: Anomaly for the seasonal mean dust emission fluxes of the two present-day simulations (PD2 minus PD1). Blue shading indicates an underestimation by the PD2 data, taking PD1 as a reference. Red shading indicates an overestimation. Seasons are conventionally defined as in Figure 5.

Figure 9 displays the anomaly of the PD2 data minus the PD1 data. The differences that occur are only due to the different vegetation distributions. Deviations from the reference PD1 are marked as an overestimation (red shading) or as an underestimation (blue shading).

As seen in Figure 9, the specified source regions generally agree but slightly deviate in strength, extension and seasonality. For example, stronger emissions can be stated for central Asia, for South America and the southern coast of Australia, Here, the strength and extension of the source areas are overestimated. On the contrary, the Sahara features lower emissions throughout all seasons but also a partial overestimation during DJF. The emissions in North America and central Australia show an underestimation of the dust

flux only during two seasons. For North America, the emission is underestimated for DJF and MAM, while for central Australia, the emissions are smaller than expected during SON and DJF.

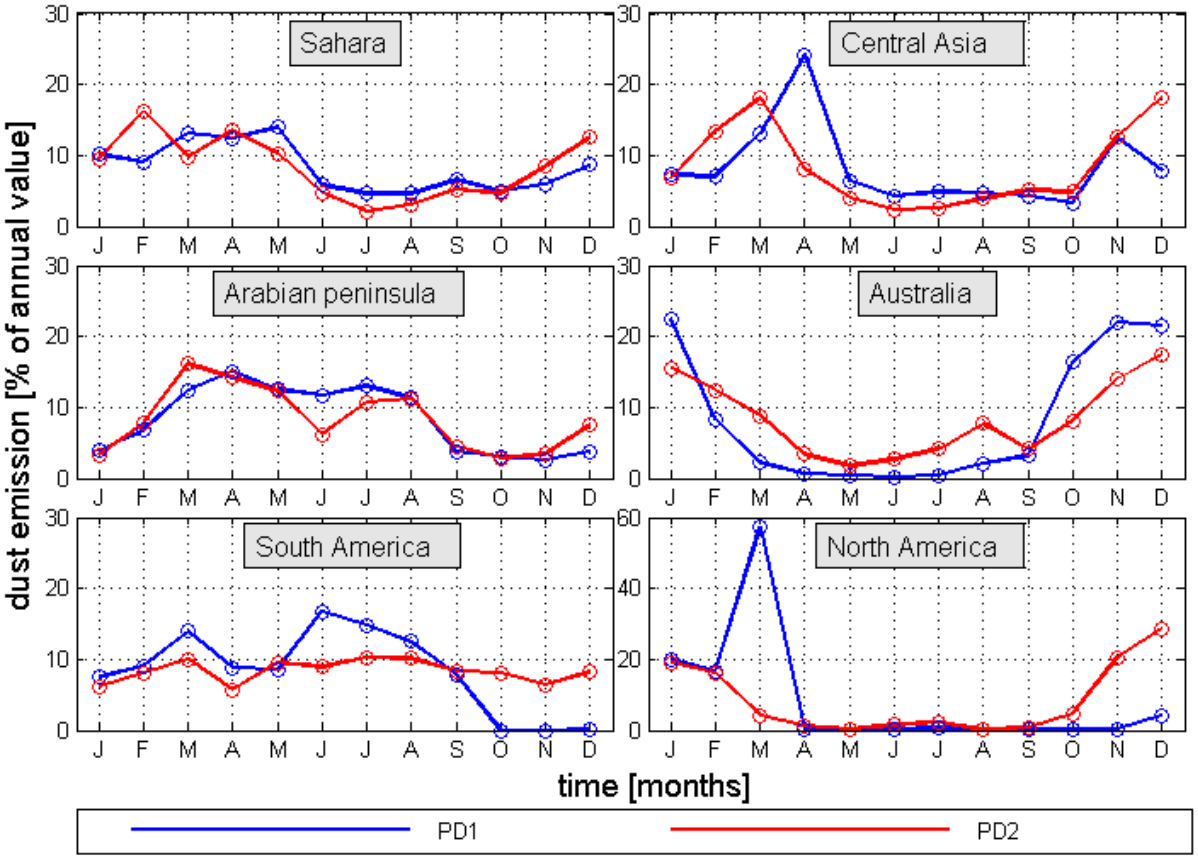

Figure 10: Monthly dust emission for the present-day simulations. Given are the values for the specified source regions Sahara, central Asia, Arabian peninsula, Australia, South America and North America. The regionally and monthly summed emission is given in percentage of the total annual dust emission value.

The seasonal character for the different source regions can be even better inferred from an analysis of monthly emission fluxes. In Figure 10, the regionally and monthly summed, relative contribution to the total annual dust emission is displayed. For a homogeneous emission without any variation throughout the year, a constant value of ∼8% ($=\frac{1}{12}$) would be expected for every month. This can be best observed for South America, where the monthly dust emission never exceeds 10% and seasonal variability almost vanishes. For the source regions on the northern hemisphere, the maximum emission takes place during boreal winter (DJF) to spring (MAM). This can be seen for the Sahara and central Asia. For the Arabian peninsula the period of maximum emissions starts in boreal spring (MAM) and extends until summer (JJA). Australia being on the southern hemisphere, features a maximum emission during austral spring (SON) and summer (DJF). Taking the PD1 data as a reference, central Asia, Australia and North America provide a less distinc-

tive seasonality in the PD2 simulation. For the Sahara, central Asia and North America, a shift of one month (Sahara, central Asia) and two to three month (North America) towards an earlier start of dust emissions within the yearly period can be observed.

4.6.2 Last glacial maximum simulation

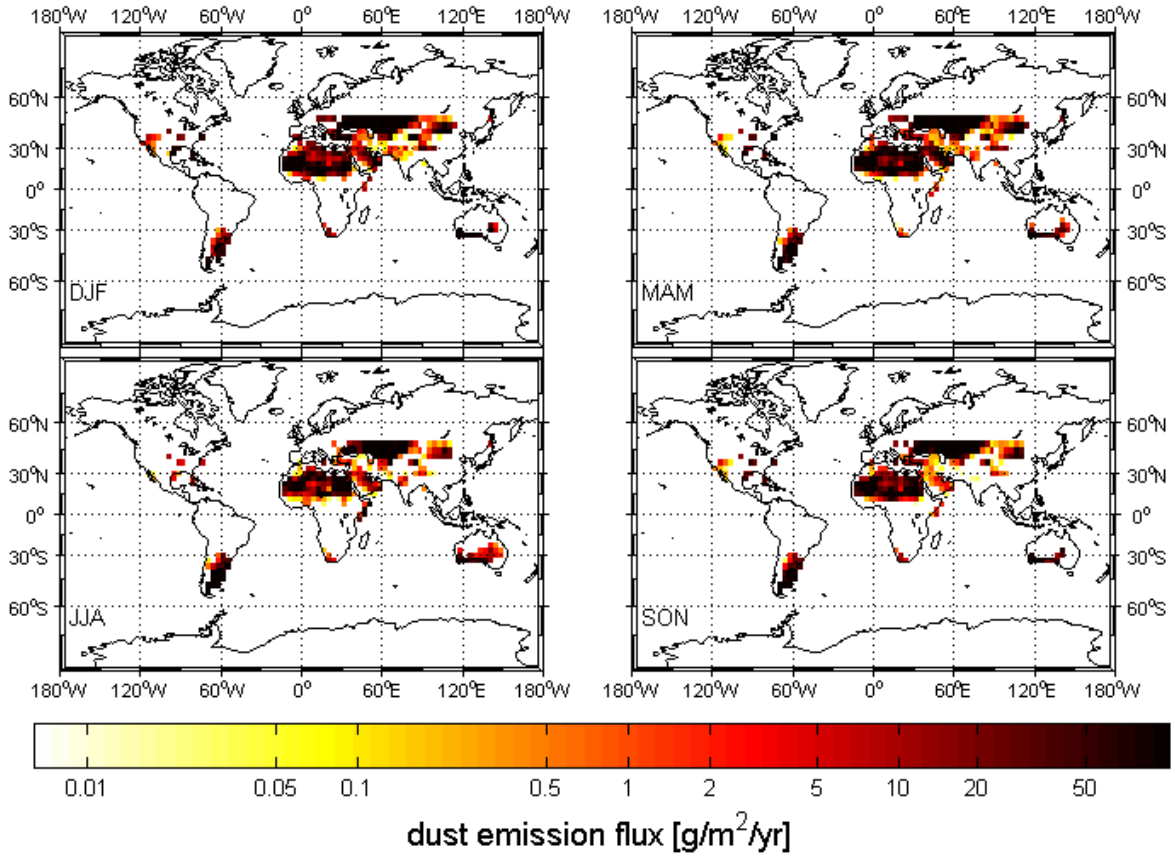

Figure 11: Seasonal mean dust emission fluxes for the LGM2 simulation, using the modeled vegetation distribution. Seasons are conventionally defined as in Figure 5.

In Figure 11 the dust emission fluxes for the LGM2 simulation, including the vegetation distribution from the fully modeled COSMOS simulation can be seen. In general, the emissions have the same spatial distributions as the corresponding present-day emissions (Figure 8). It can be seen that South America and central Asia are stronger emission areas for the last glacial maximum. This can also be seen, in Table 7 and 8. While the global PD2 to LGM2 increase of the dust emissions is of a factor three, the increase for central Asia is by a factor 4.118 and for South America even by a factor 20.111.

Figure 12 displays the anomaly of the LGM2 emission data minus the PD2 data and consequently the changes of the dust emission fluxes in glacial times, using the present-day as a reference. The deviations can in general be associated to the change of the climate conditions. But since the prescribed vegetation distributions are modeled, the

climate conditions additionally include the change of the vegetation distribution and thus the bare soil distribution. The largest increase can be observed for central Asia and South America. But also for the Arabian peninsula and North America the dust emissions increase, while for the Sahara both a partly increase and a partly decrease is visible. For Australia , the emissions generally decrease.

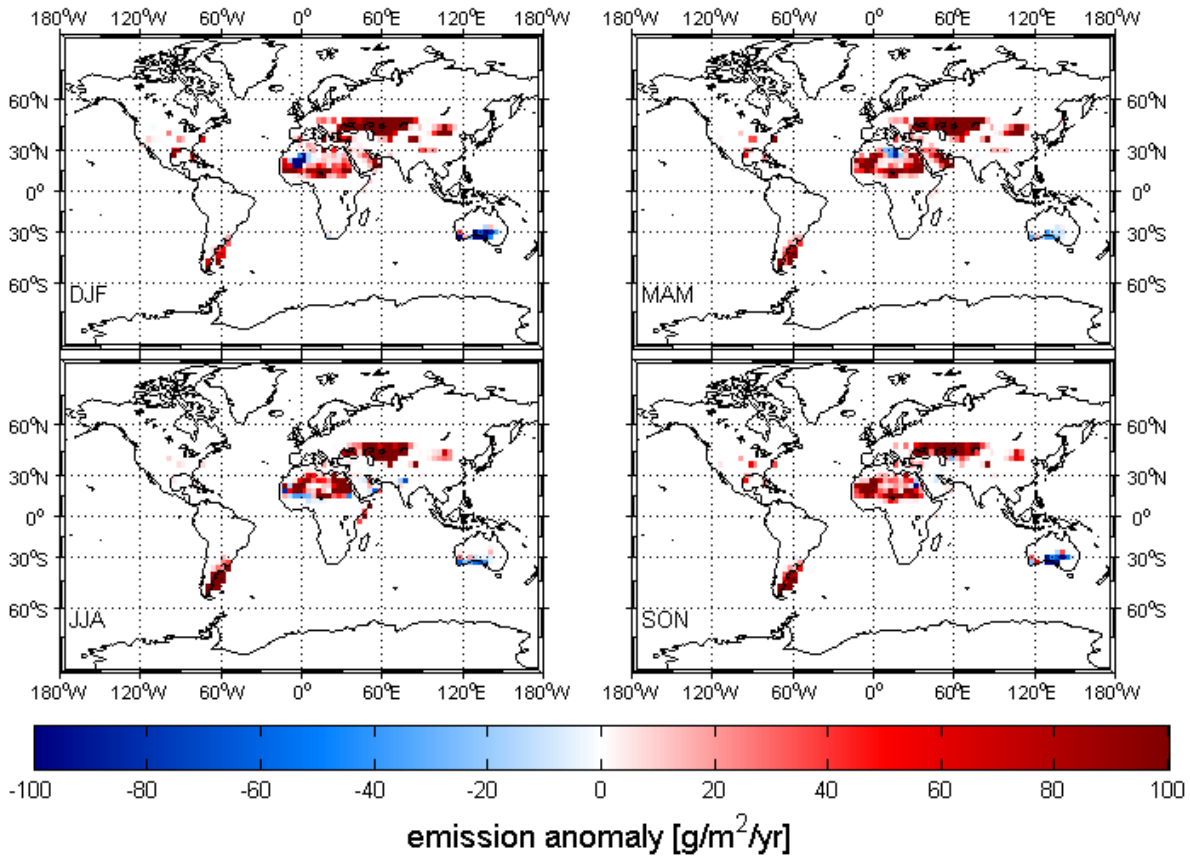

Figure 12: Anomaly for the seasonal mean dust emission fluxes of the two T31L19 simulations, featuring the modeled vegetation distribution (LGM2 minus PD2). Blue shading indicates a decrease of the LGM2 data, taking PD2 as a reference. Red shading indicates an increase. Seasons are conventionally defined as in Figure 5.

Figure 13 shows the regionally and monthly integrated, relative contributions to the regional, annual dust emission. In general, the seasonal dust emission cycles for the PD2 and the LGM2 simulation agree well. The period of maximum emission on the northern hemisphere is from boreal winter (DJF) to spring (MAM). One exception is the shift of the maximum emission period for the Arabian peninsula from boreal winter and spring to spring and summer (JJA). Other exceptions are central Asia and North America, where higher emissions can already be observed in November. On the southern hemisphere, the maximum emission takes place during austral spring (SON) and summer (DJF).

For the Sahara, the seasonality is less pronounced for the LGM2 simulation, as the

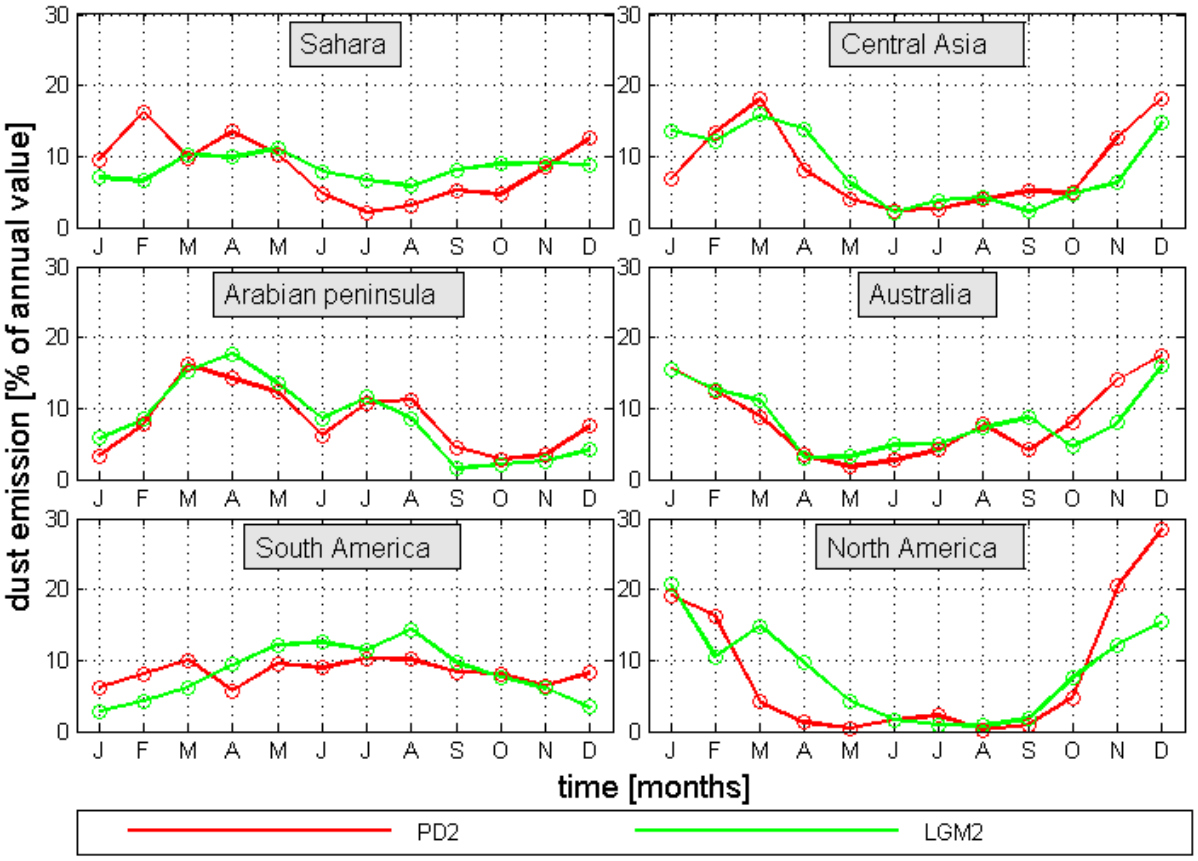

Figure 13: Monthly dust emission for the LGM2 and PD2 simulations. Given are the values for the specified source regions Sahara, central Asia, Arabian peninsula, Australia, South America and North America. The monthly emission is given in percentage of the total annual dust emission value.

monthly values exceed 10% only during MAM. For North America, the period of the maximum dust emission value is lower for the last glacial maximum, but extends to May and August. By contrast, the seasonal character of emissions in South America is more pronounced for the LGM2 simulation, which might result from the generally higher emission values. Though, the glacial dust emissions do not increase uniformly for the different source regions, their seasonal character in the LGM2 simulation correspond closely to the character of the emissions in the PD2 simulation. Figure 44 in the Appendix displays the monthly dust emissions for all four T31L19 simulations in comparison.

Werner et al. [2002] describes the Sahara, Asia and Australia as the strongest dust emission regions for present-day simulations. This is also true for the present-day simulations in this study. But regarding the last glacial maximum simulations including the modeled vegetation distribution, the Sahara features a less intense glacial increase than the global dust cycle (Table 8). As a consequence, central Asia displaces the Sahara as the strongest dust emission area, in the LGM2 simulation. For central Asia, this increase can be attributed partly to a general strengthening and expansion of the potential source

areas. Such an expansion cannot be stated for the Sahara. Here, the increased emissivity must origin from other sources, like increased wind velocities.

The emissions for South America even exceed a glacial increase by a factor 20 (T31L19), which matches expectations by e.g. Lamy et al. [2014]. The PD2 to LGM2 anomaly (Figure 12) displays the fact that Australia is the only emission region, where the glacial emissions decrease compared to the present-day, which is consistent with the findings in Werner et al. [2002].

Though the absolute emission values vary for different simulations, the seasonal character of the different source regions are in good agreement (Figure 10, 13 and 21). The period of maximum emissions is during boreal winter and spring on the northern hemisphere. For the Arabian peninsula, it is shifted to spring and summer. South America, being located on the southern hemisphere, features the emission maximum during austral autumn and fall. Australia is the only region showing major exceptions from this seasonal cycle. For the LGM2 simulation, its maximum emissions take place during austral summer and autumn. Figure 32 in the Appendix displays the seasonal distribution of the (present-day) dust optical thickness, remotely sensed with the Total Ozone Mapping Spectrometer. The dust optical thickness refers to the amount of dust in the atmosphere and does not represent an emission or deposition flux, but is used here as a qualitative comparison for the seasonality of the simulated dust cycle. For emission regions on the northern hemisphere (Northern America, Sahara, Arabian peninsula, central Asia), the highest dust optical thickness can be observed for boreal spring and summer. For the southern hemisphere, only a significant increase for Australia during austral spring and summer can be observed. For the Arabian peninsula and Australia, these observations agree quite well with the simulations, while for North America, the Sahara and central Asia, the observations are delayed by one season. One explanation for this lag might be the fact, that the dust optical thickness is neither equal to an emission nor deposition flux but reveals the amount of dust stored in the atmosphere.

4.7 Seasonal variability of dust depositions (T31L19)

4.7.1 Present-day simulation

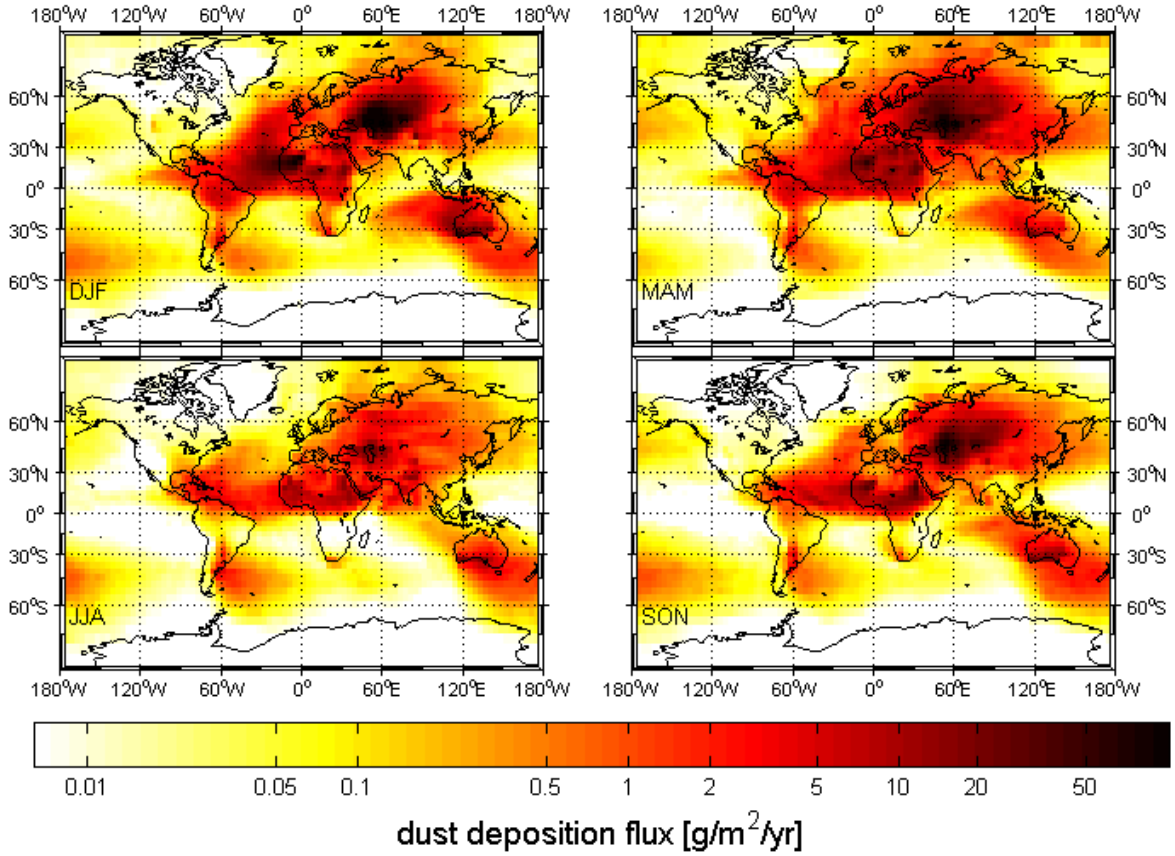

Figure 14: Seasonal mean dust deposition fluxes for the PD2 simulation, using the modeled vegetation distribution. Seasons are conventionally defined as in Figure 5.

Figure 14 shows the averaged, seasonal dust deposition fluxes for the PD2 simulation. As stated in Chapter 2.1.2, most of the deposition takes place close the emission sites. For this reason and because the deposition takes place continuously along the way of transportation, the distribution of dust from the specific emission areas follows mainly the predominant wind patterns.

For example, dust from South America, Australia and South Africa is transported eastwards between 30°S and 60°S according to the west wind drift in this area. But dust from Australia is also carried to the north-east into the Indian Ocean. Dust originating from central Asia is spread over the entire continent and even into the Indian Ocean in the south, the Arctic Ocean in the north and the Pacific Ocean in the west. Saharan dust is transported across the Atlantic Ocean and towards the Caribbean and South America, reaching even the Pacific Ocean. In the north, dust from the Sahara reaches northern Europe and even Greenland in MAM. The emissions from the Arabian peninsula travel

south-east into the Indian Ocean. These observations agree with the dust transport pattern already indicated in Figure 2, based on the TOMS aerosol index values by Kohfeld and Tegen [2007].

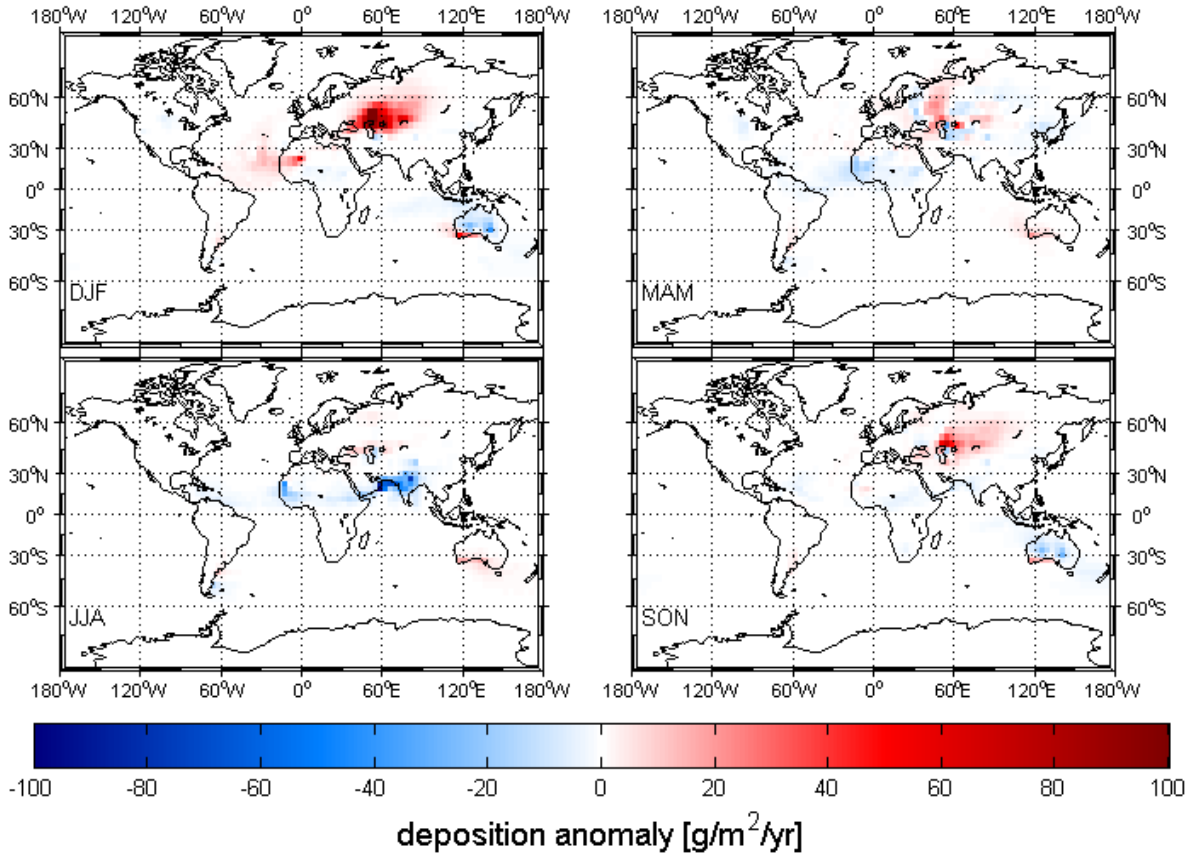

Figure 15: Anomaly for the seasonal mean dust emission fluxes of the two present-day simulations (PD2 minus PD1). Blue shading indicates an underestimation by the PD2 data, taking PD1 as a reference. Red shading indicates an overestimation. Seasons are conventionally defined as in Figure 5.

Figure 15 displays the anomaly of the mean seasonal dust deposition fluxes (PD2 - PD1). For central Asia a large underestimation can be observed in SON and DJF for PD2 which is conform to the difference in emission seasonality. Due to the fact that transport and deposition can last up to days or weeks, a less intense overestimation still can be seen in MAM. Saharan depositions over Sahara itself but also over the Atlantic Ocean are overestimated during DJF but underestimated from MAM to JJA. An underestimation for central Australia in SON and DJF can be detected, too, but also a general overestimation for the Australian southern coast.

4.7.2 Last glacial maximum simulation

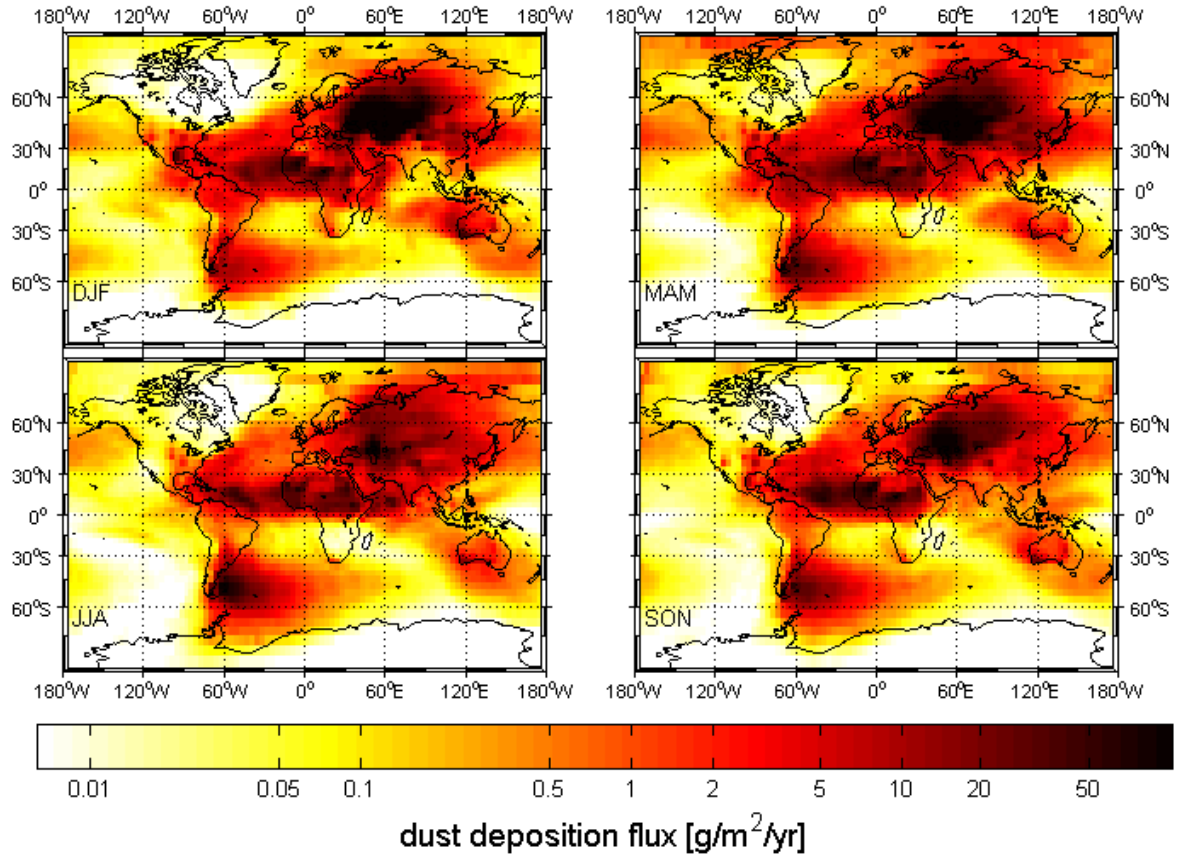

Figure 16: Seasonal mean dust deposition fluxes for the LGM2 simulation, using the modeled vegetation distribution. Seasons are conventionally defined as in Figure 5.

The averaged, seasonal dust deposition fluxes for the LGM2 simulation, that can be seen in Figure 16, are in general more intense than in the corresponding present-day simulation (Figure 14) which is in agreement with the simulated higher LGM emissions. Additionally, dust is transported further and even distributed into polar regions. Dust from central Asia reaches the Arctic Ocean and Greenland, while dust from South America approaches Antarctica and the Indian Ocean. Dust from the Sahara reaches not only South America, central America and the Pacific Ocean but also North America. This is also true for dust from central Asia, which is transported over the Pacific Ocean.

Analogue to Figure 12, Figure 17 depicts the anomaly of the LGM2 minus the PD2 deposition data and consequently the changes of the dust deposition fluxes in glacial times, using the present-day simulation as a reference. The deviations result from the change of climate conditions and the different modeled vegetation distributions. The latter include also the change of the climate conditions and thus their impact onto vegetation coverage.

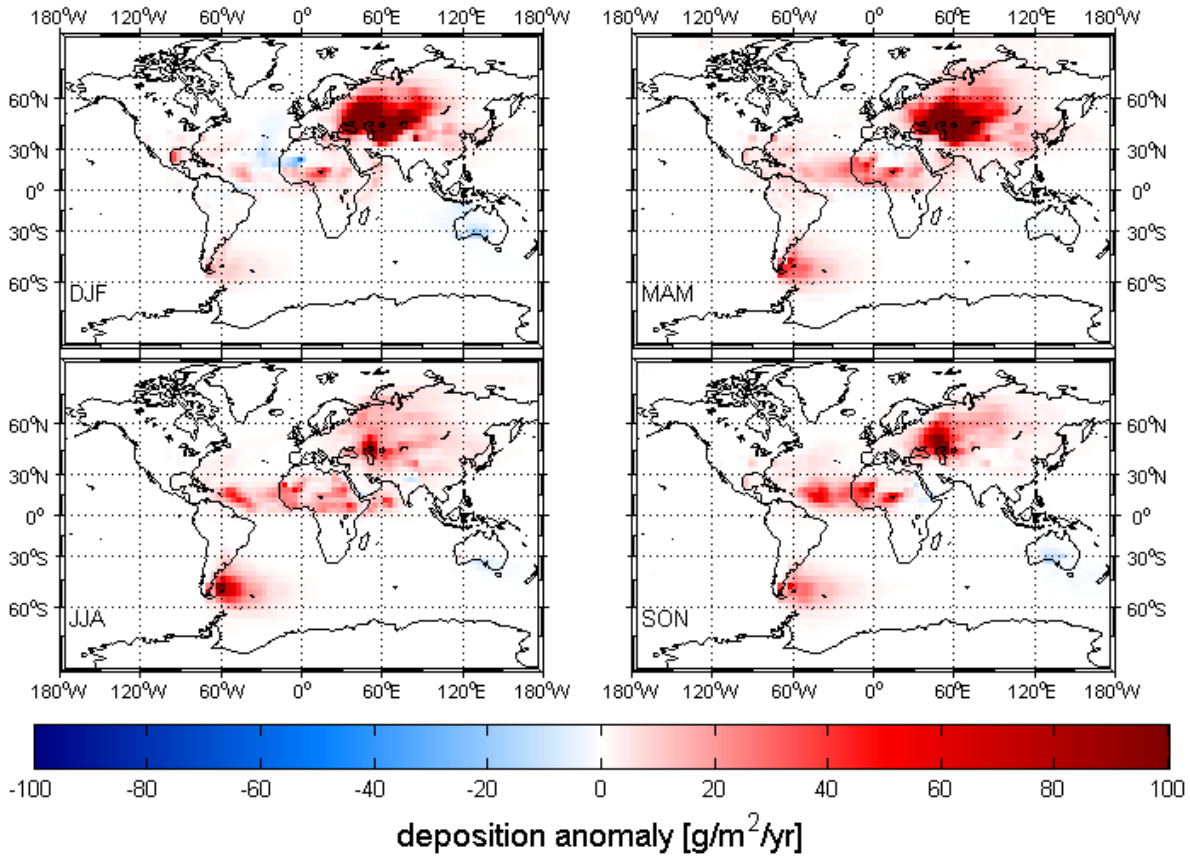

Figure 17: Anomaly for the seasonal mean dust deposition fluxes of the two T31L19 simulations, featuring the modeled vegetation distribution (LGM2 minus PD2). Blue shading indicates a decrease of the LGM2 data, taking PD2 as a reference. Red shading indicates an increase. Seasons are conventionally defined as in Figure 5.

The largest glacial increase of dust depositions occurs over central Asia. Here, a change in seasonality can be observed, as central Asia features a less intense increase for JJA and SON. Consequently, the glacial increase is especially intense for the seasons of maximum dust emissions. Dust originating from South America also shows larger depositions fluxes due to the west wind drift over the Atlantic Ocean. The increase is strongest during MAM and JJA. For dust deposition fluxes coming from North America, no reliable observations can be stated as Saharan dust transported across the Atlantic Ocean might mask the deposition deviation. In general, deposition of Saharan dust is more intense for LGM2 but features also a regional decrease during DJF. Australia, being the only exception, provide generally lower dust depositions than in the corresponding present-day simulation.

From Figure 18, showing the LGM2 to LGM1 anomaly, it can be inferred that both central Asia and South America are much stronger emission regions for the LGM simulation with the modeled vegetation distribution. This is in agreement with previous observations. While for central Asia less dust is deposited over the source region itself, for South America, the major deviation can be found over the Atlantic Ocean, close to

the coast of South America.

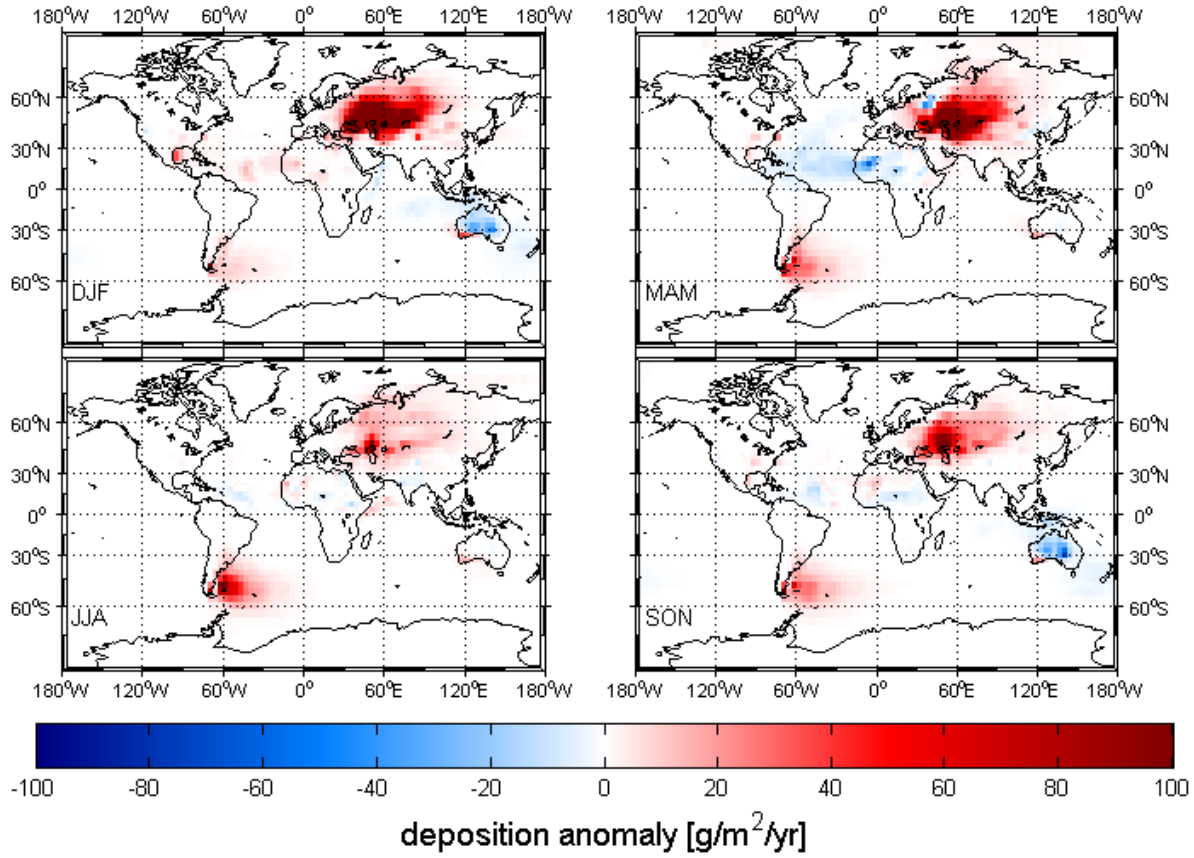

Figure 18: Anomaly for the seasonal mean dust deposition fluxes of the two last glacial maximum simulations (LGM2 minus LGM1). Blue shading indicates a decrease of the LGM2 data, taking LGM1 as a reference. Red shading indicates an increase. Seasons are conventionally defined as in Figure 5.

Just like in the corresponding present-day anomaly (Figure 15), dust depositions in the Atlantic Ocean, originating from Sahara are lower than in the simulation with the observational vegetation distribution, except for DJF. Equally, depositions in the Indian and Pacific Ocean originating from Australia are lower in SON and DJF. Since both simulations feature the same climate conditions, the detected deviations of the dust depositions are only due to the influence of the different prescribed vegetation distributions.

4.8 Seasonal variability of dust emissions (T63L31)

In this chapter, the results from the simulations with the modeled vegetation distribution and the T63L31 model resolution are presented. The simulations are directly compared to the corresponding simulations with the coarser T31L19 model resolution.

4.8.1 Present-day simulation

The PD2-T63 simulation (Appendix, Figure 37) shows the same pattern of dust emissions as the corresponding T31L19 simulation (Figure 8). But since the absolute, global and regional emission values strongly vary, the deviations between the two simulation results are analysed in detail, here.

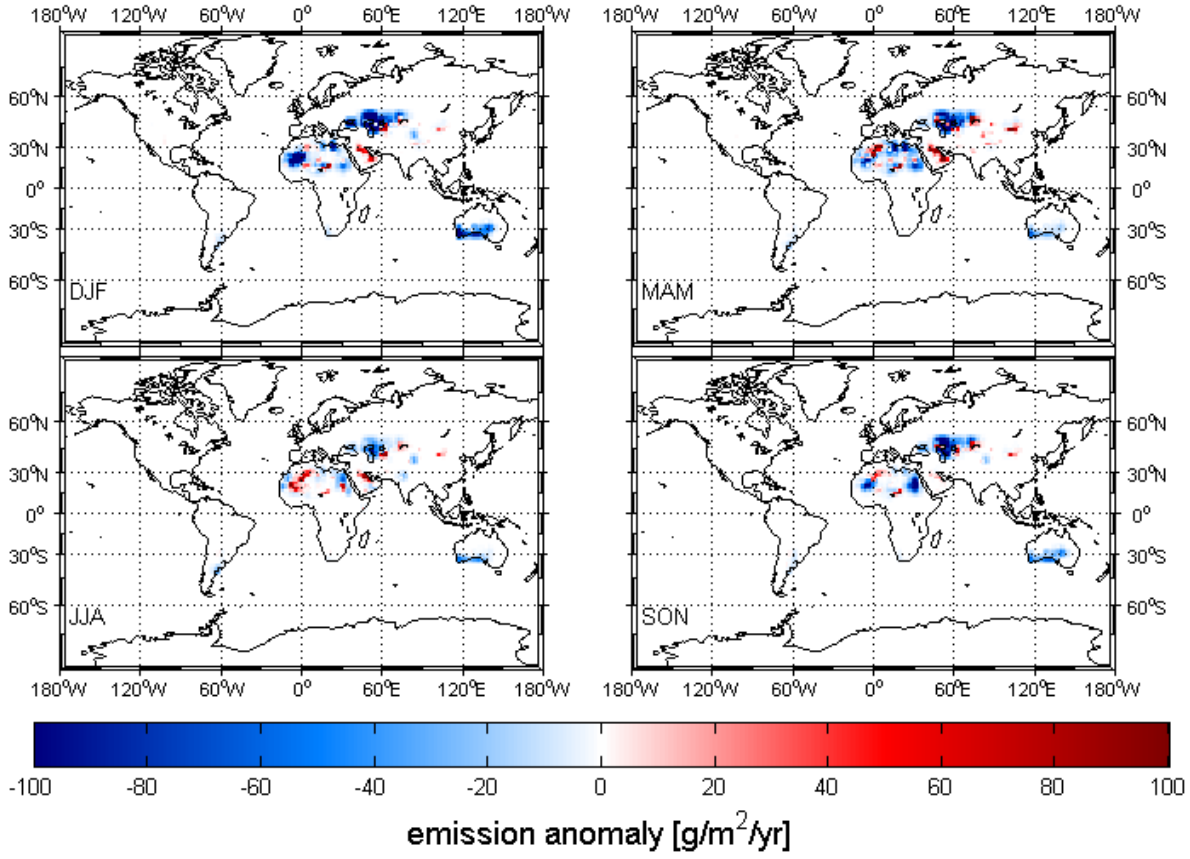

Figure 19: Anomaly for the seasonal mean dust emission fluxes of the two present-day simulations (PD2-T63 minus PD2). Blue shading indicates a decrease of the PD2-T63 simulation, taking PD2 as a reference. Red shading indicates an increase. Seasons are conventionally defined as in Figure 5.

The major deviations of the two simulation results can be found for the source regions of Sahara, central Asia and Australia. Here, regions of decreased dust emissions can be observed for the T63 simulation. Only minor and small areas of higher dust emissions are present for Sahara and central Asia, while for the Arabian peninsula, a seasonal increase

of dust emissions during DJF and MAM can be stated. As expected, both results agree with the data from Table 9, stating the Arabian peninsula to be the only region with an increase of dust emissions. The deviations are not equal for all seasons. For the Sahara and central Asia, the differences to the T31L19 simulation are less intense for the period of minimum dust emissions (JJA).

4.8.2 Last glacial maximum simulation

The last glacial maximum emission fluxes of the T63L31 simulation with the modeled vegetation distribution (Appendix, Figure 39) yield basically the same dust emission pattern as the corresponding T31L19 simulation (LGM2, Figure 11), with the same dust emission areas and an increased emission in central Asia and South America.

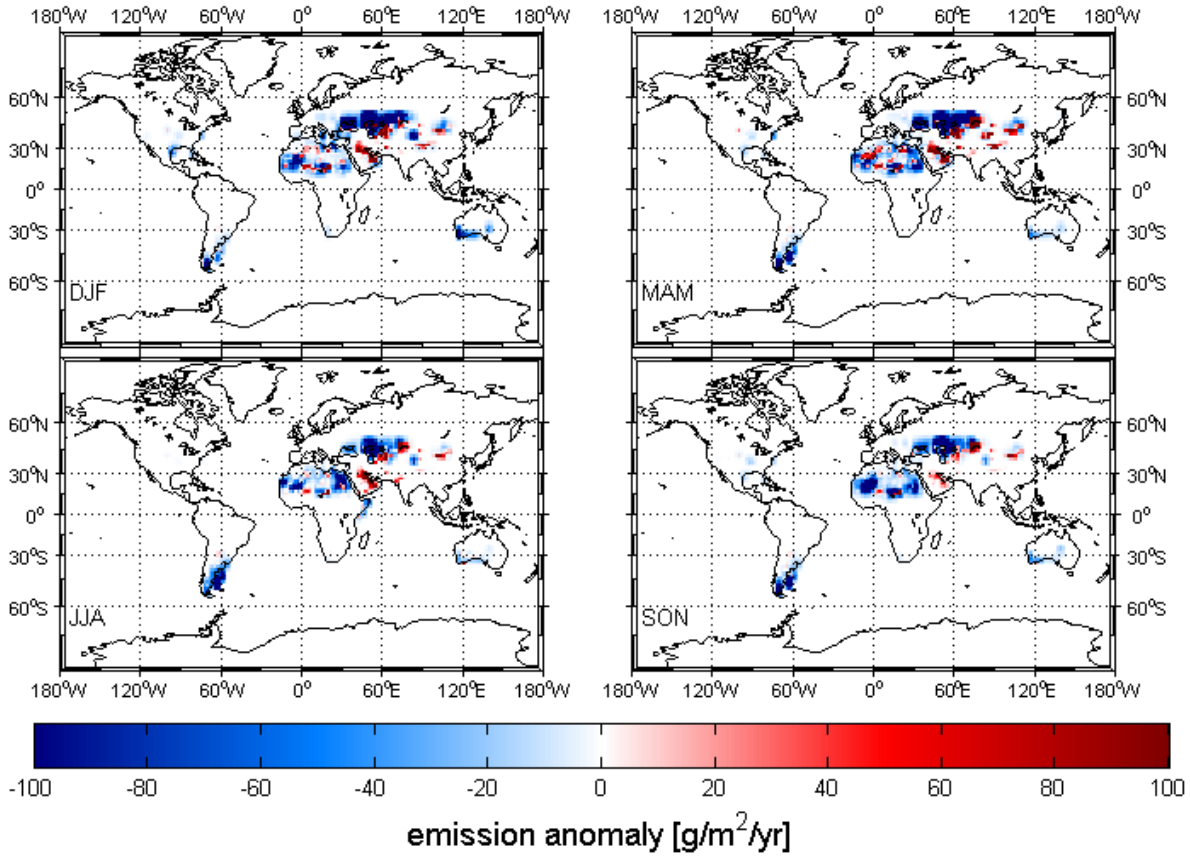

Figure 20: Anomaly for the seasonal mean dust emission fluxes of the two last glacial maximum simulations (LGM2-T63 minus LGM2). Blue shading indicates a decrease of the LGM2-T63 simulation, taking LGM2 as a reference. Red shading indicates an increase. Seasons are conventionally defined as in Figure 5.

The deviations between LGM2-T63 and the associated T31L19 simulation can be seen in Figure 20, showing the anomaly for the two simulations. LGM2 is taken as a reference. In general, a decrease of emissions for all source regions can be observed. The only exceptions

are North America, where the decrease of the already low emissions might not be distinct and the Arabian peninsula. The decrease is not uniform across the areas and for central Asia, the Arabian peninsula and the Sahara, even local increases of dust emission can be seen. As the climate conditions and the vegetation distributions are the same for both simulations, the deviations between the two simulations can be associated directly to the different model resolutions. According to Carlsen [2014] locally higher emissions can be attributed to the better resolution of local emission processes and local peaks in wind velocities.

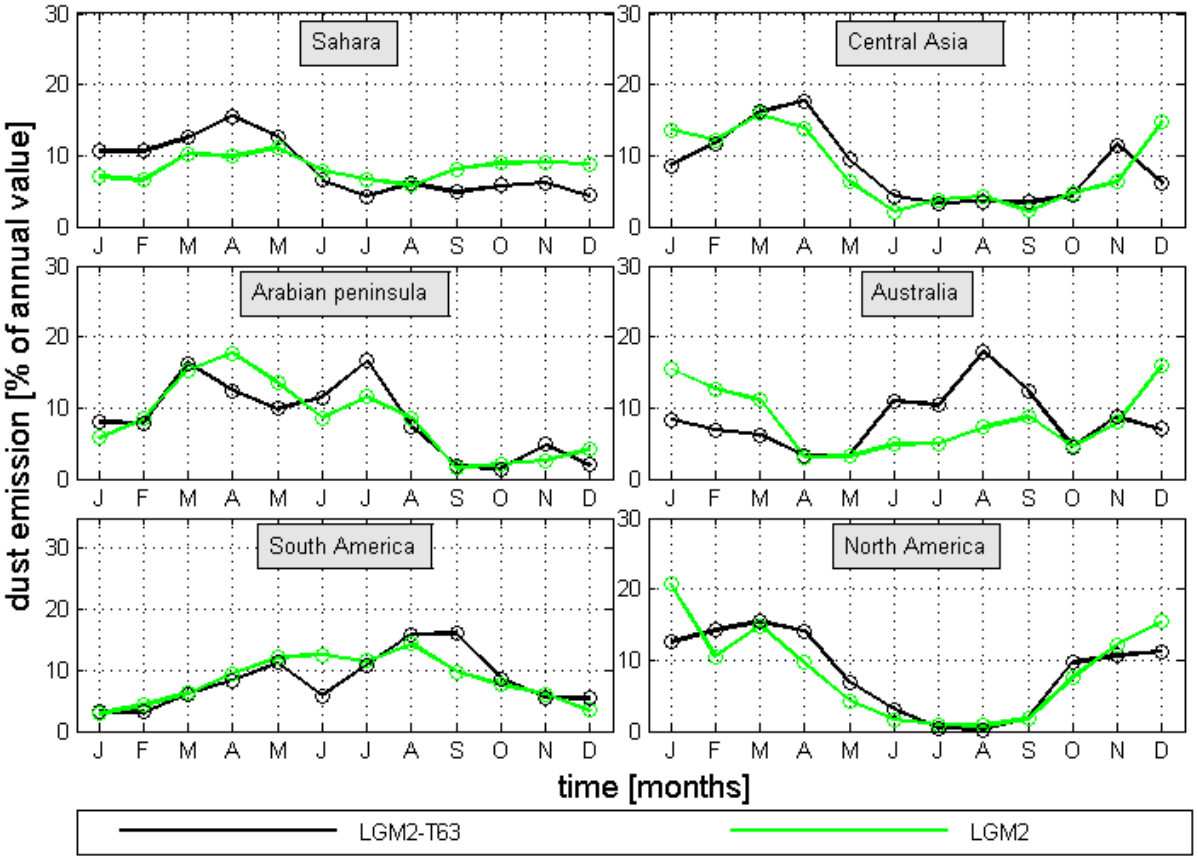

Figure 21: Monthly dust emission for the last glacial maximum simulations. Given are the values for the specified source regions Sahara, central Asia, Arabian peninsula, Australia, South America and North America. The monthly emission is given in percentage of the total annual dust emission value.

To better compare the influence of the model resolution onto the seasonal character of the dust emissions in the specified source regions, Figure 21 depicts the relative monthly contributions to the annual dust emission. The timing of maximum emissions agree for the Sahara, central Asia, the Arabian peninsula and North America. The maximum on the northern hemisphere is during boreal winter (DJF) and spring (MAM), with the shift by one season for the Arabian peninsula (MAM, JJA), that was already mentioned in Chapter 4.6.2. For South America, the maximum emission can be seen for the months August

and September, meaning that it is shifted into austral spring by about two months. For Australia, the maximum emission period is shifted from austral summer (November, DJF, March) to boreal summer (JJA, September). For the Sahara, the seasonal character of the emissions is more pronounced for the LGM2-T63 simulation, as the maximum emission in spring is higher, while the minimum in summer is lower.

In general, the same observations for the seasonality of the simulation with the T63L31 model resolution can be stated as for the simulation with the T31L19 model resolution. One exception is a less intense glacial increase for emissions from South America by a factor 18 (compared to a factor 20 in LGM2). Additionally, the maximum emissions for LGM2-T63 take place during austral winter, while it takes places from austral summer and autumn for the LGM2 simulation.

4.9 Seasonal variability of dust depositions (T63L31)

4.9.1 Present-day simulation

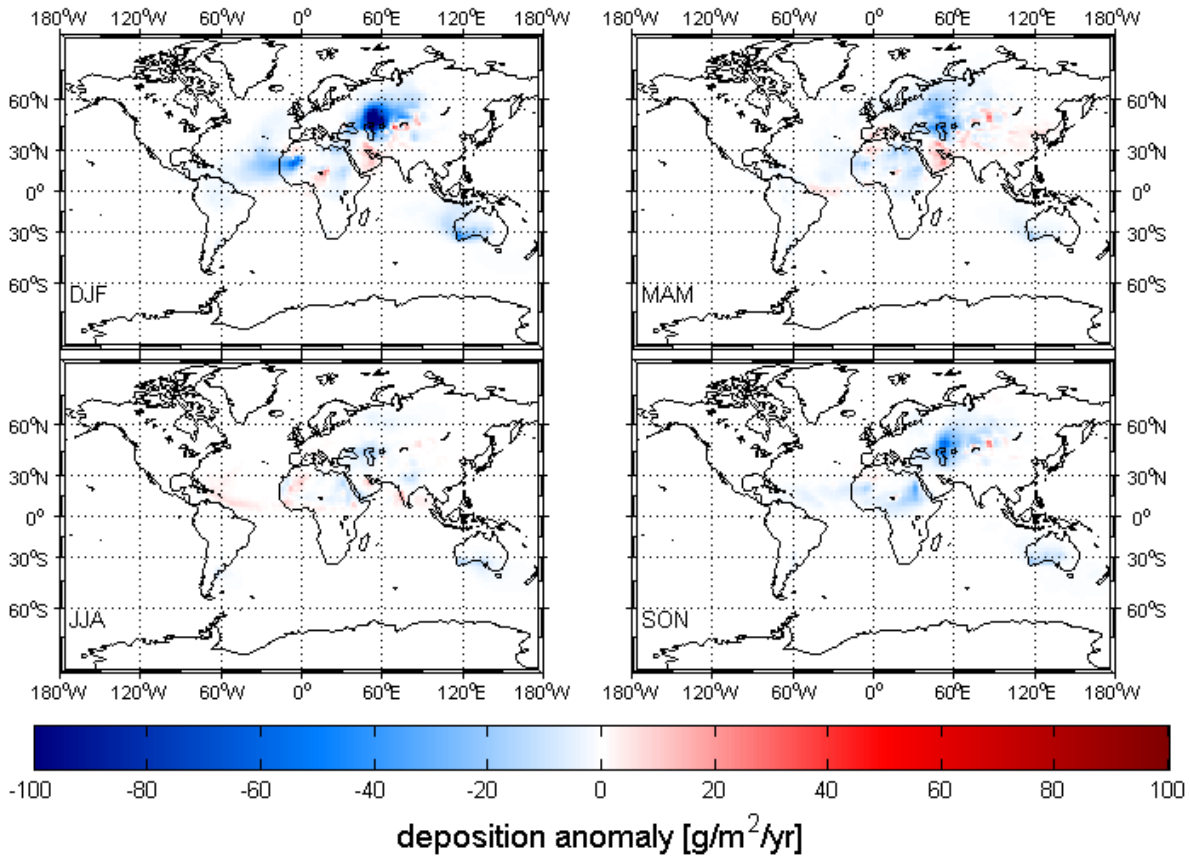

Figure 22: Anomaly for the seasonal mean dust deposition fluxes of the two present-day depositions (PD2-T63 minus PD2). Blue shading indicates a decrease of the PD2-T63 data, taking PD2 as a reference. Red shading indicates an increase. Seasons are conventionally defined as in Figure 5.

The PD2-T63 dust deposition (Appendix, Figure 38) is shown as the anomaly compared to the corresponding T31L19 simulation in Figure 22. In general, it can be seen that the seasonal cycle of the deposition anomaly matches the cycle of the corresponding emission anomaly (Figure 22). The deviations are minimal during boreal summer, the period of minimum emissions on the northern hemisphere. The most significant decrease of depositions can be stated for the region around the Aral sea in central Asia and during DJF. In the western Sahara, a decrease of the dust depositions are apparent, that appear to stem from a local emission area. For Australia, the dust depositions are generally lower, affecting especially the Indian Ocean during DJF. For North and South America, only changes due to the changes of dust transports from the Sahara can be distinguished as the emissions and thus depositions from these regions are rather low.

4.9.2 Last glacial maximum simulation

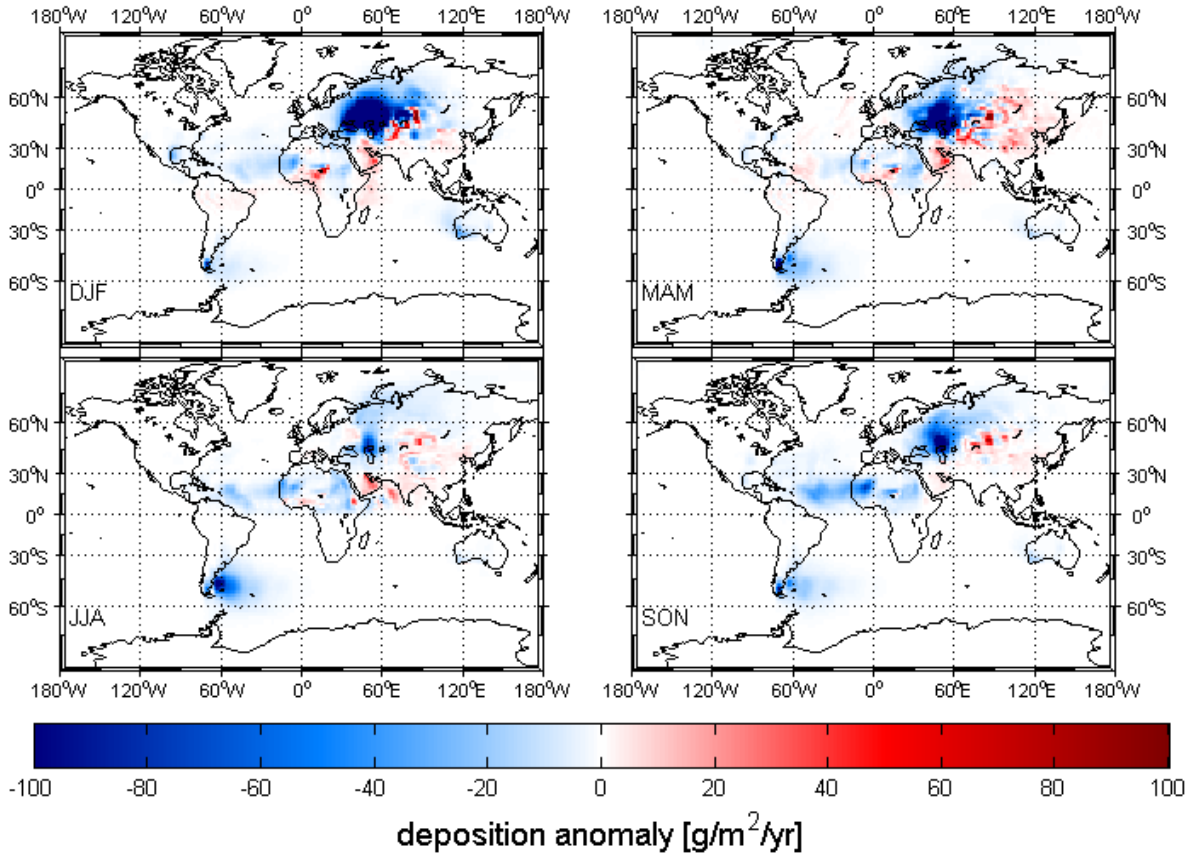

Figure 23: Anomaly for the seasonal mean dust deposition fluxes of the two last glacial maximum simulations (LGM2-T63 minus LGM2). Blue shading indicates a decrease of the LGM2-T63 simulation, taking LGM2 as a reference. Red shading indicates an increase. Seasons are conventionally defined as in Figure 5.

The LGM2-T63 dust deposition (Appendix, Figure 40) is displayed as the anomaly to its corresponding T31L19 simulation in Figure 23. Beside a decrease of dust deposition

fluxes in the source regions itself for central Asia, the Sahara and Australia, the highest decreases can be found over the Atlantic Ocean, adjacent to the Sahara and in the Indian Ocean, close to Australia. The decrease over the Atlantic is especially high during boreal winter (DJF), the maximum emission period and origins from one local area in the western Sahara. For the Arabian peninsula, the dust depositions increased, which matches the findings from the corresponding emission anomaly (Figure 20) and from Table 9.

In contrast to the LGM1 simulation, the LGM2 and LGM2-T63 simulations reveal significant dust deposition fluxes to Antarctica. This outcome is matching observations from Antarctic ice cores, indicating that the dust deposition flux has been up to ∼20 times higher as for the present-day [Kohfeld and Harrison, 2001, and references therein]. Li et al. [2010], Tegen [2002] and Werner et al. [2002] also indicate the simulated glacial depositions to be up to 20 times higher, which matches the results of this study with an increase by a factor 10 to 20. For the simulations featuring the modeled vegetation distribution, the higher deposition fluxes can be associated to the increase of dust emissions in South America as the emissions from Australia even decrease for the last glacial maximum simulations.

5 Evaluation

5.1 Description of the DIRTMAP3 data

To evaluate the simulated deposition data, it is compared with observational data from different dust deposition records. Here, the third version of the Dust Indicator and Records of Terrestrial and Marine Paleoenvironments (DIRTMAP3 data compilation) is used [Maher and Kohfeld, 2009]. As only few coring sites are located in the mid-latitudes of the southern hemisphere and thus close to Antarctica, additional coring sites are implemented in this study. These marine sediment cores were taken during the Polarstern cruise ANT-XXVI / 2 and are described by Lamy et al. [2014] .

DIRTMAP3 as described by Maher and Kohfeld [2009] provides 891 datasets among which are records from ice cores, marine sediment cores, marine sediment traps and loess deposits. The data is given in units of mass accumulation rates (MAR) which allows the direct comparison to the simulated dust deposition fluxes as they have the same units of $[g/m^2/yr]$.

5.2 Evaluation by DIRTMAP3 data

From the 891 datasets, 175 are used for the evaluation of the present-day simulations and 88 for the last glacial maximum simulations. Other data from loess deposits are omitted because they are affected by local emission and deposition processes. These terrestrial datasets cannot be reproduced by the coarse resolution of both T31L19 and T63L31. In contrast, there is no other source for dust being deposited on ice than aeolian origins. Ice is thus a good archive for dust deposition fluxes [Maher and Kohfeld, 2009].The dust mass accumulation rate can then be obtained by multiplying the dust concentration with the estimated ice accumulation rate. Even though this estimation may be a source to errors, Mahowald et al. [1999] considers the outcome to be more reliable than modelling the dust concentrations in the ice cores. This modeled value would be sensitive to the modeled precipitation which would lead to even higher uncertainties.

The lithogenic flux obtained from marine sediment cores is calculated following the definition of Wefer and Fischer [1993]. For some coring sites in the North Pacific, the fluxes were estimated by aluminium concentration measurements, assuming that the aluminium content of terrigeneous material is constantly 8% [Saito et al., 1992].
Figure 24 displays the annual mean dust deposition flux obtained from the LGM2 simulation. Additionally, the 88 coring sites from the DIRTMAP3 data set are depicted and indicate the glacial mass accumulation rate. This figure is presented exemplarily to estimate the general agreement between the simulated and observed dust deposition fluxes

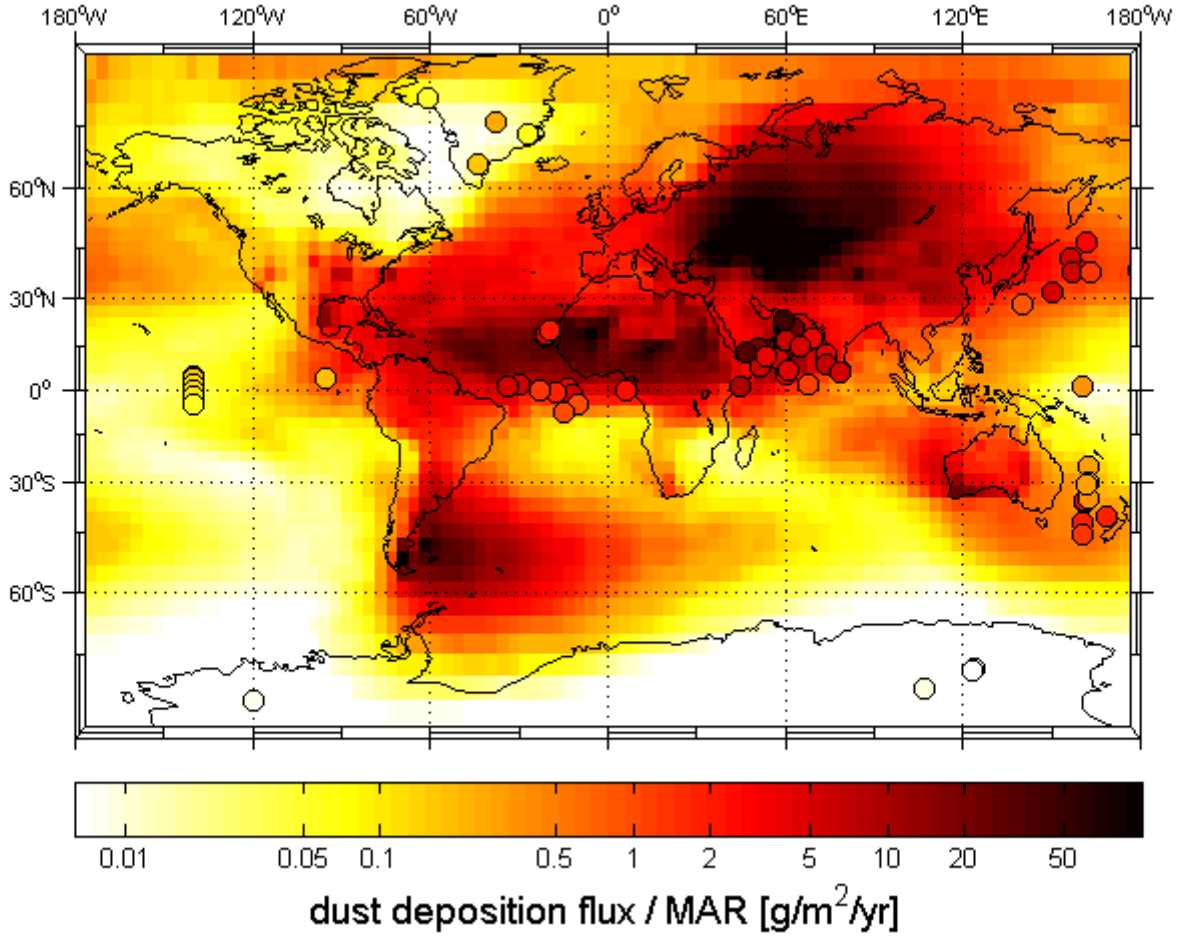

Figure 24: Map showing the annual mean dust deposition fluxes for the LGM2 simulation (background) and the observed mass accumulation rates extracted from the DIRTMAP3 database (markers). Both data types feature the same colour coding.

and to display the spatial distribution of the cores. The figure with the corresponding visualisation for the data from the PD2 simulation can be found in the Appendix (Figure 43)

Most coring sites are located on the northern hemisphere and in equatorial regions. Only few datasets stem from ice cores like in Antarctica or Greenland. For the mid-latitudes, the dust deposition fluxes thus can not be resolved well, except for the Pacific Ocean, close to Australia and Asia. For large parts of the northern and southern hemisphere, the evaluation is consequently less reliable. This is especially true for dust from South America, as no core site is located close to its deposition area. Modeled depositions over the Pacific Ocean are underestimated close to Australia, supporting the hypothesis, that the glacial Australian dust emissions are underestimated. In the eastern Pacific Ocean a single core site implies that dust originating from the Sahara and travelling beyond central America is overestimated. This overestimation can also be observed for two further

datasets in the Atlantic, close to the coast of Africa, while further south more datasets indicate a correct estimation or even underestimation of depositions from the Sahara. Also modeled depositions over Greenland are partly underestimated. The same is true for depositions in the Indian Ocean, close to the Arabian peninsula, for depositions over the Pacific Ocean, that origin from Australia and for at least one Antarctic dataset.

To better visualise the agreement of observational DIRTMAP3 data and the model results, scatterplots, which display the observed mass accumulation rate against the simulated dust deposition flux of the corresponding, closest grid point are analysed.

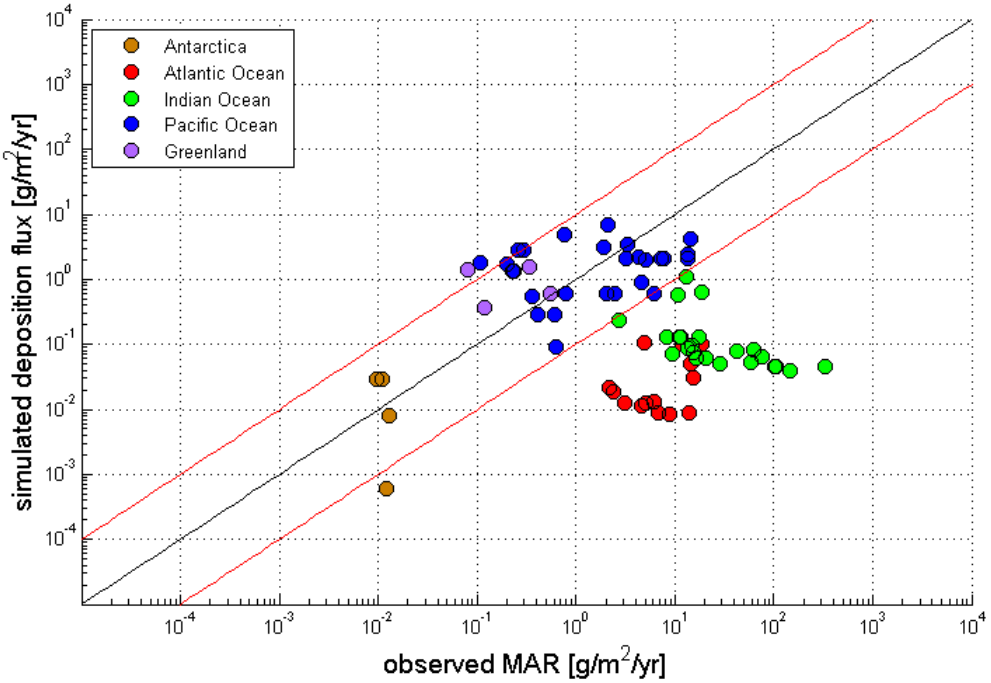

Figure 25: Scatterplot for the simulated dust deposition flux from LGM2 versus the observed mass accumulation rate from the DIRTMAP3 dataset.The different deposition areas (Antarctica, Atlantic Ocean, Indian Ocean, Pacific Ocean, Greenland) are colour coded. The red lines indicate a deviation of the datasets by one magnitude, while the black line indicates perfect agreement.

Figure 25 shows the scatterplot for the LGM2 simulation. It becomes distinct, that for some regions, the simulated data matches the observations quite well, while for other regions, like the Atlantic and Indian Ocean, this is not the case. Here, the modeled dust deposition flux underestimates the mass accumulation rate by more than three magnitudes for the Atlantic Ocean and by more than four magnitudes for the Indian Ocean. On the contrary, the magnitude of depositions over the Pacific Ocean, Antarctica and Greenland are in good agreement with the observational data, even though the deviation for Greenland is also up to one magnitude or slightly more.

Figure 25 also reveals that mainly high observed MAR values are underestimated in the LGM2 simulation. As most dust is deposited close to its source region, the underestimation of depositions may be explained by an underestimation of the emissions. The emissions Australia are decreased in the last glacial maximum simulation. As a direct consequence, the Saharan dust transport and deposition over the tropical Atlantic are decreased, as well as its transport into the Indian Ocean which is also affected by decreased depositions from Australia.

The high consistency of observational and simulated data for Antarctica can be assumed to support the strongly increased emissions and thus depositions originating from South America. For a better estimation, additional coring sites in the southern hemisphere and especially Antarctica and the adjacent waters have been analysed in this study. The results are presented in Chapter 5.2.1.

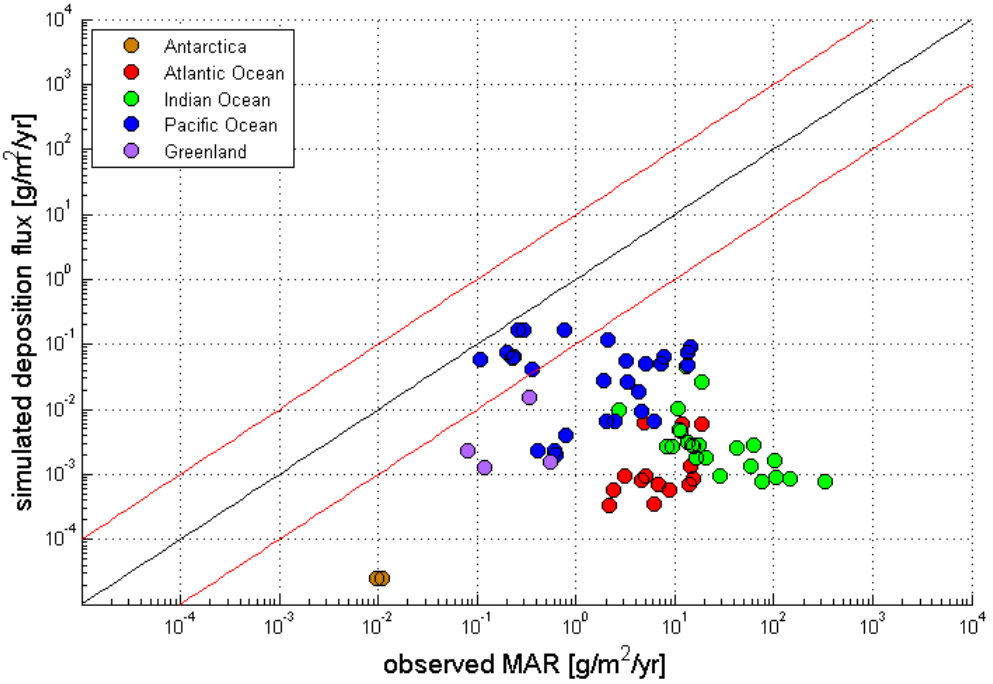

Figure 26: Scatterplot for the simulated dust deposition flux from LGM2-T63 versus the observed mass accumulation rate from the DIRTMAP3 datasets.The different deposition areas (Antarctica, Atlantic Ocean, Indian Ocean, Pacific Ocean, Greenland) are colour coded. The red lines indicate a deviation of the datasets by one magnitude, while the black line indicates perfect agreement.

Figure 26 displays the scatterplot of the LGM2-T63 data versus the observational data from DIRTMAP3. Table 9 displays the large deviations between LGM2 and LGM2-T63 that occur due to the different model resolutions T31L19 and T63L31. Thus, the evaluation against the DIRTMAP3 data might help estimating which results are more realistic.

From Figure 26 it can be inferred, that the simulated depositions in the LGM2-T63 run are generally underestimating the observational data. The largest deviation can be found for data from the Indian Ocean, exceeding a difference of five magnitudes. Only few points, coming from the Pacific Ocean are lying within the one magnitude range. No simulated data point is exceeding the corresponding observation. Comparing the scatterplot to Figure 25, a general similar pattern can be observed, despite the general underestimation by the LGM2-T63 simulation. The highest agreement can still be found for data from the Pacific Ocean, Greenland and Antarctica. The T63L31 results thus appear to be shifted to too low deposition values.

The overall evaluation against the DIRTMAP3 datasets leads to the conclusion, that the T31L19 model resolution produces more reliable results, than the corresponding T63L31 simulation. These observations agree with the observations stated by Carlsen [2014]. Even though the deviations in his study are less drastic, the same tendency can be seen.

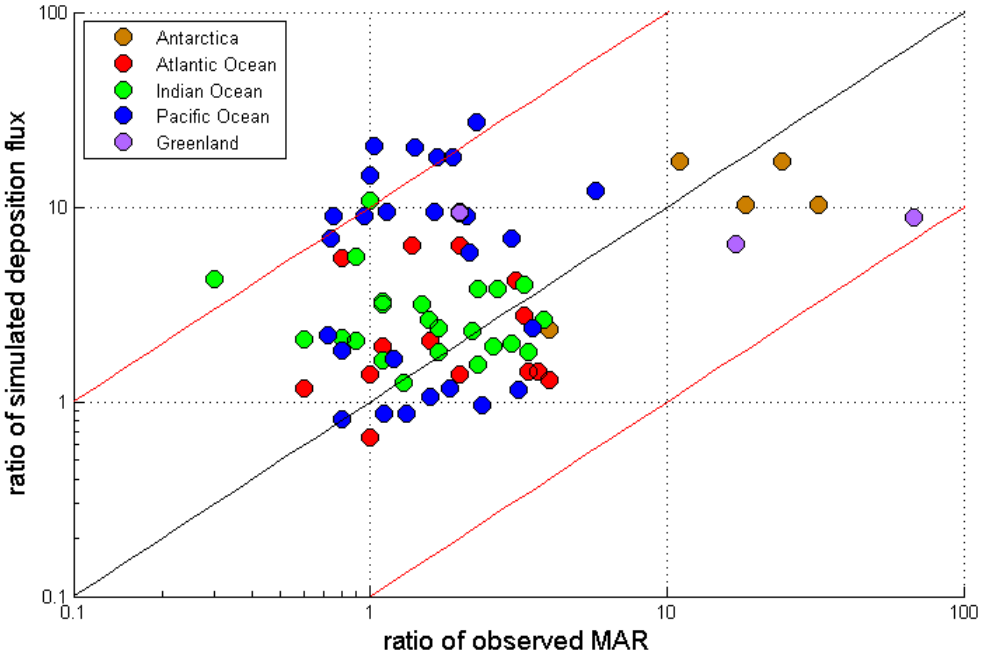

Figure 27: Scatterplot for the last glacial maximum to present-day ratios of the simulated dust deposition flux (LGM2/PD2) versus the observed mass accumulation rate from the DIRTMAP3 datasets.The different deposition areas (Antarctica, Atlantic Ocean, Indian Ocean, Pacific Ocean, Greenland) are colour coded. The red lines indicate a deviation of the ratios by one magnitude, while the black line indicates perfect agreement.

Figure 41 in the Appendix shows the scatterplot of the observed mass accumulation rate versus the simulated dust deposition flux from the PD2 simulation. Here, similar results can be stated as for the corresponding LGM2 simulation. While the data from Pacific, Greenland and Antarctic cores can be well reproduced, the Atlantic and the Indian Ocean

results underestimate the observational data. As this underestimation occurs in both, the PD2 simulation and the LGM2 simulation, it can be assumed to be systematic. To exclude this possible bias, the relative change from present-day to last glacial maximum deposition can be evaluated against the DIRTMAP3 datasets.

Figure 27 displays the scatterplot of the LGM2 / PD2 ratio versus the corresponding DIRTMAP3 dataset ratio. Most values are larger than one, meaning that the last glacial maximum value is larger than the present-day value for the dust deposition. The DIRTMAP3 datasets indicate that the increase for the Pacific Ocean, the Atlantic Ocean and the Indian Ocean are of approximately the same magnitude. This can be resolved for simulation results from the Atlantic and Indian Ocean but only partly for the Pacific Ocean. Here, about half of the LGM2 to PD2 ratios are overestimated by about one magnitude. The largest increases can be found for Antarctica and Greenland which are quite well reproduced by the simulation results or even slightly underestimated. The scatterplot for the LGM1 / PD1 ratio can be found in the Appendix (Figure 42). The comparatively well reproduction of the present-day to glacial increases for the Atlantic and Indian Ocean support the hypothesis, that the underestimation of the simulated deposition values in these regions are a systematic error, that might be attributed to the prescribed modeled vegetation distribution. From Table 7 it can be seen, that this systematic error may lead to a lower glacial increase in the Sahara and a higher glacial decrease in Australia, which would lead to lower depositions in the Atlantic and Indian Ocean.

5.2.1 Evaluation using the Lamy et al. [2014] data

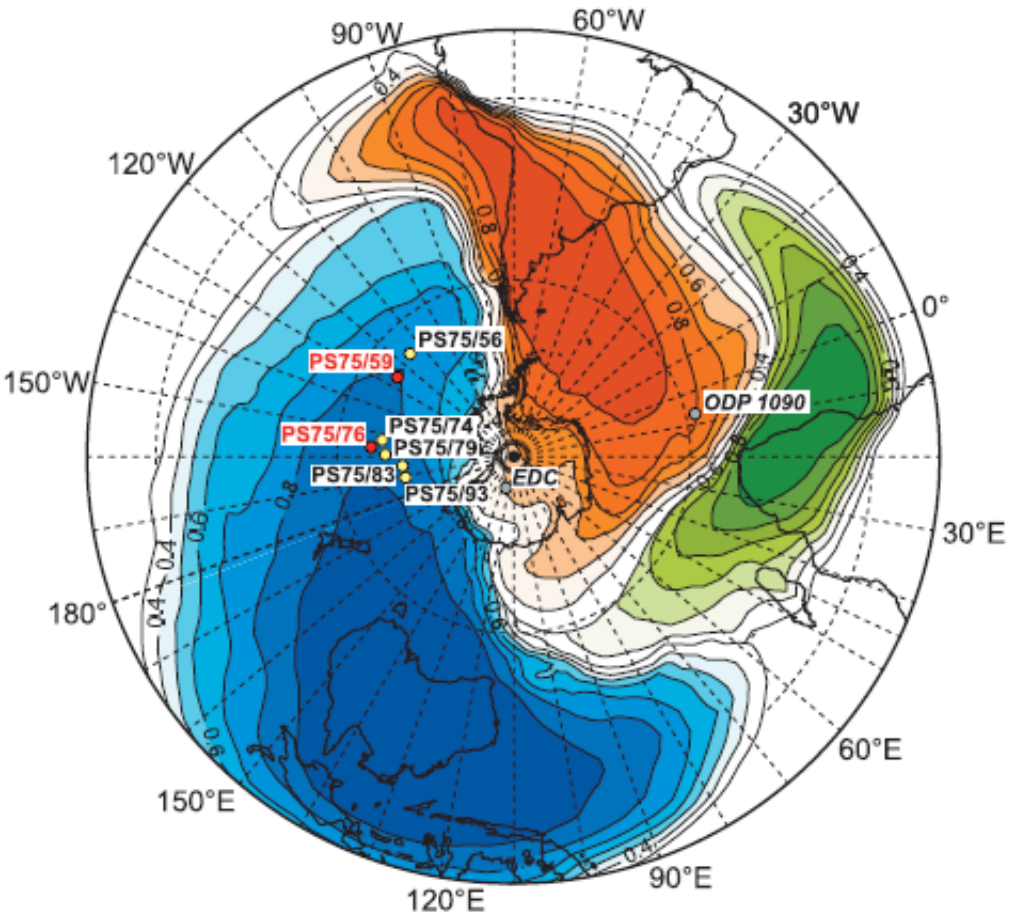

Figure 28: Map of the southern hemisphere with Antarctica in its centre, "showing the modern relative contributions of the three major dust sources in the Southern Hemisphere (blue, Australia; red, South America; green, South Africa)", based on model data. Source: Lamy et al. [2014]

To improve the evaluation in the southern oceans, eight additional marine sediment cores described by Lamy et al. [2014] are added to the DIRTMAP evaluation. The map of Figure 28,shows the location of these eight additional coring sites. They were obtained during the Polarstern cruise ANT-XXVI / 2. Only for two coring sites, the lithogenic mass accumulation was determined. For the others, the iron content was measured. Lamy et al. [2014] assume the changes in iron content to be consistent with the dust content variations from documented Antarctic ice cores and Atlantic sediments. As for most of these additional cores the relative glacial increase to the modern dust deposition fluxes could be stated only, the values are only added to the present-day to last glacial maximum ratio scatterplots (Figure 27).

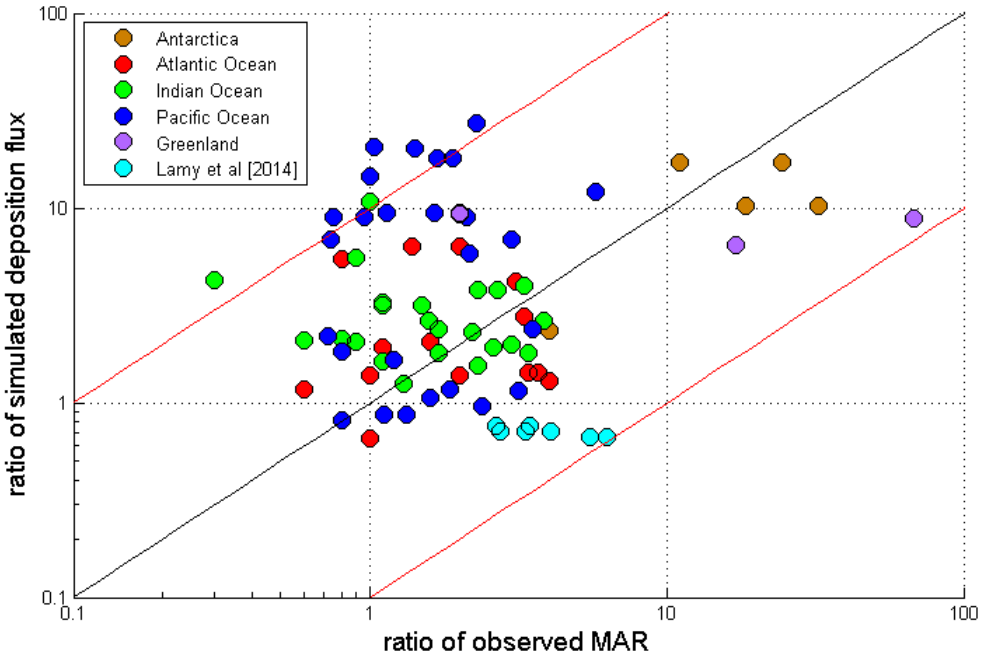

Figure 29: Scatterplot for the last glacial maximum to present-day ratios of the simulated dust deposition flux (LGM2/PD2) versus the observed mass accumulation rate from the DIRTMAP3 datasets and the recent Lamy et al. [2014] data.

The increase of glacial dust depositions obtained from the marine cores introduced by Lamy et al. [2014] is underestimated by the simulations (Figure 29). This underestimation is even more pronounced than for the other cores from high latitudes (Greenland, Antarctica). This result supports particularly the hypothesis, that the dust depositions on the southern hemisphere are still underestimated by the simulations featuring the modeled vegetation distribution. Taking additionally into account, that according to Lamy et al. [2014], the additional cores are located in an area, where dust depositions stem basically from Australia, the underestimation in the southern hemisphere can be especially attributed to Australia.

For the T63L31 simulations, in Figure 30 the glacial to present ratio (LGM2-T63 to PD2-T63) is displayed. The plot reveals that most ratios exceed the ratio of the corresponding DIRTMAP3 data ratios. The overestimation is slightly higher than for the LGM2/PD2 ratio, although the increase for Antarctica and the additional cores from ANT-XXVI / 2 is still underestimated. Thus, the increased ratios for the T63L31 simulations are of similar quality as for the T31L19 simulations.

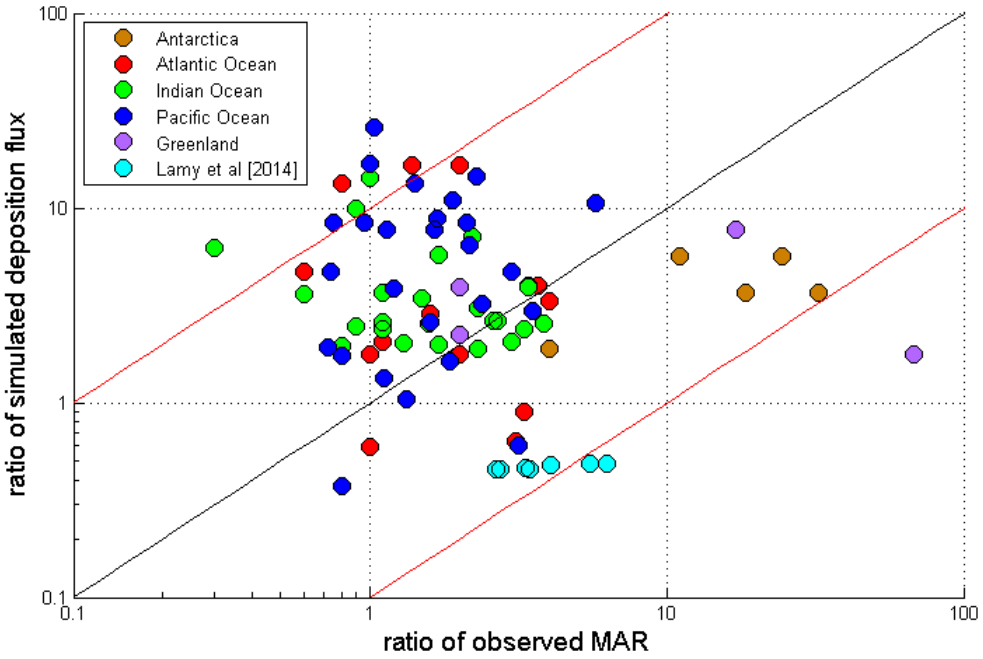

Figure 30: Scatterplot for the last glacial maximum to present-day ratios of the simulated dust deposition flux (LGM2-T63/PD2-T63) versus the observed mass accumulation rate from the DIRTMAP3 datasets and the recent Lamy et al. [2014] data.

6 Conclusion and Outlook

6.1 Conclusion

The aim of this master thesis was to investigate the influence of different climate conditions and different vegetation distributions onto the dust cycle, simulated with the ECHAM5-HAM2 general circulation model. The dust cycle during the last glacial maximum has been generally stronger than for the present-day, which is consistent with observations from marine sediment and ice-cores [Kohfeld and Harrison, 2001]. The change of the boundary conditions, like the orbital parameters, lead to a colder and thus drier climate, which also affected the coverage by vegetation and consequently the bare soil fraction, which is a requirement for the emission of dust into atmosphere. For many studies, an observational vegetation distribution inferred from present-day satellite measurements has been prescribed for both present-day and last glacial maximum simulations. This neglects the influence of the changed climate conditions onto the vegetation distribution. Thus, for this master thesis, simulations have been examined, using a prescribed vegetation distribution derived from a fully coupled run of the COSMOS Earth System Model.

For the T31L19 model resolution, both present-day simulations, using either an observational or a modeled vegetation distribution, lead to global emission and deposition values that are equal within a range of 10%. But in general the global values are on the lower border of results from other studies [Mahowald et al., 2006a, Werner et al., 2002]. Comparing the global outcome of the present-day versus the last glacial maximum simulations for the different vegetation distributions reveals a twofold present-day to glacial increase due to the change of climate boundary conditions. A threefold increase of the same magnitude can be observed for the simulations comprising the modeled distribution. Thus, the change of the vegetation distribution leads to an absolute change of dust emissions, that is of approximately the same size as the change of climate conditions.

While the transport patterns for all simulations are similar and the seasonal emission changes are in phase with the vegetation changes, the glacial increase is not globally uniform but varies for the specified source regions Sahara, central Asia, Arabian peninsula, Australia, North and South America. Central Asia displaces the Sahara as the strongest dust emission area during the LGM. Australia is the only region, where the glacial emissions decrease compared to present-day. For the simulations with the modeled vegetation distribution, the glacial increase of dust from South America increases by a factor 18 to 20.

For the modeled vegetation distribution, simulations with two different model resolutions have been carried out. The global dust emission values for the T63L31 resolution are over 50% smaller than the values of the corresponding T31L19 simulations. Apart

from this large deviation, the relative changes from present-day to last glacial maximum are similar for the simulations comprising the modeled vegetation distribution.

The evaluation of the simulated data against the observational DIRTMAP3 dataset [Maher and Kohfeld, 2009] reveals that the T63L31 simulations underestimate the observations from marine sediment cores and ice cores. In contrast, a qualitative better agreement for the T31L19 dust depositions can be found. Especially over Greenland, Antarctica and the Pacific Ocean, simulation and observation agree fairly well. Dust emissions into the Indian Ocean and the Atlantic Ocean are up to three magnitudes underestimated, which can be attributed to an underestimation of dust emissions from the Sahara and Australia. The glacial dust depositions over Antarctica are ∼10 to 20 times higher than during present-day, which partly agrees with the observations of ∼20 times higher depositions [Kohfeld and Harrison, 2001, and references therein]. Additional cores from ANT-XXVI / 2 again suggest that glacial dust emissions from Australia are underestimated, here.

6.2 Outlook

As the time for this master thesis has been limited from the beginning, some aspects necessarily remain inconclusive. It is subject to further studies to investigate the unclear issues because a most realistic simulation of the dust model is valuable for a correct estimation of the dust cycle and its impact on the climate for past, present and future times.

First of all, the present-day emission values for both the modeled and the observational vegetation distribution could be further investigated. The annual global mean emission rates are lower than expected, when compared to other studies like Werner et al. [2002] or Mahowald et al. [2006]. Another improvable aspect is the underestimation of the dust emissions in the T63L31 simulations. Gläser et al. [2012] state, that lower dust emissions by finer resolutions could be due to an interaction of orography and resolution. Further investigations of this issue include simulations with nudged wind fields. In addition, Carlsen [2014] already showed that the analysis of regional wind velocities might lead to further insights into this model deficit.

To improve the modeled vegetation distribution of the last glacial maximum, glacial vegetation reconstructions could be used to adjust the bare soil fraction. Hereby, the gap between simulated and observational data from the DIRTMAP3 database might be further closed. Especially the enhancement of dust emissions from Patagonia (South America) and Australia deserves further analysis in combination with a more detailed model-data comparison, using dust records from Antarctic ice cores.

Wherever two simulations are compared in this master thesis (e.g. difference plots), a statistical test could improve the interpretation of the results as it shows where differences are significant and thus reliable or insignificant. Such a test would be the t-test. If the results turned out to be insignificant, an increase of the simulation period would produce more reliable results.

References

[Albrecht, 1989] Albrecht, B. (1989). Aerosols, Cloud Microphysics, and Fractional Cloudiness. *Science*, 245 (4923):1227 – 1230.

[Arimoto, 2001] Arimoto, R. (2001). Eolian dust and climate: Relationships to sources, tropospheric cchemistry, transport and deposition. *Earth-Science Reviews*, 54 (1 - 3):29 – 42.

[Barnola et al., 1987] Barnola, j.-M., Raynaud, D., Korotkevich, Y., and Lorius, C. (1987). Vostock ice core provides 160,000-year record of atmospheric CO2. *Nature*, 329:408 – 414.

[Barry and Chorley, 2010] Barry, R. and Chorley, R. (2010). *Atmosphere, Weather and Climate (9th edition)*. Routledge London New York.

[Braconnot et al., 2012] Braconnot, P., Harrison, S., Kageyama, M., Bartlein, P., Masson-Delmotte, A., Abe-Ouchi, A., Otto-Bliesner, B., and Zhao, Y. (2012). Evaluation of climate models using paleoclimate data. *Nature Climate Change*, 2:417 – 424.

[Braswell et al., 1997] Braswell, B., Schimel, D., Linder, E., and Moore, B. (1997). The response of global terrestrial ecosystems to interannual temperature variability. *Science*, 278:870 – 872.

[Carlsen, 2014] Carlsen, T. (2014). Simulation von heutigem und glazialem mineramineral Staubtransport im Klimamodell ECHAM5-HAM2. *Bachelorarbeit*.

[Dentener et al., 1996] Dentener, F., Carmichael, G., Zhang, Y., Lelieveld, J., and Crutzen, P. (1996). Role of mineral aerosol as a reactive surface in the global troposphere. *Journal of Geophysical Research*, 101(D17):22869 – 22889.

[Donner et al., 2011] Donner, L., Schubert, W., and Somerville, R. (2011). *The Development of Atmospheric General Circulation Models: Complexity, Synthesis, and Computation*. Cambridge University Press, New York.

[Duce, 1995] Duce, R. (1995). *Sources, didistributions, and fluxes of mineral aerosols and their relationship to climate. In: Charlson, R., Heintzenberg, J. (Eds.), Aerosol Forcing of Climate*. Wiley, New York, pages 43 - 72.

[Gläser et al., 2012] Gläser, G., Kerkweg, A., and Wernli, H. (2012). The climate Dust Cycle in EMAC 2.40: sensitivity to the spectral resolution and the dust emission scheme. *Atmospheric Chemistry and Physics*, 12:1611 – 1627.

[Haese et al., 2013] Haese, B., Werner, M., and Lohmann, G. (2013). Stable water isotopes in the coupled atmosphere-land surface model ECHAM5-JSBACH. *Geoscientific Model Development*, 6:1–18.

[Harrison et al., 2001] Harrison, S., Kohfeld, K., Roelandt, C., and Claquin, T. (2001). The role of dust in climate changes today, at the last glacial maximum and in the future. *Earth-Science Reviews*, 54:43–80.

[Joussaume et al., 1999] Joussaume, S., Taylor, K., Braconnot, P., Mitchell, J., Kutzbach, J., and et al., S. H. (1999). Monsson changes for 6000 years ago: Results of 18 simulations from the Paleoclimate Modelling Intercomparison Project (PMIP). *Geophysical Research Letters*, 26 (7):859 – 862.

[Knippertz, 2013] Knippertz, P. (2013). Dust may cool polar regions. *Nature Climate Change*, 3:443 – 444.

[Knorr and Heimann, 1995] Knorr, W. and Heimann, M. (1995). Impact of drought stress and other factors on seasonal land biosphere co2 exchange, studied through an atmospheric tracer transport model. *Tellus*, Ser. B., 47:471 – 489.

[Kohfeld and Harrison, 2001] Kohfeld, K. and Harrison, S. (2001). DIRTMAP: the geological rrecord of dust. *Erarth Science Review*, 54:81 – 114.

[Kohfeld and Tegen, 2007] Kohfeld, K. and Tegen, I. (2007). Record of mineral aerosol and their role in the earth system. *Treatise Geochem.*, 4:1–26.

[Li et al., 2010] Li, F., Ramaswamy, V., Gonoux, P., Broccoli, A., Delworth, T., and Zeng, F. (2010). Toward understaunder the dust deposition in Antarctica during the last glacial maximum: Sensitivity studies on plausible causes. *Journal of Geophysical Research*, 115.

[Lohmann and Roeckner, 1996] Lohmann, U. and Roeckner, E. (1996). Design and performance of a new microphysics scheme develloped for the ECHAM4 general circulation model. *Climate Dynamics*, 12:557 – 572.

[Maher and Kohfeld, 2009] Maher, B. and Kohfeld, K. (2009). DIRTMAP Version 3. LGM and Late Holocene Eolian Fluxes from Ice Cores, Marine Sediment Traps, Marine Sediments and Loess deposits. *http://www.lec.lancs.ac.uk/dirtmap3*.

[Mahowald et al., 2013] Mahowald, N., Albani, S., Kok, J., Engelstaeder, S., Scanze, R., Ward, S., and Flanner, M. (2013). The size distribution of desert dust aerosols and its Impact on the Earth system. *Aeolian Research*, 10:1–19.

[Mahowald et al., 1999] Mahowald, N., Kohfeld, K., Hanson, M., Balkanski, Y., Harrison, S., Prentice, I., Schulz, M., and Rodhe, H. (1999). Dust sources and deposition during teh last glacial maximum and current Climate: A comparison of model results with paleodata from ice cores and marine sediments. *Journal of Geophysical Research*, 104 (D13):15895 – 15916.

[Mahowald et al., 2006a] Mahowald, N., Muhs, D., Levis, S., Rasch, P., Yoshioka, M., Zender, C., and Luo, C. (2006a). Change in atmospheric mineral aerosols in response to climate: Last glacial period, preindustrial, modern, and doubled carbon dioxide climates. *Journal of Geophysical Research*, 111:D10202.

[Mahowald et al., 2006b] Mahowald, N., Yoshioka, M., Collins, W., Conley, A., Fillmore, D., and Coleman, D. (2006b). Climate response and radiative forcing from mineral arosols during the last glacial maximum, preindustrial, current and doubled-carbon dioxide climates. *Geophysical Research Letters*, 33:L20705.

[Marticorena and Bergametti, 1995] Marticorena, B. and Bergametti, G. (1995). Modelling the atmospheric dust cycle: 1. Design of a soil-derived dust emission scheme. *Journal of Geophysical Research*, 100 (D8):16, 415 – 16, 430.

[Miller and Tegen, 1998] Miller, R. and Tegen, I. (1998). Climate response to soil dust aerosols. *American Meteorological Society*, 11:3247 – 3267.

[Mulitza et al., 2011] Mulitza, S., Heslop, D., Pittauerova, D., Fischer, H., Meyer, I., Stuut, J., Zabel, M., Mollenhauer, G., Collins, J., Kuhnert, H., and Schulz, M. (2011). Increase in African dust flux at the onset of commercial agriculture in the Sahel region. *Nature*, 466:226 – 228.

[Perlwitz et al., 2001] Perlwitz, J., Tegen, I., and Miller, R. (2001). Interactive soil dust aerosol model in the GISS GCM: 1. Sensitivity of the soil dust cycle to radiative properties of soil dust aerosols. *Geophysical Research*, 106:18167–18192.

[Petit et al., 1999] Petit, J., Jouzel, J., Raynaud, D., Barkov, N., Barnola, j.-M., Basile, I., Bender, M., Chapellaz, J., Davis, M., Delaygue, G., Delmotte, M., Kotlyakov, V., Legrand, M., Lipenkov, V., Lorius, C., Pépin, L., Ritz, C., Saltzmann, E., and Stievenard, M. (1999). Climate and atmospheric history of the past 420,000 years from the Vostock ice core, Antarctica. *Nature*, 399:429 – 436.

[Raddatz et al., 2007] Raddatz, T., Reick, C., Knorr, W., Kattge, J., Roeckner, E., Schnur, R., Schnitzler, K.-G., Wetzel, P., and Jungclaus, J. (2007). Will the tropical land biosphere dominate the climate-carbon cycle feedback during the twenty-first century? *Climate Dynamics*, 29:565 – 574.

[Rödel and Wagner, 2011] Rödel, W. and Wagner, T. (2011). *Physik unserer Umwelt: Die Atmosphäre (4. Auflage)*. Springer Verlag Berlin Heidelberg.

[Roeckner et al., 2003] Roeckner, E., Bäuml, G., Bonaventura, L., Brokopf, R., Esch, M., Giorgetta, M., Hagemann, S., Kirchner, I., Kornblueh, L., Manzini, E., Rhodin, A., Schlese, U., Schulzweida, U., and Tompkins, A. (2003). *The Atmospheric General Circulation Model ECHAM: Part 1.* Max Planck Institute for Meteorology Hamburg. Report No. 349.

[Saito et al., 1992] Saito, C., Noriki, S., and Tsunogai, S. (1992). Particulate flux of Al, a component of land origin, in the western North Pacific. *Deep-Sea Research*, Part A, 39:1315–1327.

[Sassen et al., 2003] Sassen, K., DeMott, P., Prospero, J., and Poellot, M. (2003). Saharan dust storms and indirect aerosol effect on clouds: CRYSTAL-FACE results. *Geophysical Research Letters*, 30:12.

[Schäfer-Neth and Paul, 2003] Schäfer-Neth, C. and Paul, A. (2003). The Atlantic Ocean at the last glacial maximum: 1. Objective mapping of the GLAMAP sea-surface conditions. *In: Wefer, G., Mulitza, S. and Ratmeyer, V. (eds): The South Atlantic in the Late Quartenary: Material Budget and Current Systems, Springer-Verlag Berlin, Heidelberg.*

[Seinfeld and Pandis, 1998] Seinfeld, J. and Pandis, S. (1998). *Atmospheric Chemistry and Physics: From Air Pollution to Climate Change.* John Wiley and Sons, Inc., Hoboken, New Jersey.

[Shao, 2008] Shao, Y. (2008). *Physics and Modelling of Wind Erosion.* Springer Verlag Berlin Heidelberg.

[Shao et al., 2011] Shao, Y., Chappell, A., Huang, J., Lin, Z., McTainsh, H., Mikami, M., Tanaka, T., Wang, X., and Yoon, S. (2011). Dust cycle: An emerging core theme in Earth system science. *Aeolian Research*, 2:181 – 204.

[Sokolik and Toon, 1996] Sokolik, I. and Toon, O. (1996). Dust radiative forcing by anthropogenic airborne mineral aerosols. *Nature*, 381:681 – 683.

[Stier et al., 2005] Stier, P., Feichter, J., Kinne, S., Kloster, S., Vignati, E., Wilson, J., Ganzeveld, L., Tegen, I., Werner, M., Balkanski, Y., Schulz, M., Bucher, O., Minikin, A., and Petzold, A. (2005). The aerosol-climate model ECHAM5-HAM. *Atmospheric Chemistry and Physics*, 5:1125 – 1156.

[Sudarchikowa, 2012] Sudarchikowa, N. (2012). *Modelling of mineral dust in the Southern Hemisphere with focus on Antarctica for interglacial and glacial climate conditions*. PhD thesis, International Max Planck Research School on Earth System Modelling.

[Tegen, 2002] Tegen, I. (2002). Modelling the mineral dust aerosol cycle in the climate system. *Quaternary Science Reviews*, 22:1821 – 1834.

[Tegen and Fung, 1995] Tegen, I. and Fung, I. (1995). Contribution to the atmospheric mineral aerosol load from land surface modification. *Journal of Geophysical Research*, 100 (D9):18,707 – 18,726.

[Tegen et al., 1996] Tegen, I., Lacis, A., and Fung, I. (1996). The influence on climate forcing of mineral aerosols from disturbed soils. *Nature*, 380:419 – 422.

[Textor, 2006] Textor (2006).

[Twomey, 1974] Twomey, S. (1974). Pollution and the planetary albedo. *Atmospheric Environment*, 8:1251 – 1256.

[Watson et al., 2000] Watson, A., Bakker, D., Ridgwell, A., Boyd, P., and Law, C. (2000). Effect of iron supply on Southern Ocean CO2 uptake and implications for glacial atmospheric CO2. *Nature*, 407:730 – 733.

[Werner et al., 2002] Werner, M., Tegen, I., Harrison, S., Kohfeld, K., Prentice, I., Balkanski, Y., Rodhe, H., and Roelandt, C. (2002). Seasonal and interannual variability of the mineral dust cycle under present and glacial climate conditions. *Journal of Geophysical Research*, 107 (D24):2 (1–19).

[Wilson et al., 2001] Wilson, J., Cuvelier, C., and Raes, F. (2001). A modelling study of global mixed aerosol fields. *Journal of Geophysical Research*, 106:34081 – 34108.

[Zhang et al., 2012] Zhang, K., O'Donnell, D., Kazil, J., Kinne, P. S. S., Lohmann, U., Ferrachat, S., Croft, B., Quaas, J., Wan, H., Rast, S., and Feichter, J. (2012). The global aerosol-climate model ECHAM5-HAM, version 2: sensitivity to improvements in process presentations. *Atmospheric Chemistry and Physics*, 12:8911 – 8949.

List of Figures

List of Tables

Appendix

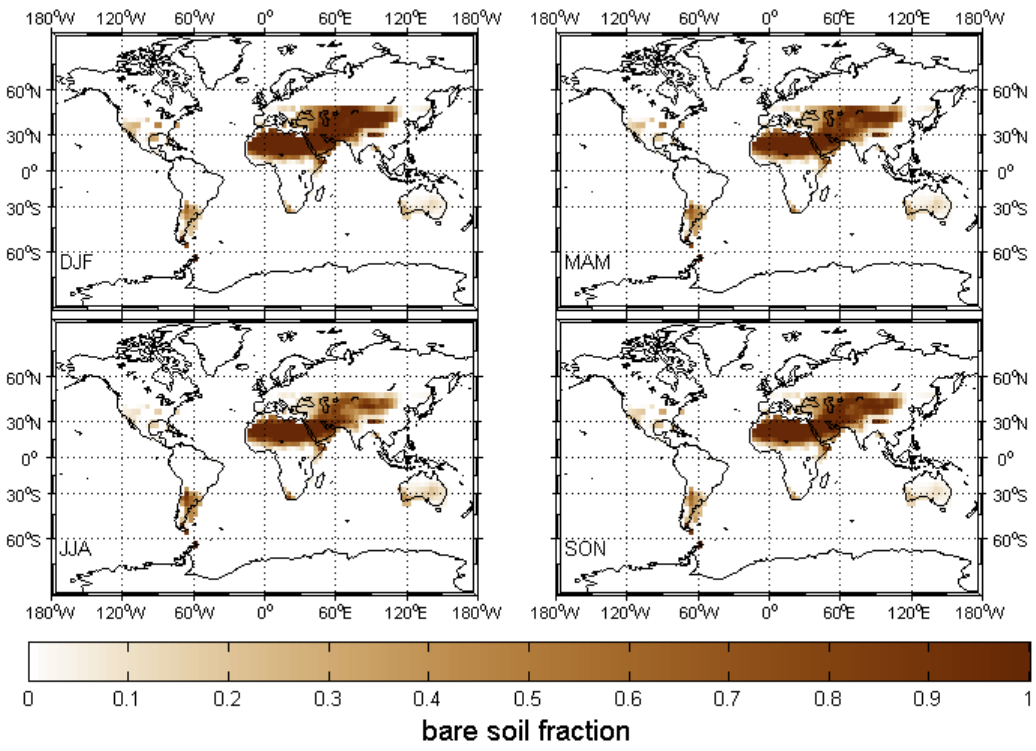

Figure 31: Seasonal mean of the bare soil fraction in the LGM2 simulation. Seasons are conventionally defined as in Figure 5.

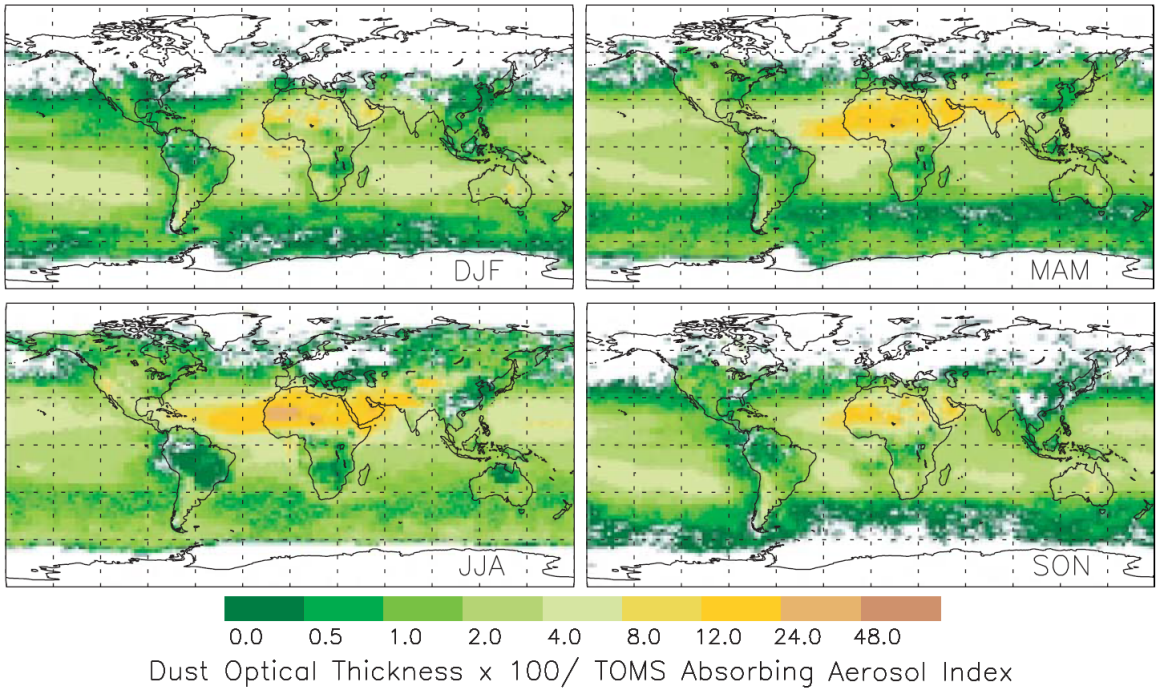

Figure 32: Remotely sensed Aerosol Index from the Total Ozone Mapping Spectrometer (TOMS), averaged for 5 years (1986 - 1990). Adapted from Tegen [2002]

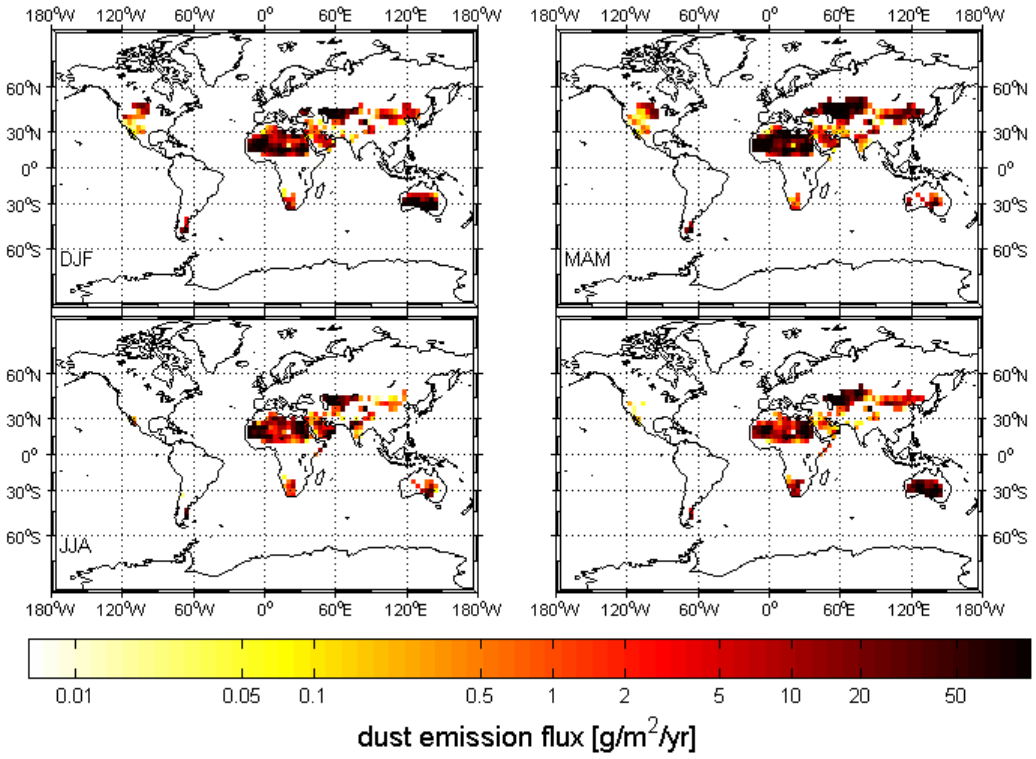

Figure 33: PD1 emissions. Seasons are conventionally defined as in Figure 5.

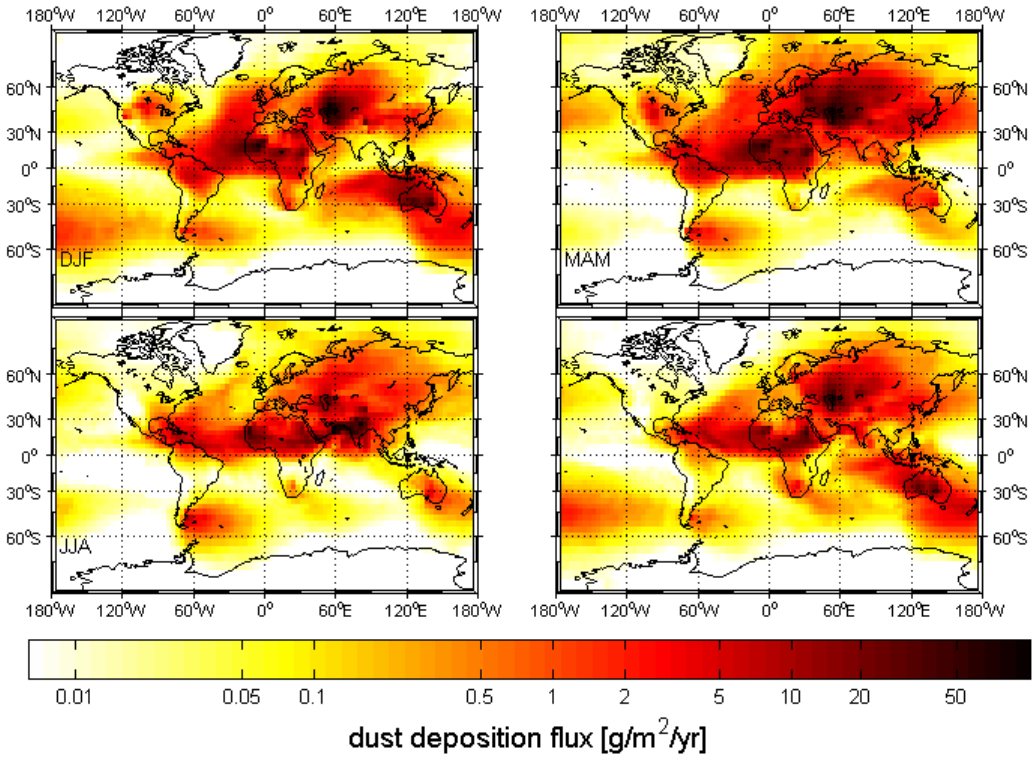

Figure 34: PD1 depositions. Seasons are conventionally defined as in Figure 5.

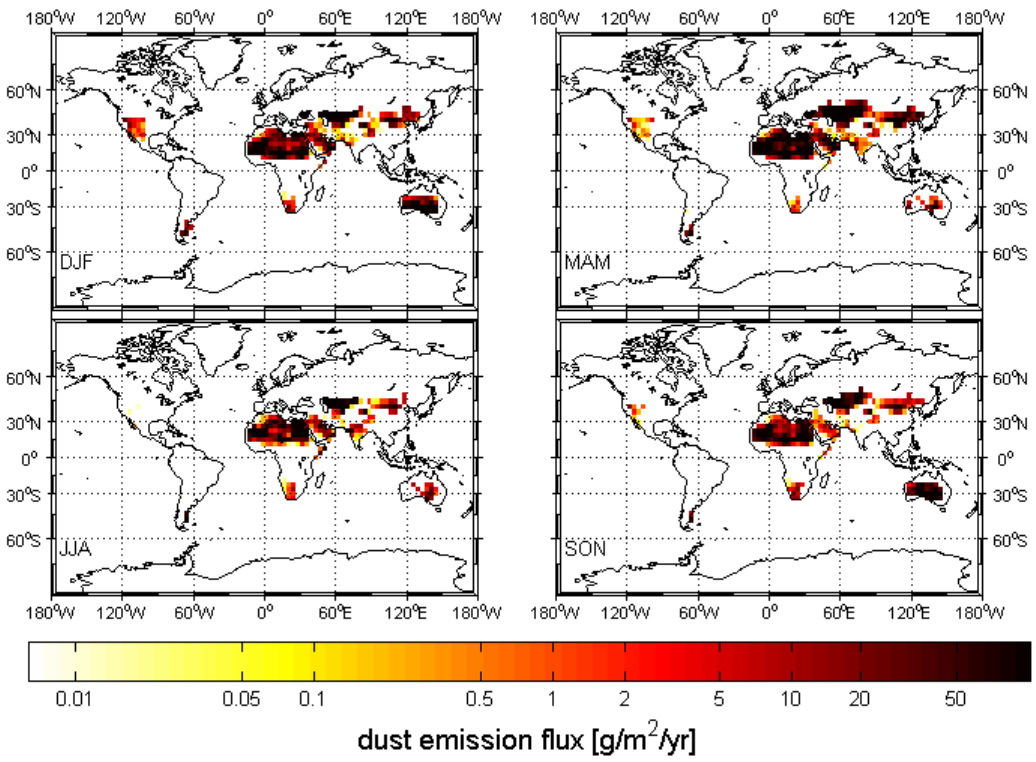

Figure 35: LGM1 emissions. Seasons are conventionally defined as in Figure 5.

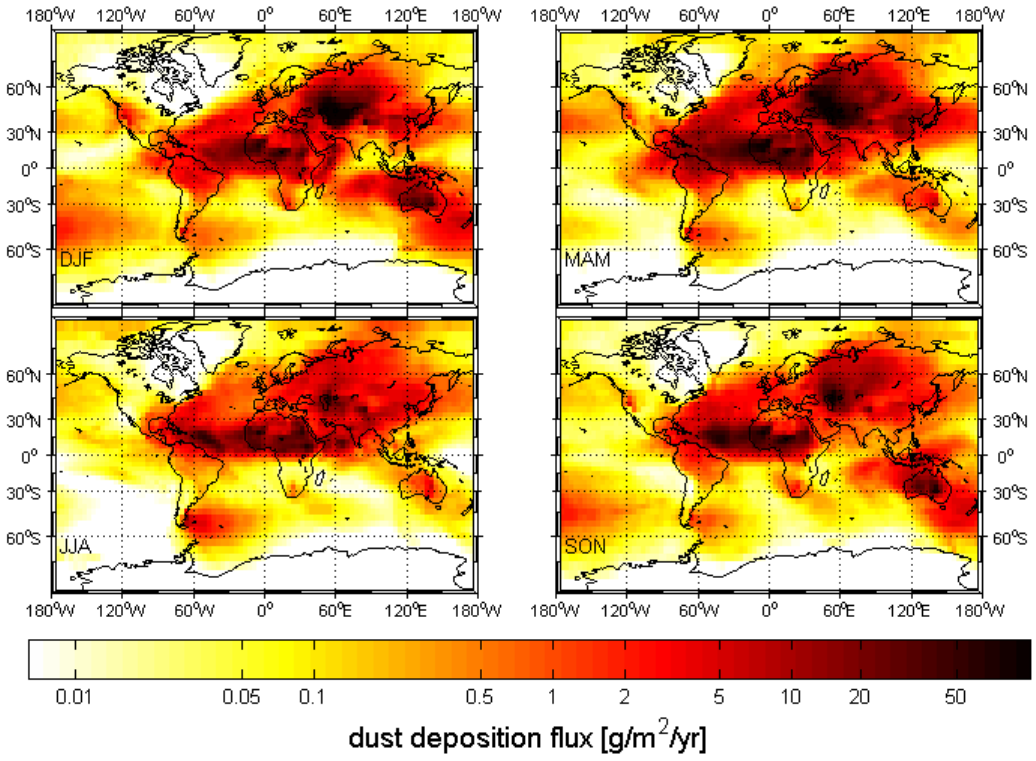

Figure 36: LGM1 depositions. Seasons are conventionally defined as in Figure 5.

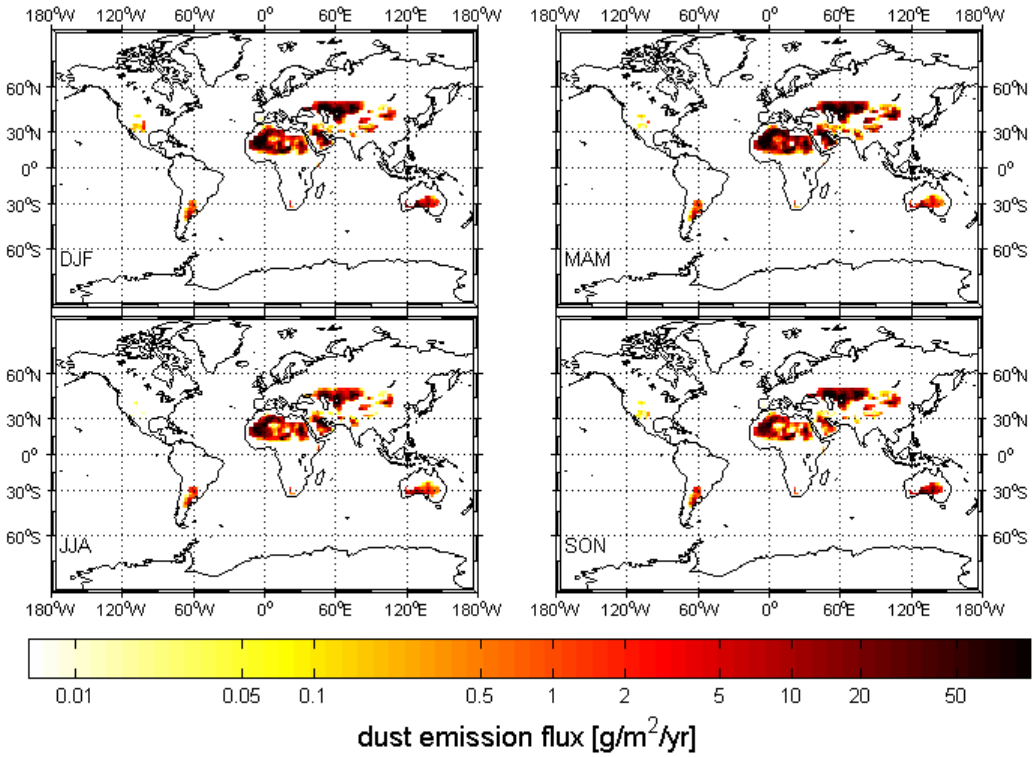

Figure 37: Seasonal mean dust emission fluxes for the PD2-T63 simulation, using the modeled vegetation distribution. Seasons are conventionally defined as in Figure 5.

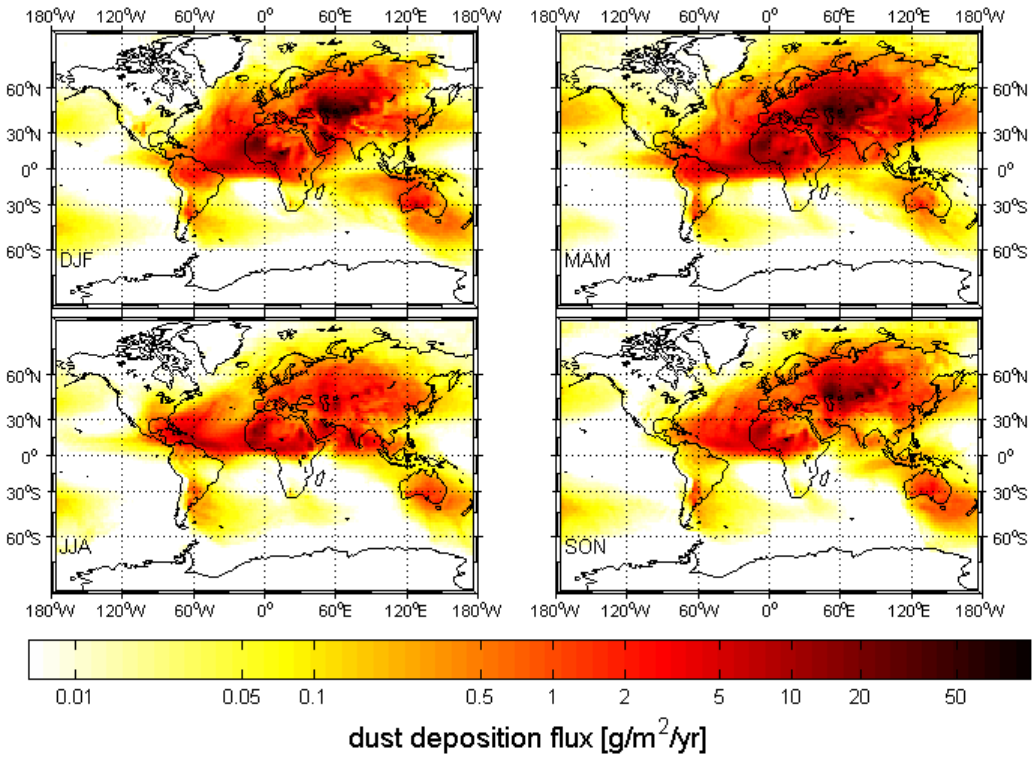

Figure 38: Seasonal mean dust deposition fluxes for the PD2-T63 simulation, using the modeled vegetation distribution. Seasons are conventionally defined as in Figure 5.

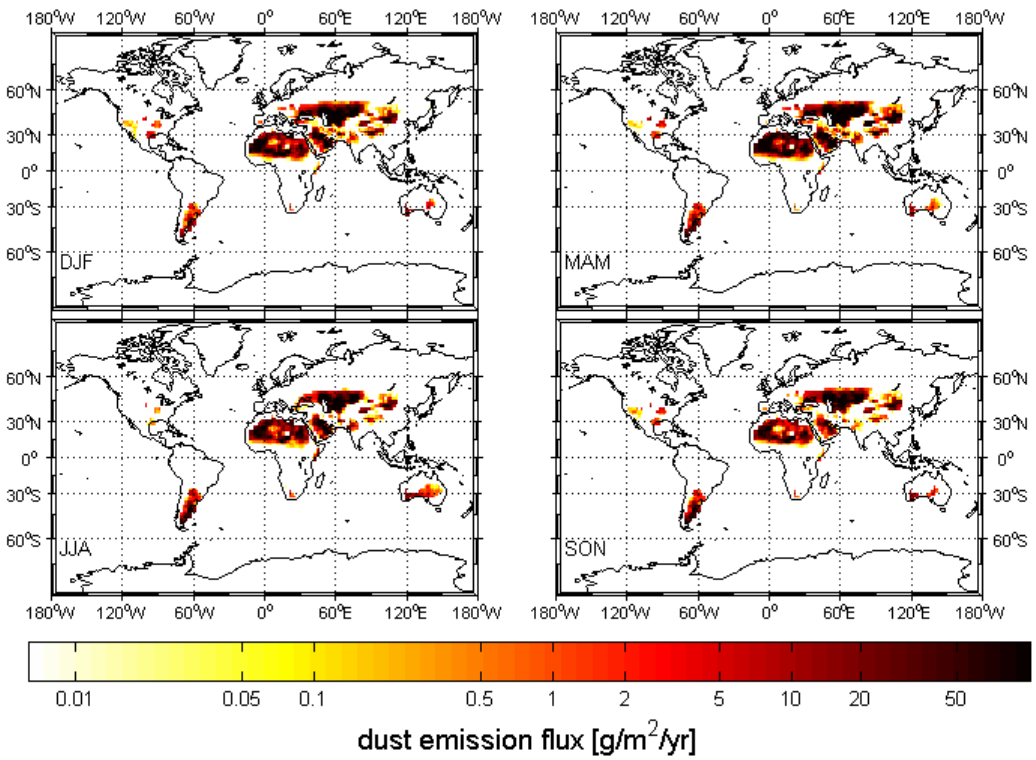

Figure 39: Seasonal mean dust emission fluxes for the LGM2-T63 simulation, using the modeled vegetation distribution. Seasons are conventionally defined as in Figure 5.

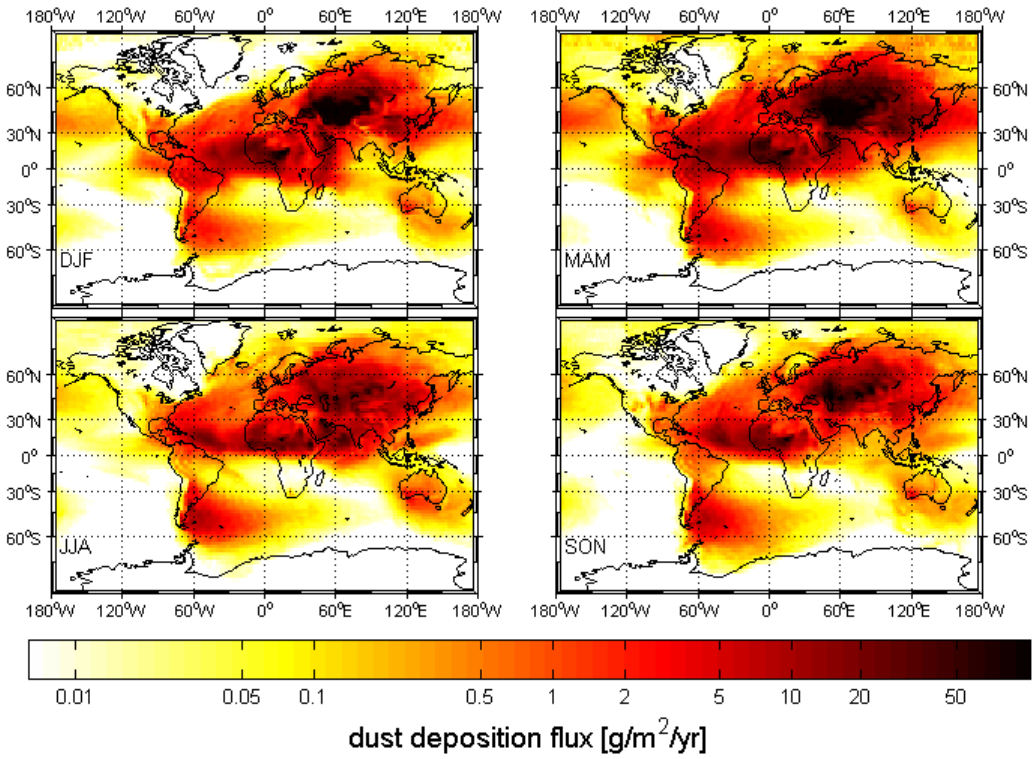

Figure 40: Seasonal mean dust deposition fluxes for the LGM2-T63 simulation, using the modeled vegetation distribution. Seasons are conventionally defined as in Figure 5.

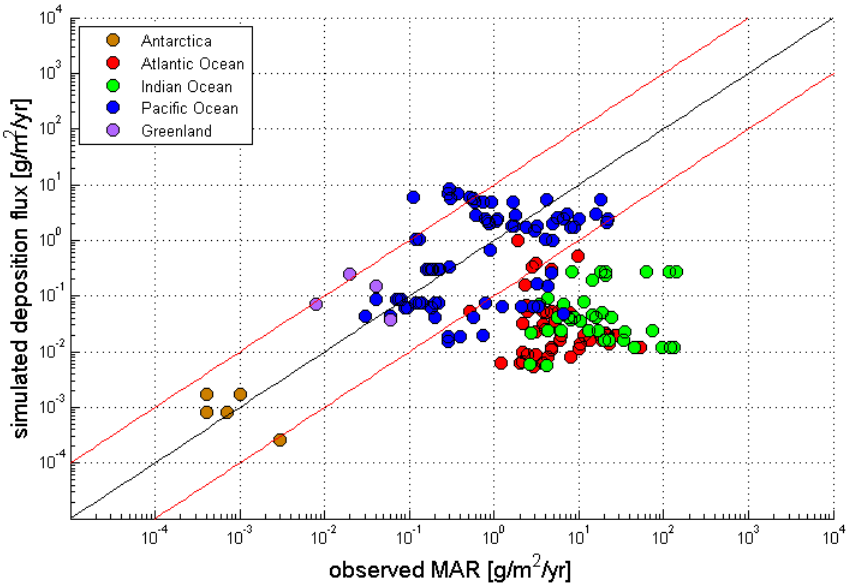

Figure 41: Scatterplot for the simulated dust deposition flux from PD2 versus the observed mass accumulation rate from the DIRTMAP3 datasets.The different deposition areas (Antarctica, Atlantic Ocean, Indian Ocean, Pacific Ocean, Greenland) are colour coded. The red lines indicate a deviation of the datasets by one magnitude, while the black line indicates perfect agreement.

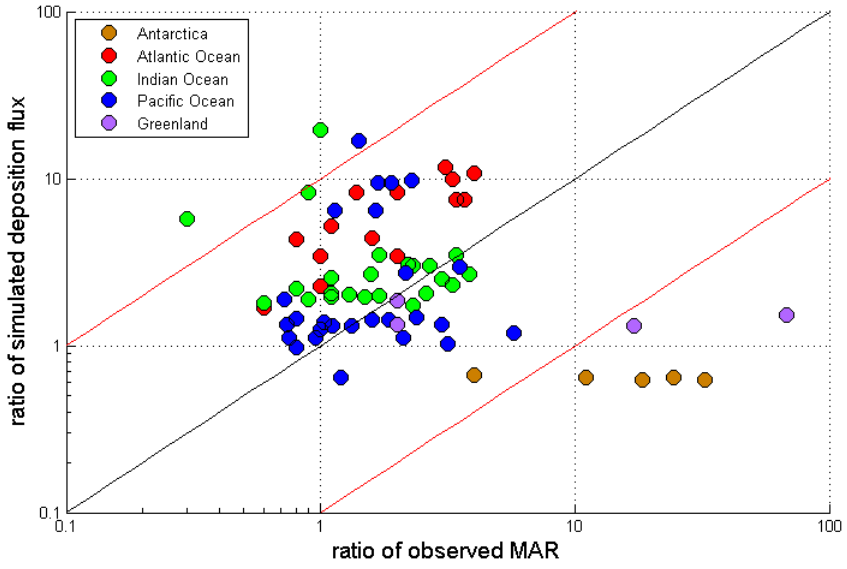

Figure 42: Scatterplot for the last glacial maximum to present-day ratios of the simulated dust deposition flux (LGM1/PD1) versus the observed mass accumulation rate from the DIRTMAP3 datasets.The different deposition areas are colour coded. These are Antarctica, the Atlantic Ocean, the Indian Ocean, the Pacific Ocean and Greenland. The red lines indicate a deviation of the ratios by one magnitude, while the black line indicates perfect agreement.

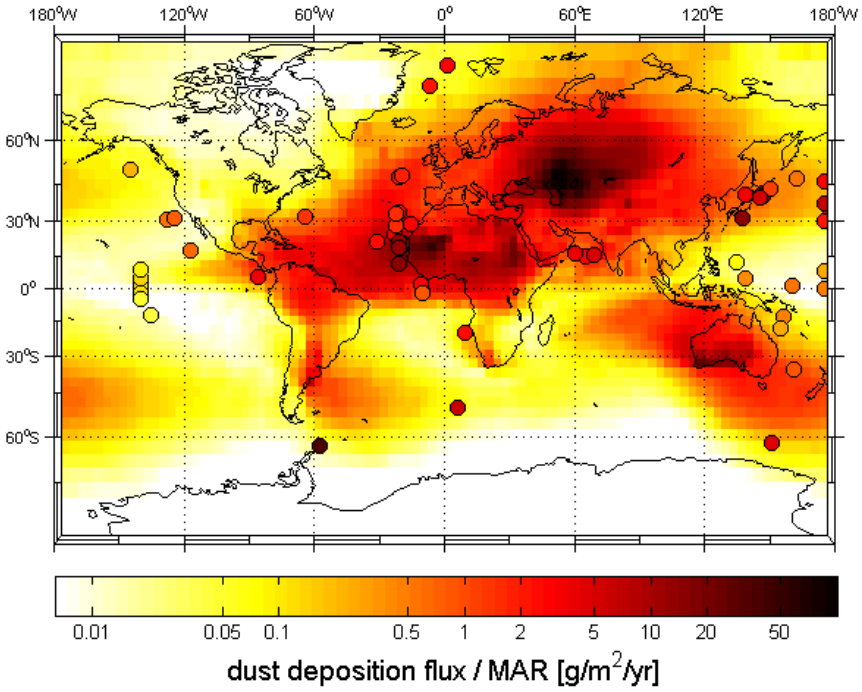

Figure 43: World map showing the annual mean dust deposition fluxes for the PD2 simulation (background) and the observed mass accumulation rates extracted from the DIRTMAP3 database (markers). Both data types feature the same colour coding. Not all coring sites could be displayed.

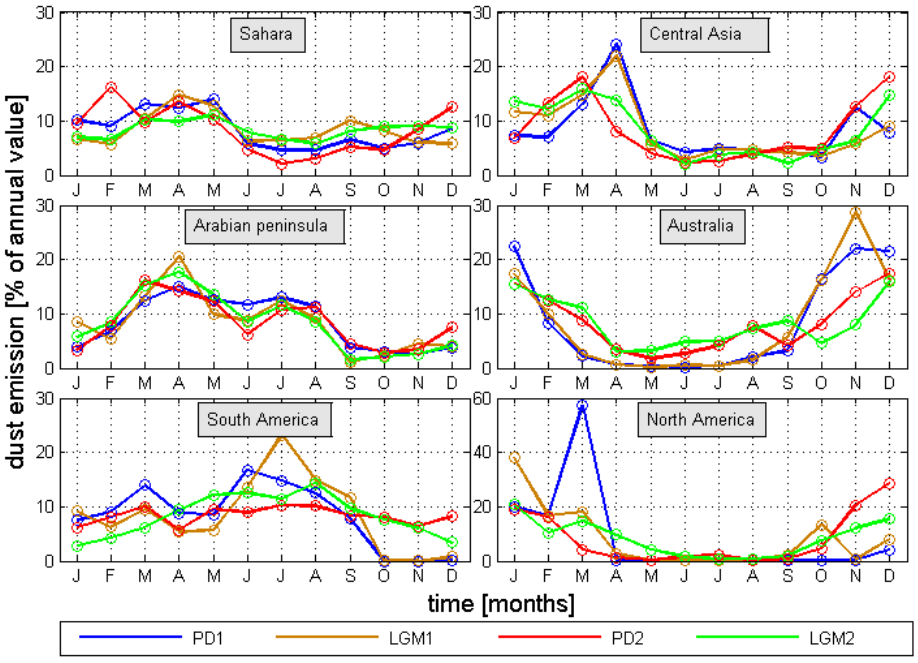

Figure 44: Monthly dust emission for the present-day and last glacial maximum simulations. Given are the values for the specified source regions Sahara, central Asia, Arabian peninsula, Australia, South America and North America. The monthly emission is given in percentage of the total annual dust emission value.

Acknowledgements

I would like to express my gratitude to the people, who have helped and supported me throughout my master thesis.

First of all, I would like to thank my supervisors Professor Gerrit Lohmann and Doctor Martin Werner for the chance to write my master thesis in their working group of Paleoclimate Dynamics at the Alfred Wegener Institut Bremerhaven. I am especially grateful to Martin Werner, for the immense effort and the fact that his door was always open to me, when I needed help.

I would also like to thank Tim Carlsen and Frank Lamy for their fruitfull correspondance and especially Tim Carlsen for his remote assistance, getting started with the ECHAM5-HAM2 model. I want to thank Wolfgang Cohrs, who supported me in technical terms and with the backup of my data. Additionally, I very much appreciated the help from my colleagues with whom I had the opportunity to share the office and I especially want to thank Christian Stepanek, Michael Stärz and Paul Gierz. Their support saved me a lot of time and trouble and we spent many nice lunch breaks with interesting discussions together.

But above all, I am grateful to my family and my boyfriend Dennis, for their unconditional support and love.